HEAT TRANSFER ENHANCEMENT IN A CHANNEL WITH POROUS BAFFLES

A Dissertation

by

KANG-HOON KO

Submitted to the Office of Graduate Studies of
Texas A&M University
in partial fulfillment of the requirements for the degree of

DOCTOR OF PHILOSOPHY

December 2004

Major Subject: Mechanical Engineering

HEAT TRANSFER ENHANCEMENT IN A CHANNEL WITH POROUS BAFFLES

A Dissertation

by

KANG-HOON KO

Submitted to Texas A&M University
in partial fulfillment of the requirements
for the degree of

DOCTOR OF PHILOSOPHY

Approved as to style and content by:

Nagamangala K. Anand (Chair of Committee)	Sai C. Lau (Member)
Ali Beskok (Member)	Hamn-Ching Chen (Member)
	Dennis O'Neal (Head of Department)

December 2004

Major Subject: Mechanical Engineering

ABSTRACT

Heat Transfer Enhancement in a Channel with Porous Baffles.

(December 2004)

Kang-Hoon Ko, B.S.; M.S., Inha Unversity Korea

Chair of Advisory Committee: Dr. N.K. Anand

An experimental and numerical investigation of heat transfer enhancement in a three dimensional channel using wall mounted porous baffles was conducted. The module average heat transfer coefficients were measured in a uniformly heated rectangular channel with staggered positioned porous baffles. A numerical procedure was implemented, in conjunction with a commercially available Navier-Stokes solver, to model the turbulent flow in porous media. The Brinkman-Forchheimer-Extended Darcy model was used for modeling fluid flow through the porous baffles. Conventional, one-equation, and two-equation models were used for heat transfer modeling. The accuracy and characteristics of each model were investigated and discussed. The results were compared with experimental data.

Baffles were mounted alternatively on the top and bottom walls. Heat transfer coefficients and pressure loss for periodically fully developed flow and heat transfer were obtained for different pore densities (10, 20, and 40 pores per inch (PPI)) with two different baffle heights (B_h / D_h = 1/3 and 2/3), and two baffle thicknesses (B_t / D_h = 1/3 and 1/12). The Reynolds number (Re) was varied from 20,000 to 50,000. To compare the effect of foam metal baffles, the data for conventional solid-type baffles was

obtained for (B_t / D_h =1/3). The maximum uncertainties associated with the module Nusselt number and friction factor were 5.8% and 4.3%, respectively. The experimental procedure was validated by comparing the data for the straight channel without baffles (B_h / D_h = 0) with those in the literature.

The use of porous baffles resulted in heat transfer enhancement as high as 300% compared to heat transfer in straight channels without baffles. However, the heat transfer enhancement per unit increase in pumping power was less than one for the range of parameters studied in this work. Correlation equations were developed for the heat transfer enhancement ratio and the heat transfer enhancement per unit increase in pumping power in terms of Reynolds number.

The conventional theoretical model, the dispersion conductivity model, and the modified two-phase model using the local thermal non-equilibrium theory were considered. The results from each model were compared against the experimental data, and compared to each other to investigate the efficiency of each model. Also, the characteristics of each model were discussed.

DEDICATION

To my parents, my brother, my wife, Hyekyung, and my son, John Y.

ACKNOWLEDGEMENTS

This dissertation would not have been possible without the encouragement and help from Dr. N.K. Anand. My deepest appreciation is given to him for his guidance throughout my graduate study. I would like to thank Dr. S. C. Lau for his advice and sharing his time for the experimental work. I also wish to thank Dr. A. Beskok and Dr. H.C. Chen for the advice as my committee members.

I am grateful to my parents for their love, encouragement, and prayers. I also thank my wife, Hyekyung for her support, and my son for his smiles.

I am also deeply thankful to Dr. N.K. Anand for his support for final proofing of this dissertation. I give my gratitude to my office mate, Bruno Miranda, for his assistance while conducting experiments. I give thanks to my friends, Ganesh Venkatesan, George H. Ayers, and Gabriel Barbosa for their suggestions and critique while I was writing this dissertation.

I also wish to thank the staff of the Department of Mechanical Engineering for their kindness and help provided during my studies at Texas A&M University.

TABLE OF CONTENTS

Page

ABSTRACT iii

DEDICATION v

ACKNOWLEDGEMENTS vi

TABLE OF CONTENTS vii

LIST OF TABLES xi

LIST OF FIGURES xii

NOMENCLATURE xvi

CHAPTER

I INTRODUCTION 1

1.1 Background 1
1.1.1 The Demand for Heat Transfer Enhancement 1
1.1.2 Heat Transfer Enhancement Using Serpentine Geometry 2
1.1.3 Heat Transfer Enhancement Using Porous Media as Baffles 3
1.2 Literature Review 3
1.2.1 The Experimental Data 3
1.2.2 Porous Baffles for Heat Transfer Enhancement 4
1.2.3 A Brief Review of Theoretical Development in Porous Media 6
1.3 Objectives 8
1.3.1 Experimental Investigation 8
1.3.2 Numerical Analysis 9
1.4 Outline of the Study 10

II HEAT TRANSFER IN POROUS MEDIA 11

2.1 Definition of Porous Media and Classification of Solid Matrices 11
2.2 Porosity 13
2.3 Permeability 14
2.4 Effective Thermal Conductivity 15
2.4.1 The Concept of Effective Thermal Conductivity 15
2.4.2 Thermal Conductivity in Conducting Fluid in a Porous Medium 15

CHAPTER Page

2.4.3 Thermal Diffusivity in Single Phase Forced Flow in a Porous Medium 18
2.4.4 Thermal Diffusivity in Two Phase Forced Flow in Porous Media 18
2.5 Equation of Motion in a Homogeneous Fluid 19
2.5.1 Darcy's Law 19
2.5.2 Forchheimer -Extended Darcy's Law 21
2.5.3 Brinkman-Forchheimer-Extended Darcy's law 21
2.6 Volume Averaging Method 22
2.7 Volume Averaged Continuity Equation 25
2.8 Volume Averaged Momentum Equations 26
2.9 Volume Averaged Energy Equation 29
2.9.1 One-Equation Model and Local Thermal Equilibrium 31
2.9.2 Two-Equation Model and Local Thermal Non-Equilibrium 34

III EXPERIMENTAL SETUP AND PROCEDURE 37

3.1 Introduction 37
3.2 The Uniqueness of the Experimental Investigation 37
3.3 Experimental Setup 40
3.4 Instruments and Calibration 45
3.5 Data Reduction 47
3.5.1 Data Reduction of Mass Flow 47
3.5.2 Data Reduction of Friction Factor 49
3.5.3 Heat Loss Compensation 49
3.5.4 Data Reduction of Heat Transfer 54
3.6 Uncertainty Analysis 54
3.7 Independent Parameters 57

IV EXPERIMENTAL RESULTS AND DISCUSSION 59

4.1 Validation of Test Rig 59
4.2 Heat Transfer Enhancement Ratio 60
4.3 Heat Transfer Performance Ratio 68
4.4 Summary of Experimental Results 71

V NUMERICAL INVESTIGATION 73

5.1 Introduction 73
5.2 Definition of Problem 73
5.2.1 Periodicity 73
5.2.2 Geometry 74
5.3 The Solver; FLUENT 74

CHAPTER Page

5.3.1 Benefits and Limitations of Using a Commercial Code 74
5.3.2 Momentum Equation 76
5.3.3 Turbulence Model 76
5.3.4 Energy Equation 78
5.4 Programming Using User Defined Functions (UDFs) 78
5.4.1 User Defined Functions 78
5.4.2 Flowchart for Two-Phase Solution 79
5.5 Convergence Criteria and Numerical Scheme 81
5.6 Mesh Generation 82
5.6.1 Dimensionless Distance 82
5.6.2 Sample Grids 83
5.7 Models and Implementation 85
5.7.1 Heat Transfer (Conventional Model) 85
5.7.2 Heat Transfer (One-Equation Model) 85
5.7.3 Heat Transfer (Two-Equation Model) 90
5.8 Boundary Conditions 93
5.8.1 Boundary Conditions for the One-Equation Model 93
5.8.2 Boundary Conditions for the Two-Equation Model 93
5.9 Nusselt Number Evaluation 98
5.9.1 Nusselt Number Evaluation for the One-Equation Model 98
5.9.2 Nusselt Number Evaluation for the Two-Equation Model 100

VI RESULTS AND DISCUSSION 102

6.1 Grid Independence Test 102
6.2 Results of the Conventional Model 104
6.2.1 Forchheimer Constant Dependency 104
6.2.2 Comparison of Heat Transfer Enhancement 108
6.2.3 Comparison of Heat Transfer Enhancement and Dimensionless Friction Factor for Selected Inertial Coefficients 112
6.2.4 Turbulent Conductivity 112
6.2.5 Velocity Distribution 116
6.2.6 Temperature Distribution 120
6.2.7 Turbulent Kinetic Energy and Turbulent Dissipation Rate 120
6.3 Results of One-Equation Model 124
6.3.1 Dependency of Heuristic Coefficients 124
6.3.2 Comparison of Heat Transfer Enhancement 126
6.4 Results of Two-Equation Model 129
6.4.1 Comparison of All Models 129
6.4.2 Temperature Difference between the Two Phases 133
6.4.3 Interfacial Heat Transfer Coefficient (h_{sf}) 136
6.4.4 Pressure Distribution 139

CHAPTER Page

6.4.5 Isotherm for Sample Case (D_t =10) 139
6.4.6 Local Heat Transfer Distribution 141

VII CONCLUSIONS.....143

REFERENCES.....145

APPENDIX A 150

APPENDIX B 155

VITA 165

LIST OF TABLES

TABLE Page

3.1 Material properties [12].....40

3.2 Coefficients for the heat loss compensation for each module.....53

3.3 Test parameters 58

4.1 Correlation coefficients for Nusselt numbers.....70

5.1 Convergence criteria and numerical scheme.....81

5.2 Effective diameter of aluminum foam 88

5.3 Comparison of specific area (m^2).....91

6.1 Maximum percent relative error for Nu^+ 102

LIST OF FIGURES

FIGURE Page

2.1 Classifications of matrix structure [16]. 12

2.2 Microscopic view of a porous medium 24

2.3 Imaginary micro-structure 30

3.1 Samples of the porous material 39

3.2 Schematic diagram of the experimental set-up 42

3.3 Schematic of the test section 43

3.4 Copper plate dimensions 44

3.5 Attached copper plates 45

3.6 Photographs of the experimental setup 46

3.7 Temperature distribution for heat loss test (Re=0) 50

3.8 Determination of heat loss for a plate using the linear assumption 52

4.1 The validation of heat transfer experiments (comparison of the Nusselt number) 59

4.2 Average module Nusselt number for 20 PPI, B_h / D_h = 1/3 61

4.3 Heat transfer enhancement ratio for B_h / D_h =1/3 62

4.4 Friction factor for B_h / D_h =1/3 64

4.5 Heat transfer enhancement ratio for B_h / D_h = 2/3 65

4.6 Friction factor for B_h / D_h = 2/3 67

4.7 Heat transfer performance for B_h / D_h = 1/3 68

FIGURE Page

4.8 Heat transfer performance for $B_h / D_h = 2/3$ 69

5.1 Computational domain....75

5.2 Flowchart for the two-equation model calculation 80

5.3 Generated mesh....84

5.4 The variation of $\sqrt{180(1-\varepsilon)^2/\varepsilon^3}$ with porosity 89

5.5 Boundary conditions for one-equation model 92

5.6 Heat transfer at the interface between the porous medium and the impermeable wall [58]....94

5.7 Boundary conditions for the two-equaion model 99

6.1 Grid independence test for $B_t / D_h = 1/12$ and $B_h / D_h = 1/3$ 103

6.2 Percent relative error for dimensionless friction factor for various inertial coefficients....106

6.3 Velocity vectors for a sample case 107

6.4 Percent relative error for dimensionless friction factor for various inertial coefficients (plotted against dimensionless friction factor)....109

6.5 Absolute error for the heat transfer enhancement ratio for the various inertial coefficients....111

6.6 Relative error for the heat transfer enhancement ratio for the various inertial coefficients....112

6.7 Absolute and relative error for the dimensionless friction factor with corrected inertial coefficients 114

FIGURE Page

6.8 Absolute and relative error for Nu^+ with corrected inertial coefficients 115

6.9 Turbulent conductivity at the central plane for a sample case (unit: W/m-K) 116

6.10 X-directional velocity distribution at the central plane for a sample case (unit: m/s) 118

6.11 Y- directional velocity distribution at the central plane for a sample case (unit: m/s).....119

6.12 Z-directional velocity distribution at various locations for a sample case (unit: m/s).....120

6.13 Temperature distribution at the central plane for a sample case (unit: ℃).....122

6.14 Turbulent kinetic energy distribution at the central plane for a sample case (unit: J/Kg).....123

6.15 Turbulent dissipation rate distribution at the central plane for a sample case (unit: m^2/s^3).....124

6.16 Comparison of the Nusselt number variations against D_t for the one-equation model. 126

6.17 Comparison of percent relative error for heat transfer enhancement ratio for the one-equation model (conventional and $D_t = 10$) 128

6.18 Comparison of percent relative error for heat transfer enhancement ratio for the one-equation model ($w = 1.5$ and $w = 0.5$).....129

6.19 Comparison of the Nusselt number variations with D_t for the two-equation model.....131

FIGURE Page

6.20 Temperature difference between two phases for a sample case (D_t=0.375~10) ..133

6.21 Temperature difference between two phases for a sample case (D_t=20~50) 135

6.22 Heat transfer coefficient variations for a sample case (D_t=0.375~10) 136

6.23 Heat transfer coefficient variations for a sample case (D_t=20~50) 138

6.24 Isobar distribution for a sample case 139

6.25 Isotherm distribution for a sample case 141

6.26 Local heat transfer coefficients for a sample case 143

NOMENCLATURE

A	flow cross-sectional area (m^2)
A_{int}	interface area or specific interface area ($A_{interface} / V$)
A_s	area of a plate (m^2)
B_h	baffle height (m)
B_p	baffle pitch (m)
B_t	baffle thickness (m)
C	inertial coefficient (Forchheimer coefficient)
C_p	specific heat at constant pressure ($kJ / kg \cdot K$)
$d\mathbf{A}$	unit normal vector directing toward solid phase
D_h	hydraulic diameter ($4A / P$)
d_p	pore diameter (m)
d_v	void diameter ($4\varepsilon / A_{int}$)
dV	control volume element
ε	porosity or turbulent dissipation rate (m^2 / s^3)
f	Darcy friction factor
f_n	numerical value of Darcy friction factor
f_s	Darcy friction factor for a straight channel
f^+	dimensionless friction factor (f / f_s)

f_n^+	numerical value of dimensionless friction factor (f_n / f_s)
H	channel height (m)
h	heat transfer coefficient ($W / m^2 °C$)
h_{sf}	interfacial heat transfer coefficient ($W / m^2 °C$)
k	turbulent kinetic energy (J / kg)
K	thermal conductivity, permeability, or Kelvin temperature
L	distance between pressure taps
$\dot{m}$	mass flow rate of air
$\overline{Nu}_p$	average plate Nusselt number
$\overline{Nu}_m$	average module Nusselt number
$\overline{Nu}_s$	Nusselt number for fully developed flow in a straight channel
$\overline{Nu^+}$	heat transfer enhancement ratio ($\overline{Nu_{m,pdf}}$ / $\overline{Nu_s}$)
$\overline{Nu^*}$	heat transfer performance ratio ($\overline{Nu^+}$ /($f_{m,pdf}$ / f_s)$^{1/3}$)
P	perimeter or pressure
Pe	Peclet number
PPI	pores per linear inch
Pr	Prandtl number
Q	amount of heat applied or flow rate
Q_{loss}	amount of heat lost to the ambience
Re	Reynolds number

Re_h	Reynolds number based on channel hydraulic diameter $\left(\rho U D_h / \mu\right)$
S	body force
T_{in}	module inlet temperature of air
$\overline{T}_b$	bulk temperature of air
$\overline{T}_w$	average mean wall temperature
U	average air velocity
u	x-directional velocity or mean velocity (m/s)
v	y-directional velocity (m/s)
V_f	volume of fluid
V_s	volume of solid
V_{total}	total volume
W	channel width
z	z-directional velocity (m/s)

Greek Symbols

β	ratio of the orifice plate diameter to the pipe diameter
ε	porosity (V_f / V_{total})
ρ	density
μ	dynamic viscosity
Δ	difference

$\langle\ \rangle$	volume averaged
$\langle\ \rangle^{f\ or\ s}$	intrinsic volume averaged for fluid or solid phase.

Subscripts

d	dispersion
eff	effective
f	fluid
i	baffle index, i^{th} node
m	module
p	plate
pdf	periodically fully developed flow
s	solid
w	wall

Superscripts

f	fluid
s	solid
'	derivative of variable or variation of a term
*	effective

Fonts

Bold	vector

CHAPTER I

INTRODUCTION

1.1 Background

This dissertation presents the results of the experimental and numerical approach to enhance heat transfer using porous media in a three-dimensional channel.

1.1.1 The Demand for Heat Transfer Enhancement

Porous media has been of interest for a while due to its wide range of applications in electronic cooling, heat exchangers, nuclear power generation, and geothermal systems. For example, due to the increased execution speed and denser circuitry, modern desktop central processing units (CPU) generate higher levels of heat fluxes and will continue to increase in the near future. The general cooling requirement for the CPU in a desktop PC ranges from $10 W/cm^2$ to $25 W/cm^2$. For safe operation, CPUs are known to be maintained below 140°C, but heat removal by natural convection and the forced convection of air are limited to $0.001 W/cm^2 C°$ and $0.01 W/cm^2 C°$, respectively. Forced convection of a liquid can remove heat flux as much as $0.1 W/cm^2 C°$. However, higher heat removal capacity will be required for future computers and for parts of electronic equipment.

Dissertation style and format follow that of the *International Journal of Heat and Mass Transfer*.

It is well known that heat transfer rates will increase with an increase in surface area, and it is also proportional to heat transfer coefficients. The surface can be grooved at an optimal depth and angle or blocked with ribs to change the flow pattern to increase the heat transfer rate at the surface.

By using a porous medium as baffles in a channel (or simplified form of a heat exchanger), it is expected to outperform not only smooth channels, but also channels with solid baffles with less pumping power required.

1.1.2 Heat Transfer Enhancement Using Serpentine Geometry

The use of serpentine type or baffled type channels is one of the commonly used passive heat transfer enhancement strategies in single-phase internal flows. Accordingly, the study of fluid flow and heat transfer in serpentine channels has received considerable attention [1, 2]. This passive heat transfer enhancement strategy has been used for various types of industrial applications such as shell-and-tube type heat exchangers, electronic cooling devices, thermal regenerators, internal cooling systems of gas turbine blades, and labyrinth seals for turbo-machines.

Periodically positioned baffles in baffled channels and periodic turns in serpentine channels periodically interrupt hydrodynamic and thermal boundary layers. Downstream of each baffle (or turns in serpentine channels) the flow separates, re-circulates, and impinges on the wall. Flow impingement and fin effect are the main reasons for heat transfer enhancement in such channels. Due to periodicity in the geometry, the flow and heat transfer will never reach a fully developed state. However,

in modules far from the channel entrance flow, and heat transfer will be periodically fully developed [3, 4].

1.1.3 Heat Transfer Enhancement Using Porous Media as Baffles

Due to the aforementioned practical applications, researchers have been interested in modeling non-Darcian transport through porous media. While the use of solid baffles results in significant heat transfer enhancement the associated increase in pressure drop and higher local thermal stress, due to the recirculation zone near the root of the baffle, is of concern, thus warranting the exploration of the use of porous baffles to enhance heat transfer while keeping the pressure drop to a minimum.

The advantages of using porous baffles are: (1) higher surface area to volume ratio, which will increase the dispersion of the heat drastically; (2) due to their structural stiffness and light weight, they can be used for thermal management in aerospace applications, and (3) their nature of forcing uniform distribution of flow will homogenize the thermal dispersion of the surface, which will reduce local thermal stress.

1.2 Literature Review

1.2.1 The Experimental Data

Experimental data on forced convective heat transfer in channels with partially filled porous material is limited [5, 6]. Accordingly, it is difficult to verify numerical simulation. In search of relevant sources for review only one numerical study [5] showed the comparisons with the experimental data in a turbulent flow regime. It will be

challenging to numerically simulate the flow with partially filled fibrous material and to compare simulation results with the experimental data.

1.2.2 Porous Baffles for Heat Transfer Enhancement

The exploration of heat transfer enhancement started with the experiments of Koh and Stevens [7] and Mergerlin et al. [8]. Koh and Stevens demonstrated the enhancement of cooling effectiveness by using porous materials in a coolant passage subject to constant heat flux. Wall temperature in the circular passage dramatically dropped and the temperature of the coolant increased, by a factor of two.

Kuo and Tien [9] presented numerical results for a fully packed bed with a foam material to enhance liquid forced convection cooling at low Reynolds number ranges (Re = 2000-6000) with discrete heat sources. They found that the heat transfer increased between 2-4 times, the enhancement was due to the dispersion of heat in the solid matrix, and the heat transfer enhancement was pronounced at high flow rates and large permeability.

Rachedi and Chikh [10] numerically studied forced convection cooling in the presence of porous inserts in electronic devices. Results showed that the temperature dropped by a factor of two.

Hwang and Chao [11] showed that a decreased pore density can decrease the entrance length and increase the local Nusselt number in their packed bed experiments using sintered material. They introduced a two-equation model for an energy equation to incorporate the large difference in conductivities between the solid and fluid phase. Hwang and Chao overcame the heat transfer over prediction of the conventional one

equation model and showed the existence of non-equilibrium thermal conditions between the fluid and the solid matrix.

Recently, Kim et al. [12] experimentally investigated an asymmetrically heated packed bed filled with foam material. They developed correlation equations for Nusselt numbers for different foam materials as a function of the Darcy number.

Hwang and Liou [13] found that the thermal performance in the rectangular channel with ribs was best when the ratio between the vacant area and solid area (open area ratio) in the ribs was 44%. Using the same configuration as that of Hwang and Liou [13], Liou and Chen [14] experimentally studied turbulent heat transfer and fluid flow in a rectangular channel with perforated ribs. Consideration was given to both attached (to wall) and detached ribs. Perforated ribs were made of aluminum. Their study indicated the highest Nusselt number to be around three (3) times higher than that for a corresponding channel without ribs.

Hwang [5] conducted experiments to study turbulent heat transfer and fluid flow in a channel with porous baffles. The porous baffles were mounted on the top and bottom walls in a staggered manner. In addition, experiments were also conducted with solid baffles for the sake of comparison. Consideration was given to two different baffle heights and the Reynolds number was varied from 10,000 to 50,000. In this study thermocouples were mounted along the center-line of the bottom wall to measure the local heat transfer. Accordingly, heat transfer data was reported only along the center-line of the channel. In addition, Hwang [5] measured the turbulent intensity and velocity

profile using hot wire anemometry. His study showed that channels with porous baffles have a significantly lower friction factor.

1.2.3 A Brief Review of Theoretical Development in Porous Media

Extensive reviews can be found in several books [15-18]. Darcy showed in his experiment that the mass flow is proportional to the pressure drop and inversely proportional to the length of the test section. Hydraulic conductivity, known as permeability, was the unknown coefficient.

Effort has been put into many studies to obtain the methods of evaluation of permeability and values of permeability. Since Darcy's model is not valid when the flow velocity is relatively high, Forchheimer suggested that the square of the velocity may better reflect the inertial type of drag force. He introduced the Forchheimer-Extended Darcy model by adding the inertial drag. When the flow has constraints such as a wall, there is a sudden jump of flow velocity due to the wall effects. Brinkman incorporated this effect by adding the Brinkman term.

While Wooding [19] was the first who applied the Darcy model to convective terms, Vafai and Tien [20] suggested macroscopic governing equations derived from Navier-Stokes' equations using Slattery's [21, 22] volume average method and the Brinkman-Forchheimer-Extended Darcy model. Vafai and Tien, at this time, used the pore velocity as the variable of the Brinkman-Forchheimer-Extended Darcy term. Later, Hunt and Tien [23] suggested another type of governing equation using the Darcian velocity, which was the basis for most of the research papers.

Nakayama [17] suggested that pore-pressure should be used for the momentum equation since the pressure can be gauged only inside the pore region. Many studies quoted the governing equation for the flow in porous media, which was developed by Vafai and Tien [20] for their numerical simulations, but these studies often used slightly modified types of governing equations.

Permeability is important for the given porous medium in momentum transport. It is one of the factors to be known for numerical simulation of momentum transport in porous media. Due to the random characteristics and irregularity of the geometric connectivity of the porous medium it is often required to be measured, but there is a series of attempts to determine permeability in a specific condition, theoretically by using easily obtainable properties such as porosity or volume fraction. However, those methods are limited to a simple mathematically determinable form of geometric configuration.

Various studies have been carried out to understand the energy transport in a porous medium. It has been found that the thermal dispersion caused by a solid matrix plays an important role in the heat transfer enhancement. It is known that a second order thermal dispersion tensor is asymmetric when the medium is uniform. A series of investigations have been conducted for thermal dispersion effects in porous medium [20, 24-27]. Later it was found that the transverse thermal dispersion is much more important than the longitudinal thermal dispersion [28].

The local thermal equilibrium (LTE) condition is one of the important factors to be considered. If the flow is sluggish and the thermal conductivity of the solid matrix is

relatively low, then we can assume that there is no abrupt temperature change at the interface. Under this condition, the solid phase and fluid phase temperature at the interface are the same. Two separate energy equations for each phase can be combined into one while the heat transfer through convection due to the different interfacial temperature change can be neglected.

Dixon and Criswell [29] investigated local thermal non-equilibrium (LTNE) between the two phases and were the first to obtain a fluid to solid heat transfer correlation. Achenbach [30] noted that due to the complexity of the solution procedures for LTNE problems, negligence of the heat transfer between phases may be required. But researchers [26, 29, 30] have presented their own correlations and employed [11, 31] two separate energy equations to explain the heat transfer between two phases.

However, all of the referenced research is based on a saturated packed bed type configuration, and the two-equation model approach entails the wall boundary problem to be handled.

1.3 Objectives

1.3.1 Experimental Investigation

The objective of the present work is to conduct experiments to measure module averaged Nusselt numbers and the friction factor for flow in a 3-D channel with staggered porous baffles. Due to the limited resources, variation of parameters such as height and thickness of the baffles and pore density have to be limited to a manageable

scope. Through this limited investigation, the effect of each parameter was investigated and the relative correlations were obtained.

1.3.2 Numerical Analysis

As mentioned in an earlier section, due to the experimental limitation, a wider range of investigations with different parameters was not feasible. But numerical simulations can be used for further investigation with the help of the correlations and data obtained from the experiments.

Numerical experiments can give more freedom on selection of the conditions and are less costly while the experiments are generally more time consuming and can be costly. But it has to be noted that before any credit is given to the computational simulations, the methods have to be evaluated against experimental data. Therefore, the first objective is to evaluate the code against the results from the experiments. Along with the methods of evaluation and results, the validity of the codes and the problem of current evaluation methods will be discussed further.

Thus, the first objective of numerical analysis is to understand the currently available models and to utilize and modify the appropriate model which can be used to simulate the experimental cases for the comparison against the experimental data sets.

The second objective of numerical analysis is to investigate and analyze the local flow field and heat transfer information to gain more profound physical understandings.

1.4 Outline of the Study

The dynamics and heat transfer of the flow in porous media are discussed in Chapter II. Important properties such as porosity and permeability are explained with the widely used correlations. The procedures for obtaining macroscopic governing equations for the flow in porous media are also shown in Chapter II.

The experimental setup and procedures are given in Chapter III. Data reduction methods and uncertainty analysis are also shown in this chapter. Experimental results are discussed in Chapter IV. Validations are given with the comparison of the known correlations. In addition, the heat transfer enhancement and performance with equal pumping power conditions are discussed in this chapter.

The modeling procedures for the numerical investigation are explained in Chapter V. The grid generation method, convergence criteria, boundary conditions, and the other numerical procedures are given in Chapter V.

In Chapter VI, comparisons of the experimental and numerical results are shown and discussed. The comparison of three types of models are shown and discussed along with the results. The method of determination of inertial coefficients using numerical experiments is shown.

In Chapter VII, the summary of the current study is given and further study is suggested.

CHAPTER II

HEAT TRANSFER IN POROUS MEDIA

2.1 Definition of Porous Media and Classification of Solid Matrices

Porous medium can be defined as a material consisting of a solid matrix with an interconnected void. Kaviany [16] classified the matrix structures of porous media based on the structural characteristics of porous media (Fig. 2.1). Porous media where the grains are not connected to each other are considered unconsolidated. If the grains are cemented together, such solid matrices are called consolidated porous media (Fig. 2.1).

Many of the scientific and engineering fields actively involved the development of theory and the understanding of the dynamics and heat transfer through porous medium include groundwater, nuclear power generation, oil reservoir, volcanic lava movement, storage of grains, and the transport of air through coal sediments.

However, current understanding of the fluid dynamics and heat transfer through this media is quite limited. Extensive studies have been conducted with rather simplified cases such as matrices consisting of capillary tubes and spheres with sluggish flow or stagnant fluid.

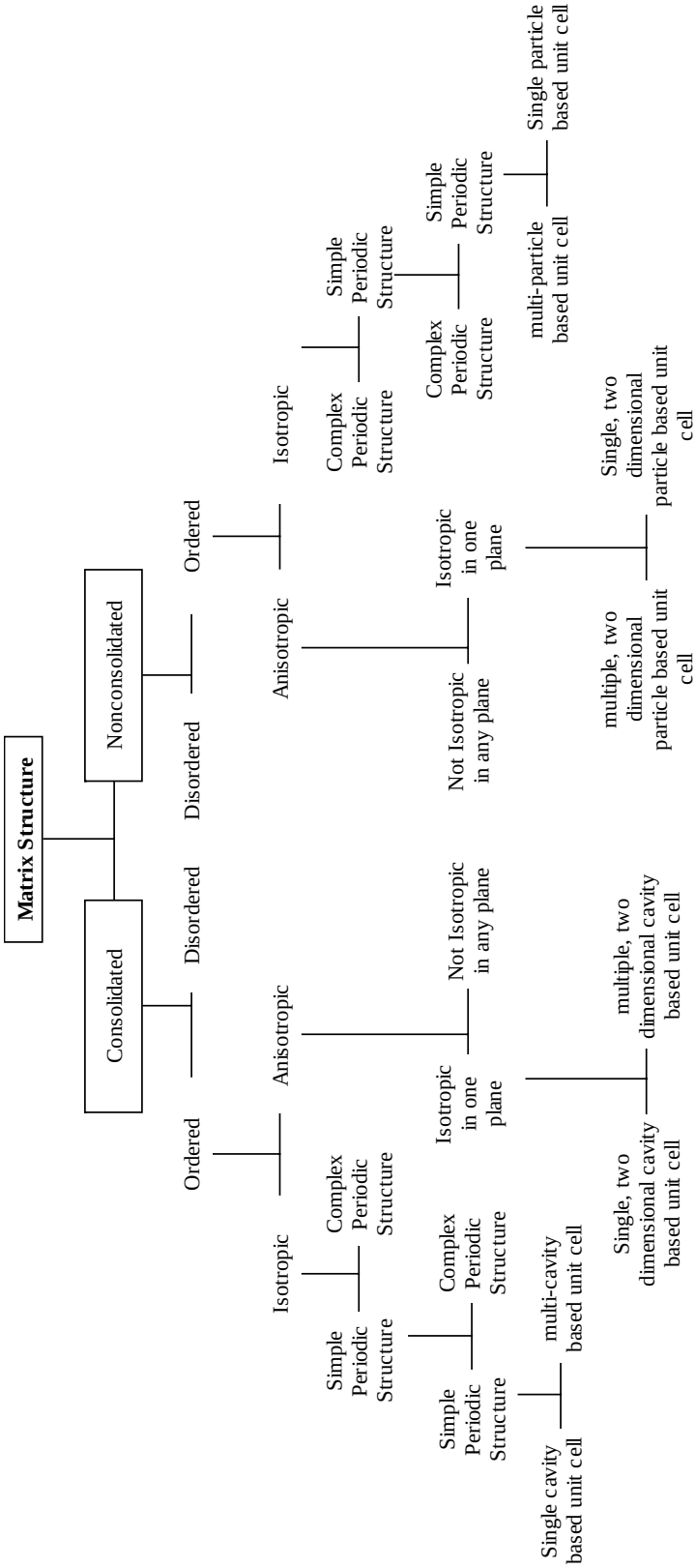

Fig. 2.1. Classifications of matrix structure [16].

2.2 Porosity

Porosity (ε), or volumetric porosity, a macroscopic porous medium property, is defined as the ratio of volume of the void space, or volume which is taken by fluid (V_f), to the total volume (V_{total}) of the medium.

$$\varepsilon = \frac{V_f}{V_{total}} \tag{2.1}$$

Occasionally, volume fraction (ϕ) of porous medium is used instead of porosity for description of the porous medium. With the volume taken by solid matrix (V_s), equation (2.2) can be defined.

$$\phi = \frac{V_{total} - V_f}{V_{total}} = \frac{V_s}{V_{total}} \tag{2.2}$$

Porous medium can have pores or voids, which are not inter-connected. Pores can be inter-connected only to each other (dead-end) or may not be inter-connected at all (isolated). In these situations, porosity can be referred as “absolute porosity.” However, in an engineering sense, the inter-connected pores are much more interesting. Hence, the concept of “effective porosity” arises. The definition of the effective porosity is the volume fraction of inter-connected pores ($\left(V_f\right)_{eff}$) to the total volume.

$$\varepsilon_{eff} = \frac{\left(V_f\right)_{eff}}{V_{total}} \tag{2.3}$$

If the particles are loosely packed, the effective porosity and the porosity can be considered almost equal. For natural media the porosity does not exceed 0.6. For packed bed of spheres, it ranges from 0.245 to 0.476. Other details about the measurement of porosity and porosity values can be found in literature [15].

2.3 Permeability

Permeability is a measurable property of hydraulic conductance to the flow through the solid matrix. Various attempts have been made to correlate permeability to easily measurable structural variables such as porosity, pore diameter, etc.

Among the many models such as capillary tube models, fissure models, hydraulic radius models, and so forth, the hydraulic radius model is used widely for a packed bed of spheres. Semi-heuristic Carman-Kozeny equation for permeability is given by,

$$K = \frac{1}{180}\frac{\varepsilon^3}{(1-\varepsilon)^2} d_p{}^2 \qquad (2.4)$$

where, d_p is the effective particle diameter and the constant 1/180 is used to fit the experimental data.

2.4 Effective Thermal Conductivity

2.4.1 The Concept of Effective Thermal Conductivity

For quite sometime determination of the correct effective thermal conductivity has been a challenge. There have been some attempts to determine the correct thermal conductivity and to correlate with readily obtainable properties such as porosity, permeability, void diameter, and particle diameter.

However, the term “effective” sometimes leads to confusion since the term “effective” can be between laminar and turbulent, between one phase and another phase, or combination of all these effects. Also it should be noted that the term “effective conductivity” doesn’t imply a material property unlike conductivity of a natural medium. Without clear understanding of a given problem and its conditions, effective conductivity cannot be used directly to the other problems.

Thus, in a strict concept, the effective conductivity is not a property to represent conduction mode only between two media. Actually the correct term would be “diffusivity.” In this section, the currently available theory will be briefly discussed.

2.4.2 Thermal Conductivity in Conducting Fluid in a Porous Medium

Instead of using a volume averaged approach and the use of modifiers such as dispersion conductivity, there is another approach to express effective conductivity based on the theory of particle concentration. The particle concentration method has its theoretical limitation due to the explanation of the contact mechanism. Analysis was

started using particles in a fluid, or a dilute suspension case. Namely, porosity is almost 1 or volume fraction of solid is nearly zero.

Maxwell's [32] model is the first attempt to describe effective thermal conductivity by this approach.

$$\frac{K_{eff}}{K_1} = \frac{1+2\beta\phi}{1-\beta\phi}, \quad \beta = \frac{\alpha-1}{\alpha+2}, \quad \alpha = \frac{K_2}{K_1} \tag{2.5}$$

where K_1 and K_2 denote the thermal conductivity of dilute material 1 and 2, respectively. Equation (2.5) gives an upper bound and predicts well with rather dilute solution of granular flow ($\phi < 0.1$), but it did not correlate well in dense material.

Many attempts have been made after Maxwell using a geometric arrangement analysis of particles [16]. Among the attempts, one of the best correlations was made by Hadley [33]. He used the weighted average method using Maxwell upper bound (α_0) and the introduction of an adjustable function (f_0).

$$\begin{aligned}\frac{K_{eff}}{K_1} &= (1-\alpha_0)\frac{\varepsilon f_0 + K_2/K_1(1-\varepsilon f_0)}{1-\varepsilon(1-f_0)+K_2/K_1\varepsilon(1-f_0)} \\ &\quad + \alpha_0 \frac{2(K_2/K_1)^2(1-\varepsilon)+(1+2\varepsilon)K_2/K_1}{(2+\varepsilon)K_2/K_1+(1-\varepsilon)}\end{aligned} \tag{2.6}$$

Where, $f_0 = 0.8 + 0.1\varepsilon$, $\alpha_0 = \alpha_0(\varepsilon)$

$$log(\alpha_0) = -4.898\varepsilon, \ 0 \le \varepsilon \le 0.0827$$
$$log(\alpha_0) = -0.405 - 3.154(\varepsilon - 0.0827), \ 0.0827 \le \varepsilon \le 0.298$$
$$log(\alpha_0) = -2.084 - 6.778(\varepsilon - 0.298), \ 0.298 \le \varepsilon \le 0.580$$

Based on the result of Chiew and Glandt [34],

$$\frac{K_{eff}}{K_1} = \frac{1 + 2\beta\phi + (K_2 - 3\beta^2)\phi^2}{1 - \beta\phi} \qquad (2.7)$$

Gonzo [35] developed simpler and useful correlation.

$$\frac{K_{eff}}{K_1} = \alpha \frac{1 + 2(1-\alpha)/(1+2\alpha)(1-\phi)}{1-(1-\alpha)/(1+2\alpha)(1-\phi)}, \quad \alpha = \frac{K_2}{K_1} \qquad (2.8)$$

For both the range of $0.15 \le \phi \le 0.85$ and $\phi \ge 0.9$, it is well representing of the actual effective thermal conductivity. He also presented a range of data for various material types.

Boomsma and Poulikakos [36] developed a geometrical effective thermal conductivity model of a saturated porous metal foam based on the idealized three-dimensional basic cell geometry. He developed porosity as a function of geometric parameters and estimated an appropriate geometric radius for the proper prediction of both air and water effective thermal conductivities. Comparison with the experimental data showed good agreement with the model predictions.

In his experiment, Kim [12] showed effective thermal conductivity of foam metal, and the value is in the Table 3.1. Since the actual data was available, the data was used for both the one and two equation models.

2.4.3 Thermal Diffusivity in Single Phase Forced Flow in a Porous Medium

According to Kaviany [16], extensive research has been done for $K_s = 0$ cases. The database for the correlation for the thermal dispersion tensor is limited to more complex configurations such as higher thermal conductivity ratios ($K_s / K_f >> 1$), high Reynolds number flows including turbulent regime ($Re >> 10^4$), or the effects of surrounding enclosures which would be mandatory to solve the practical engineering problems. Some limited cases of experimental correlations were presented by Kaviany [16].

Among others, Koch and Bradley [37], Angirasa [38], and W.S. Fu [39]'s work are good references for the development and utilization of dispersion conductivity in forced convection related researches. The compilation of experimental work and theoretical development should also be a good topic for further research.

2.4.4 Thermal Diffusivity in Two Phase Forced Flow in Porous Media

The understanding for effective thermal dispersion and conductivity is quite incomplete for this case. Although no rigorous correlation is available for effective thermal conductivity in this case, there were a few attempts to obtain the correlation by Hashimoto et al. [40]; Crine [41]; and Saez et al. [42].

2.5 Equation of Motion in a Homogeneous Fluid

2.5.1 Darcy's Law

It would be interesting to look over developmental history for the fluid dynamics of porous media starting from Darcy's experiments before the general governing equations are presented using the concept of volume averaging methods [21, 22].

In 1856, Henry Darcy studied the flow of water through homogeneous sand in vertical canister. The macroscopic flow is one dimensional, slow, and driven by a gravity. The loosely packed sand filter can be considered as uniform, rigid, and an isotropic solid matrix.

He found that the rate of flow (Q) is (a) proportional to the constant cross-sectional area A , (b) proportional to piezometric head (Δh), and (c) inversely proportional to the length of sand filter (L). By combining the conclusions, Darcy formulated these conclusions as,

$$Q = \mathrm{K}A\frac{\Delta h}{L} = -\frac{\mathrm{K}A}{\rho g}\frac{\Delta P}{L} \qquad (2.9)$$

Darcy's flux defined as,

$$q = Q / A \qquad (2.10)$$

If a non-water fluid is used, the hydraulic conductivity (K) is replaced by the permeability (K),

$$\mathrm{K} = K\rho g / \mu \qquad (2.11)$$

Equation (2.9) can then be changed in to the form of equation (2.12)

$$q = -\frac{K}{\mu}\frac{\Delta p}{L} \qquad (2.12)$$

Equation (2.12) can be rewritten in a differential form,

$$q = -\frac{K}{\mu}\frac{dp}{dx} \qquad (2.13)$$

Where, x is the direction of the flow. Note that q is unit of velocity but it is not the velocity at the pore. It has the same meaning as superficial velocity, which can be used conveniently in the macroscopic momentum equation. The actual velocity at the pore (u_p), often called seepage velocity, can be defined using porosity of the porous medium,

$$u_p = Q / A\varepsilon \qquad (2.14)$$

The unit for permeability is Darcy. One unit of Darcy is equivalent to $9.87\times10^{-13} m^2$. Darcy's model has been examined extensively, and it is known that it is not applicable for liquid flows at high velocities and for gaseous flows at very low and very high velocities.

Typical values of permeability are: brick 10^{-15} to 10^{-13} m^2, sand 10^{-11} to 10^{-10}, and cigarette 10^{-9} m^2.

2.5.2 Forchheimer -Extended Darcy's Law

Darcy's law is solely based on a balance of the viscous force and pressure gradient. Thus, it is not applicable for flows at a high velocity, in which the inertia effect of the flow is no longer negligible. Forchheimer modified Darcy's law to account for the inertial contribution because of separation and wake around the porous micro-structure as,

$$-\frac{dp}{dx} = \frac{\mu}{K}u + \frac{C\rho_f}{K^{1/2}}u^2 \qquad (2.15)$$

The first term, or Darcy term, accounts for the viscous contribution, which is usually called "frictional drag." While the second term, or Forchheimer term, accounts for the inertial contribution, which is called "form drag." The inertial parameter can be estimated using porosity [43] as,

$$C = \frac{1.75}{\sqrt{150}\varepsilon^{1.5}} \qquad (2.16)$$

2.5.3 Brinkman-Forchheimer-Extended Darcy's law

In the case of highly porous media such as fibrous media and foam materials, the boundary frictional effect becomes important. Fluid particles can jump from the boundary to the bulk of the main flow, jumping over the microstructure. Brinkman modified Darcy's law as,

$$-\frac{dp}{dx} = \frac{\mu}{K}u - \mu_B \frac{d^2u}{dy^2} \qquad (2.17)$$

where Brinkman coefficient μ_B is usually considered as μ for the first approximation.

To account for all of the effects, equation (2.15) and equation (2.17) can be combined into one equation as,

$$-\frac{dp}{dx} = \frac{\mu}{K}u - \mu_B \frac{d^2u}{dy^2} + \frac{C\rho_f}{K^{1/2}}u^2 \qquad (2.18)$$

2.6 Volume Averaging Method

Due to the complexity associated with the geometric structure of a porous medium and the flow pattern such as turbulent eddies, microscopic investigations are limited at this time. Direct simulation of a simple geometry would be feasible, but it is not practical in the engineering application. Thus, instead of using the microscopic description of the phenomenon, it is common practice to use macroscopic governing equation to smooth out the local complexity of the actual phenomena, and focus on the conservation of the overall aspects of mass, momentum, and energy.

As explained in equation (2.10), the Darcian flux is not the actual velocity, and it is often referred to as apparent velocity, superficial velocity, or Darcian velocity.

To generalize this concept in three-dimensions, we can consider a control volume sufficiently larger than the length scale of flows within pores (Fig. 2.2). The characteristic length of a macroscopic control volume ($V_c^{1/3}$) has to be much larger than the microscopic characteristic length ($V^{1/3}$), but it has to be much smaller than

macroscopic characteristic length such as channel height, to obtain a meaningful governing equation through the averaging process. Under this assumption, the Darcian velocity can be defined as,

$$\langle \boldsymbol{u} \rangle = \frac{1}{V} \int_{V_f} \boldsymbol{u} dV \qquad (2.19)$$

where V_f is the volume space which the fluid occupies.

Considering the pore velocity, we can use an intrinsic averaging method,

$$\langle \boldsymbol{u} \rangle^f = \frac{1}{V_f} \int_{V_f} \boldsymbol{u} dV \qquad (2.20)$$

The relationship between two velocities is,

$$\langle \boldsymbol{u} \rangle^f = \langle \boldsymbol{u} \rangle / \varepsilon \qquad (2.21)$$

Using Slattery's [21, 22] volume averaging method, a few researchers [20, 44, 45] developed more rigorous approaches to obtain governing equations for mass, momentum, and energy conservation.

Assuming the porous media is isotropic, incompressible, and inflexible such that the properties are not depending on the direction and using a procedure analogous to Reynolds averaging procedure in turbulent flow, we can get the intrinsic average of an arbitrary product ab.

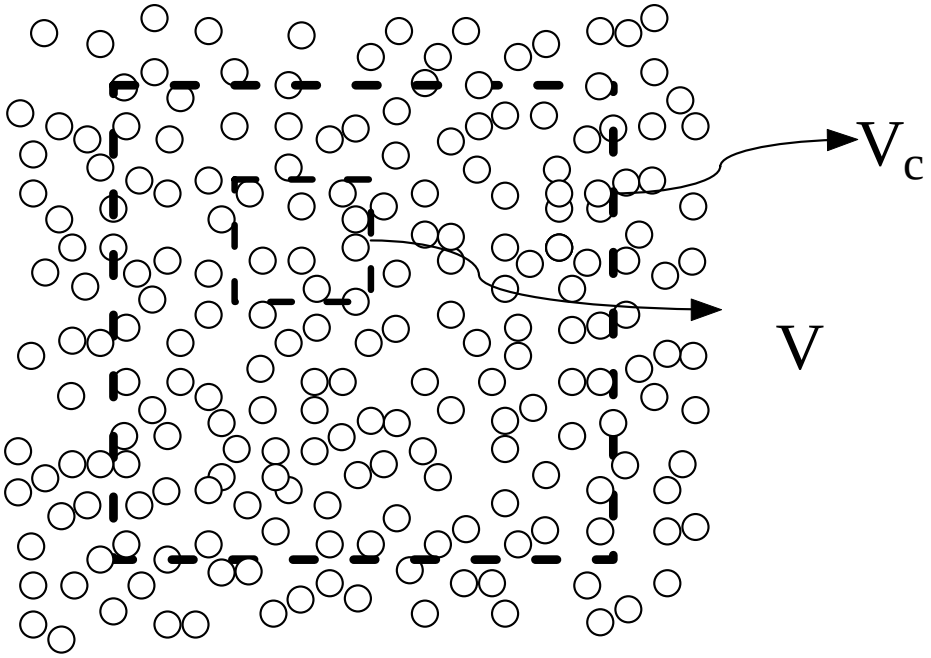

Fig. 2.2. Microscopic view of a porous medium.

$$\langle ab \rangle^f = \langle a \rangle^f \langle b \rangle^f + \langle a'b' \rangle^f \qquad (2.22)$$

where the prime denotes the deviation from the intrinsic average, such that,

$$a' \equiv a - \langle a \rangle^f \qquad (2.23)$$

Equation (2.22) can be rewritten using the proportional relationship of equation (2.21),

$$\langle ab \rangle = \frac{1}{\varepsilon} \langle a \rangle \langle b \rangle + \langle a'b' \rangle \tag{2.24}$$

It can also be derived using the following procedure,

$$\begin{aligned} &\langle ab \rangle^f = \langle ab \rangle / \varepsilon \\ &\langle a \rangle^f \langle b \rangle^f + \langle a'b' \rangle^f = \langle ab \rangle / \varepsilon \\ &\frac{\langle a \rangle}{\varepsilon} \frac{\langle b \rangle}{\varepsilon} + \frac{\langle a'b' \rangle}{\varepsilon} = \frac{\langle ab \rangle}{\varepsilon} \end{aligned} \tag{2.25}$$

It is also useful to denote the following relationship while deriving the governing equations. Using the analogy to the Leibnitz rule, the following equation is available.

$$\langle \nabla a \rangle = \nabla \langle a \rangle + \frac{1}{V} \int_{A_{int}} a dA \tag{2.26}$$

and

$$\left\langle \frac{\partial a}{\partial t} \right\rangle = \frac{\partial \langle a \rangle}{\partial t} \tag{2.27}$$

where A_{int} is the total interface between the fluid and solid, dA is its vector element pointing outward from the fluid side to solid side.

2.7 Volume Averaged Continuity Equation

The microscopic mass conservation equation is given by,

$$\nabla \cdot \boldsymbol{u} = 0 \tag{2.28}$$

By taking the volume average and using equation (2.26),

$$\nabla \cdot \langle \boldsymbol{u} \rangle + \frac{1}{V} \int_{A_{int}} \boldsymbol{u} \cdot d\boldsymbol{A} = 0 \qquad (2.29)$$

The second term vanishes, since the flow cannot penetrate solid medium. Thus, we have

$$\nabla \cdot \langle \boldsymbol{u} \rangle = 0 \qquad (2.30)$$

2.8 Volume Averaged Momentum Equations

The microscopic mass conservation equation is given by,

$$\frac{\partial \rho_f \boldsymbol{u}}{\partial t} + \nabla.(\rho_f \boldsymbol{u}\boldsymbol{u}) = -\nabla p + \nabla.\tilde{\boldsymbol{\tau}} + \rho_f \boldsymbol{g} \qquad (2.31)$$

where, ρ_f is density of fluid.

This can also be shown in the Cartesian-tensor form,

$$\frac{\partial \rho_f u_i}{\partial t} + \frac{\partial \rho_f u_i u_j}{\partial x_j} = -\frac{\partial p}{\partial x_i} + \frac{\partial \tau_{ij}}{\partial x_j} + \rho_f g_i \qquad (2.32)$$

where,

$$\tau_{ij} = \begin{bmatrix} \tau_{xx} & \tau_{xy} & \tau_{zx} \\ \tau_{xy} & \tau_{yy} & \tau_{yz} \\ \tau_{zx} & \tau_{yz} & \tau_{zz} \end{bmatrix} = \mu \left(\frac{\partial u_i}{\partial x_j} + \frac{\partial u_j}{\partial x_i} \right) + \lambda \delta_{ij} \nabla \cdot \boldsymbol{u}$$

$$= \begin{bmatrix} 2\mu \frac{\partial u}{\partial x} + \lambda \nabla \cdot u & \mu \left(\frac{\partial u}{\partial y} + \frac{\partial v}{\partial x} \right) & \mu \left(\frac{\partial u}{\partial z} + \frac{\partial w}{\partial x} \right) \\ \mu \left(\frac{\partial u}{\partial y} + \frac{\partial v}{\partial x} \right) & 2\mu \frac{\partial v}{\partial y} + \lambda \nabla \cdot u & \mu \left(\frac{\partial v}{\partial z} + \frac{\partial w}{\partial y} \right) \\ \mu \left(\frac{\partial u}{\partial z} + \frac{\partial w}{\partial x} \right) & \mu \left(\frac{\partial v}{\partial z} + \frac{\partial w}{\partial y} \right) & 2\mu \frac{\partial w}{\partial z} + \lambda \nabla \cdot u \end{bmatrix} \qquad (2.33)$$

where, μ is the viscosity and λ is the coefficient of bulk viscosity.

By integrating equation (2.32) over the elementary control volume, and applying equations (2.22)-(2.27), we can obtain,

$$\rho_f \frac{\partial \langle u_i \rangle}{\partial t} + \rho_f \frac{\partial}{\partial x_j} \frac{\langle u_j \rangle \langle u_i \rangle}{\varepsilon} = -\frac{\partial \varepsilon \langle p \rangle^f}{\partial x_i} + \varepsilon \rho_f g_i + \frac{\partial}{\partial x_j} \mu \left(\frac{\partial \langle u_i \rangle}{\partial x_j} + \frac{\partial \langle u_j \rangle}{\partial x_i} \right) + \frac{1}{V} \int_{A_{int}} \tau_{ij} dA_j - p dA_i - \rho_f \frac{\partial}{\partial x_j} \langle u_i' u_j' \rangle \quad (2.34)$$

For constant viscosity and a homogeneous fluid-saturated porous medium, the equation can be rewritten as,

$$\frac{\rho_f}{\varepsilon} \frac{\partial \langle \boldsymbol{u} \rangle}{\partial t} + \frac{\rho_f}{\varepsilon^2} \langle \boldsymbol{u} \rangle \cdot \nabla \langle \boldsymbol{u} \rangle = -\nabla \langle p \rangle^f + \rho_f g_i + \mu \nabla^2 \langle \boldsymbol{u} \rangle + S$$

$$S = \underbrace{\frac{1}{V_f} \int_{A_{int}} \tau_{ij} dA_j - p dA_i}_{total\ \ surface\ \ force} - \underbrace{\frac{\rho_f}{\varepsilon} \frac{\partial}{\partial x_j} \langle u_i' u_j' \rangle}_{inertial\ \ dispersion} \quad (2.35)$$

The first and second terms on the right hand side of the second equation in the equation (2.35) represent the volume averaged total surface force acting on the fluid in pores and inertial dispersion similar to the Reynolds stresses in turbulent flows.

The equation is now in the form of superficial velocity, which is used for experimental correlations. This body force can be associated with the experimental correlation of Forchheimer-Extended Darcy's law (equation (2.15)) [20] as,

$$S = \frac{\mu}{K} \langle \boldsymbol{u} \rangle + \frac{C \rho_f}{K^{1/2}} |\langle \boldsymbol{u} \rangle| \langle \boldsymbol{u} \rangle \quad (2.36)$$

Now the general macroscopic momentum equation for the fluid saturated porous media can be obtained as,

$$\underbrace{\frac{\rho_f}{\varepsilon}\frac{\partial\langle \boldsymbol{u}\rangle}{\partial t}}_{transient\ \ term} + \underbrace{\frac{\rho_f}{\varepsilon^2}\langle \boldsymbol{u}\rangle\cdot\nabla\langle \boldsymbol{u}\rangle}_{convective\ \ inertia\ \ term} = -\nabla\langle p\rangle^f + \rho_f g_i \underbrace{+\frac{\mu}{\varepsilon}\nabla^2\langle \boldsymbol{u}\rangle}_{Brinkman\ \ term} + \underbrace{\frac{\mu}{K}\langle \boldsymbol{u}\rangle}_{Darcy\ \ term} + \underbrace{\frac{C\rho_f}{K^{1/2}}\left|\langle \boldsymbol{u}\rangle\right|\langle \boldsymbol{u}\rangle}_{Forchheimer\ \ Term} \tag{2.37}$$

The first term on the left hand side of equation (2.37) denotes the transient term and second term of the left hand side of equation (2.37) is the convective inertia term. The brinkman term is often called as the boundary friction term, or wall friction term. The Darcy term represents viscous effects due to the porous medium. The Forchheimer term represents inertial effects of porous medium. As porosity approaches unity the permeability will approach infinity (resistance free or fluid only flow). Thus, equation (2.37) becomes Nervier-stokes equation. By neglecting the left hand side of the equation, the right hand side becomes the Brinkman-Forchheimer-Extended Darcy model, as shown in equation (2.18).

The equation (2.37) can also be described with pore velocity,

$$\underbrace{\rho_f\frac{\partial\langle \boldsymbol{u}\rangle^f}{\partial t}}_{transient\ \ term} + \underbrace{\rho_f\langle \boldsymbol{u}\rangle^f\cdot\nabla\langle \boldsymbol{u}\rangle^f}_{convective\ \ inertia\ \ term} = -\nabla\langle p\rangle^f + \rho_f g_i \underbrace{+\mu\nabla^2\langle \boldsymbol{u}\rangle^f}_{Brinkman\ \ term} + \underbrace{\frac{\mu}{K}\varepsilon\langle \boldsymbol{u}\rangle^f}_{Darcy\ \ term} + \underbrace{\frac{C\rho_f}{K^{1/2}}\varepsilon^2\left|\langle \boldsymbol{u}\rangle^f\right|\langle \boldsymbol{u}\rangle^f}_{Forchheimer\ \ Term} \tag{2.38}$$

Equation (2.38) describes the conservation of momentum only for the pore region inside of the solid matrix. Equation (2.37) is preferable considering all of the experimental correlations are based on this superficial velocity.

The imaginary micro-channel filled with a solid matrix (Fig. 2.3) can be thought to see the physical meaning of $-\nabla\langle P\rangle^f$. Considering the flow inside of the pore, the velocity and pressure can be related as,

$$\langle u\rangle^f \sim \Delta\langle P\rangle^f \tag{2.39}$$

Now, the superficial velocity $\langle u\rangle$ can be related with equation (2.39) and using equation (2.21).

$$\langle u\rangle/\varepsilon = \langle u\rangle^f \sim \Delta\langle P\rangle^f \tag{2.40}$$

Thus,

$$\langle u\rangle \sim \varepsilon\Delta\langle P\rangle^f \tag{2.41}$$

Since the physically measurable pressure is only $\langle P\rangle^f$, the pore pressure $\langle P\rangle^f$ is used in equation (2.37).

2.9 Volume Averaged Energy Equation

There can be two approaches for obtaining the energy equations. One is treating the fluid phase and solid phase as one medium, as we did for the momentum equation for there is no mass flux available through the interface, but in case of thermal phenomenon,

there can be heat flux through conduction. Thus, the other way is to treat the solid and fluid phases with separate energy equations. The former describes the conservation of energy with one equation; thus, it is often called the *one-equation model*. The later describes conservation of energy with two equations; thus, it is called the *two-equation model*. Two cases will be discussed later with derived equations.

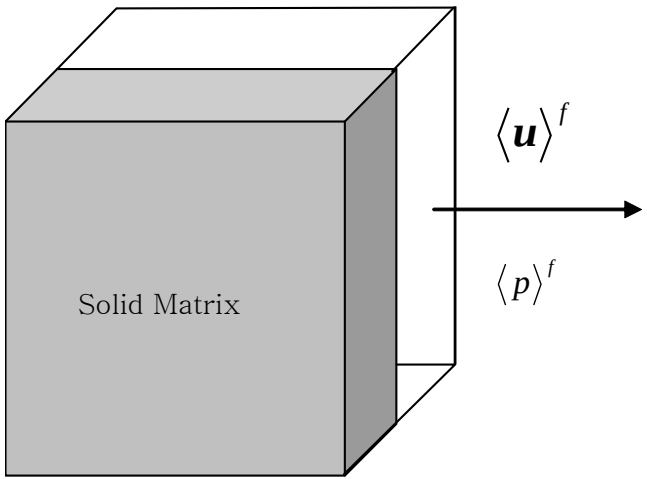

Fig. 2.3. Imaginary micro-structure.

The microscopic energy equation for fluid is given by,

$$\frac{\partial \rho_f C_{pf} T}{\partial t} + \nabla \cdot \left(\rho_f C_{pf} T \boldsymbol{u} \right) = \nabla \cdot \left(K_f \nabla T \right) \qquad (2.42)$$

where C_{pf} is the specific heat and K_f is the thermal conductivity of the fluid. Under the assumption that there is no internal heat generation and radiation effect with negligible viscous dissipation, we can use the same procedure of the volume averaging method, which will give the following equation.

$$\rho_f C_{pf}\left(\frac{\partial \varepsilon \langle T\rangle^f}{\partial t}+\langle \boldsymbol{u}\rangle\cdot\nabla\langle T\rangle^f\right) = \nabla\cdot\left(K_f\nabla\varepsilon\langle T\rangle^f+\frac{1}{V}\int_{A_{int}}K_f T d\boldsymbol{A}-\rho_f C_{pf}\langle T'\boldsymbol{u}'\rangle\right)+\frac{1}{V}\int_{A_{int}}K_f\nabla T\cdot d\boldsymbol{A} \quad (2.43)$$

Similarly, the microscopic energy equation for the solid phase can be derived as,

$$\rho_s C_s\frac{\partial(1-\varepsilon)\langle T\rangle^s}{\partial t}=\nabla\cdot\left\{K_s\nabla(1-\varepsilon)\langle T\rangle^s-\frac{1}{V}\int_{A_{int}}K_s T d\boldsymbol{A}\right\}-\frac{1}{V}\int_{A_{int}}K_f\nabla T\cdot d\boldsymbol{A} \quad (2.44)$$

where the superscript s denotes the solid matrix and $\langle T\rangle^s$ is an intrinsic average of the solid temperature. Physical properties $K_f T$ and $K_s T$ are interacting through the surface area of each side, and these terms account for thermal diffusion due to the micro-structure. The last term in equation (2.43) and equation (2.44) account for the heat transfer through the surface area.

2.9.1 One-Equation Model and Local Thermal Equilibrium

Unless the velocity of flow is very high or the conductivity ratio is high, it is generally known that the temperature between two phases (or two medium) is almost identical at a given time. That is referred as local thermal equilibrium condition (LTE).

$$\langle T \rangle^f = \langle T \rangle^s \tag{2.45}$$

If the local thermal equilibrium holds, the two equations (2.43) and (2.44) can be combined into one equation as,

$$\begin{aligned} &\left\{ \varepsilon \rho_f C_{pf} + (1-\varepsilon) \rho_s C_s \right\} \frac{\partial \langle T \rangle^f}{\partial t} + \rho_f C_{pf} \langle \boldsymbol{u} \rangle \cdot \nabla \langle T \rangle^f \\ &= \nabla \cdot \left(\left\{ \varepsilon K_f + (1-\varepsilon) K_s \right\} \nabla \langle T \rangle^f + \underbrace{\frac{1}{V} \int_{A_{int}} \left(K_s - K_f \right) T d\boldsymbol{A}}_{tortuosity\ term} - \underbrace{\rho_f C_{pf} \langle T' \boldsymbol{u}' \rangle}_{mechnical\ \ dispersion} \right) \end{aligned} \tag{2.46}$$

The first term on the right hand side consists of what is generally known as effective conductivity. The tortuosity term accounts for the transport of thermal properties through the interfacial surface. The last term is analogous to heat transfer flux in turbulent convection and accounts for contributions from mechanical dispersion.

The first two terms on the right hand side, which accounts for the molecular diffusion, can be modeled as

$$\left\{ \varepsilon K_f + (1-\varepsilon) K_s \right\} \nabla \langle T \rangle^f + \frac{1}{V} \int_{A_{int}} \left(K_s - K_f \right) T d\boldsymbol{A} = -K_{eff} \nabla \langle T \rangle^f \tag{2.47}$$

The tortuosity term usually vanishes with a constant value of $\left(K_s - K_f \right) T$, but the high thermal conductivity of the solid matrix can increase the over all heat transfer. Due to this heat transfer mechanism, it cannot be neglected in such a case, but generally it is accepted that the following model is valid except for those cases.

$$\left\{\varepsilon K_f + (1-\varepsilon)K_s\right\} \approx K_{eff} \tag{2.48}$$

The mechanical dispersion term can be modeled using the similarity of a gradient-type diffusion hypothesis as,

$$\rho_f C_{pf} \left\langle T'\boldsymbol{u}'\right\rangle = -\boldsymbol{K}_d \cdot \nabla \left\langle T\right\rangle^f \tag{2.49}$$

Thus, the macroscopic energy equation can be written as,

$$\begin{aligned} &\left\{\varepsilon\rho_f C_{pf} + (1-\varepsilon)\rho_s C_s\right\}\frac{\partial \left\langle T\right\rangle^f}{\partial t} + \rho_f C_{pf}\left\langle \boldsymbol{u}\right\rangle \cdot \nabla \left\langle T\right\rangle^f \\ &= \nabla \cdot \left(K_{eff} \nabla \left\langle T\right\rangle^f\right) + \nabla \cdot \left(\boldsymbol{K}_d \cdot \nabla \left\langle T\right\rangle^f\right) \end{aligned} \tag{2.50}$$

As an attempt to evaluate the dispersion conductivity, Rubin pointed out that the second order tensor, $\boldsymbol{K}_d$, is axisymmetric for isotropic porous media. Nakayama [17] noted that from a scale analysis, it may be assumed as,

$$K_{d,xx} \sim K_{d,yy} \sim K_{d,zz} \sim \rho_f C_{pf} \sqrt{K} u \tag{2.51}$$

The transverse dispersion is known to be larger than the longitudinal dispersion [20] and it is suggested that,

$$3K_{d,xx} \sim K_{d,yy} \sim K_{d,zz} \tag{2.52}$$

This approach usually requires only one equation to solve for the averaged temperature of local volume. Thus, it is usually called a one-equation model [20].

2.9.2 Two-Equation Model and Local Thermal Non-Equilibrium

When the flow is in the high *Re* range or the conductivity between the fluid and solid matrix is high, equation (2.45) no longer holds. From equation (2.43) for the fluid phase,

$$\rho_f C_{pf}\left(\frac{\partial \varepsilon \langle T\rangle^f}{\partial t}+\langle \boldsymbol{u}\rangle\cdot\nabla\langle T\rangle^f\right)=\nabla\cdot\left(K_f\nabla\varepsilon\langle T\rangle^f-\rho_f C_{pf}\langle T'\boldsymbol{u}'\rangle\right)+\frac{1}{V}\left(\nabla\cdot\int_{A_{int}}K_f T d\boldsymbol{A}+\int_{A_{int}}K_f\nabla T\cdot d\boldsymbol{A}\right) \quad (2.53)$$

From equation (2.44),

$$\rho_s C_s\frac{\partial(1-\varepsilon)\langle T\rangle^s}{\partial t}=\nabla\cdot\left\{K_s\nabla(1-\varepsilon)\langle T\rangle^s\right\}-\frac{1}{V}\left(\nabla\cdot\int_{A_{int}}K_s T d\boldsymbol{A}+\int_{A_{int}}K_s\nabla T\cdot d\boldsymbol{A}\right) \quad (2.54)$$

The term $-\rho_f C_{pf}\langle T'\boldsymbol{u}'\rangle$ can be modeled using equation (2.49). Then the last terms in equation (2.53) and (2.54) can be written as,

$$\frac{1}{V}\left(\nabla\cdot\int_{A_{int}}K_f T d\boldsymbol{A}+\int_{A_{int}}K_f\nabla T\cdot d\boldsymbol{A}\right) \quad (2.55)$$

$$-\frac{1}{V}\left(\nabla\cdot\int_{A_{int}}K_s T d\boldsymbol{A}+\int_{A_{int}}K_s\nabla T\cdot d\boldsymbol{A}\right) \quad (2.56)$$

Now, the left hand side terms of the groups (2.55) and (2.56) represent heat flux between the fluid phase and the solid phase due to the conductivity and temperature difference. The temperature difference due to the high conductivity difference can be

explained using this relationship. The last term denotes heat flux from the fluid phase to the solid phase through the surface area between the two phases. Since the ratio of conductivity between the fluid phase and the solid phase is large ($K_s / K_f \approx 10,000$), these terms are no longer negligible.

While it is rarely available to obtain the correlation or experimental research to describe these terms in turbulent flow, it is available to adopt experimental correlations for one-dimensional sluggish flow through sintered beads.

Dixon and Criswell [29] investigated local thermal non-equilibrium (LTNE) between the two phases and were the first to obtain a fluid to solid heat transfer correlation. Researchers [26, 29, 30] have presented their own correlations and employed [11, 31] the two separate equations for each phases to explain the heat transfer between two phases.

These terms can be modeled as the temperature difference between two phases and interfacial heat transfer coefficient (h_{sf}) as follows,

$$\frac{1}{V}\left(\nabla \cdot \int_{A_{int}} K_f T d\boldsymbol{A} + \int_{A_{int}} K_f \nabla T \cdot d\boldsymbol{A} \right) = h_{sf} A_{int} (T_s - T_f) \qquad (2.57)$$

$$-\frac{1}{V}\left(\nabla \cdot \int_{A_{int}} K_s T d\boldsymbol{A} + \int_{A_{int}} K_s \nabla T \cdot d\boldsymbol{A} \right) = h_{sf} A_{int} (T_f - T_s) \qquad (2.58)$$

The interfacial heat transfer coefficients must be modeled to incorporate this model. Among others, Hwang and Chao [11] presented the following relationships.

$$h_{sf} = 0.0040\left(\frac{K_f}{d_v}\right)\left(\frac{d_v}{d_p}\right)^{1.35} Pr_f^{1/3} Re_d^{1.35} (Re_d < 100) \quad (2.59)$$

$$h_{sf} = 0.0156\left(\frac{K_f}{d_v}\right)\left(\frac{d_v}{d_p}\right)^{1.04} Pr_f^{1/3} Re_d^{1.04} (Re_d \geq 100) \quad (2.60)$$

And,

$$A_{int} = 20.346(1-\varepsilon)\varepsilon^2 / d_p \quad (2.61)$$

where Re_d is Reynolds number based on the particle diameter.

Wakao and Funazkri [46] suggested and Amiri and Vafai [47] used the following model,

$$h_{sf} = K_f (2 + 1.1 Pr^{1/3} Re_p^{0.6}) / d_p \quad (2.62)$$

$$A_{int} = 6(1-\varepsilon) / d_p \quad (2.63)$$

Recently, Fourie and Du Plessis [48] developed another form of the two-equation model using a separate interfacial conductivity theory.

However, all of the mentioned research is based on a saturated packed bed type configuration, and the two-equation model approach entails the wall boundary problem.

CHAPTER III

EXPERIMENTAL SETUP AND PROCEDURE

3.1 Introduction

The objective of this experiment was to build a set of experimental data under the influence of various conditions in a three dimensional channel with porous baffles. Module averaged Nusselt numbers and friction factors were measured for the flow in staggered porous baffled channels. A qualitative analysis was carried out after the experimental data set was obtained.

3.2 The Uniqueness of the Experimental Investigation

It is clear from reviewing the literature that the work of Hwang [5] is the only work similar to the one presented in this dissertation. However, the present work differs from that of Hwang [5] in that the nature of the experiments and the scope of the parameters are quite different. The major difference is the geometric configuration such that Hwang focused on a 2-D plane and localized data, but the present experiment focused more on the module averaged values and therefore including the 3-D phenomenon.

Other significant differences include: (a) in the present study the test section was heated along all four walls, whereas in the previous case [5] only the top wall was heated; (b) Hwang [5] reported local heat transfer data along the centerline of the channel, whereas in the present work the focus is on measuring the module average

Nusselt number; (c) in the present work, experiments were conducted with three (3) different pore densities (viz.: 10 PPI, 20 PPI, and 40 PPI), whereas in the previous case [5] the porosity was held constant at 0.42; (d) the present set of experiments were conducted with porous baffles with two different thicknesses (1" and 0.25") whereas in the previous case [5] the baffle thickness was not varied; (e) the results of the present work is representative of a three-dimensional flow situation (aspect ratio H/W = 1) whereas the results of the previous case better represents a two-dimensional situation (aspect ratio H/W = 0.25); and (f) in the present work the material used for the baffles is an aluminum foam manufactured using a process patented by ERG Aerospace, Inc., California (See Fig. 3.1), whereas in the previous case [5], porous baffles were made of sintered bronze beads. Thus the scope of the present study is very different than that of Hwang [5]. In the following sections, a description of the experimental test setup, associated instrumentation, experimental procedure, uncertainty analysis, range of independent parameters, and representative results will be discussed.

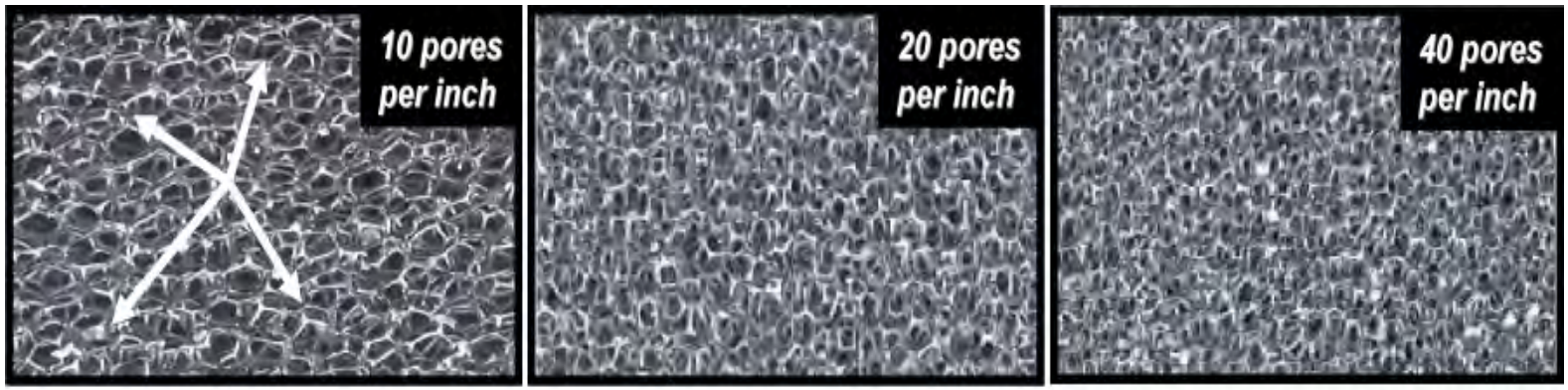

Fig. 3.1. Samples of the porous material.

3.3 Experimental Setup

Fig. 3.1 shows samples of the porous material which were used for the experiments. Because the current material has a uniform pore density, it is described by the distribution of pores per inch. (PPI). The materials selected for the experiments were 10 PPI, 20 PPI, and 40 PPI. The physical properties of these materials are listed on Table 3.1

Table 3.1
Material properties [12]

Aluminum foam	**(A) 10PPI**	**(B) 20PPI**	**(C) 40PPI**
Materials	Al-6101	Al-6101	Al-6101
Porosity, ε	0.92	0.92	0.92
Pore density (PPI)	10	20	40
Permeability, K (m^2)	1.04E-7	0.76E-7	0.51E-7
Darcy number, $Da=K/H^2$	1.3E-3	9.4E-4	6.3E-4
Surface area to volume ratio (m^2/m^3)	790	1720	2740
Effective thermal conductivity, k_ε (W/m K)	5.33	5.56	6.01

Fig. 3.2 shows the schematic diagram of the experimental setup. It consists of four major components: (a) the flow system, (b) baffled test section, (c) heating unit, and (d) measurement system.

The flow system was operated in suction mode and oriented horizontally. Air drawn through the channel entrance, flows through the baffled test section, the mixing chamber, the flow meter, and is then exhausted by two serially linked 1.5 hp blowers. The connection between the blowers and the test setup was made with a flexible high pressure vacuum tube to minimize vibration. A control valve was used to control the flow rate. An orifice flow meter was used downstream of the mixing chamber to measure airflow rate. A mixing chamber was located downstream of the test section to stabilize the flow. The open test loop had an entrance length of 48". A long entry region was provided so that the flow would be fully developed as it enters the baffled section.

Fig. 3.3 shows the details of the test section. The test section has a 3" × 3" (H × W) square cross-sectional area and a length of 36" (L_T). Baffles were located in a staggered manner by mounting the baffles alternately on the top and bottom walls. The baffles were firmly glued to the walls using thermal epoxy. The distance between two successive baffles (pitch, B_p) was 3" and was maintained constant throughout this study. To facilitate the flow to develop as it enters the test section; two unheated baffles were set in front of the heated baffles. The entrance length is sufficiently long to ensure the flow is fully developed at the entrance to the test section.

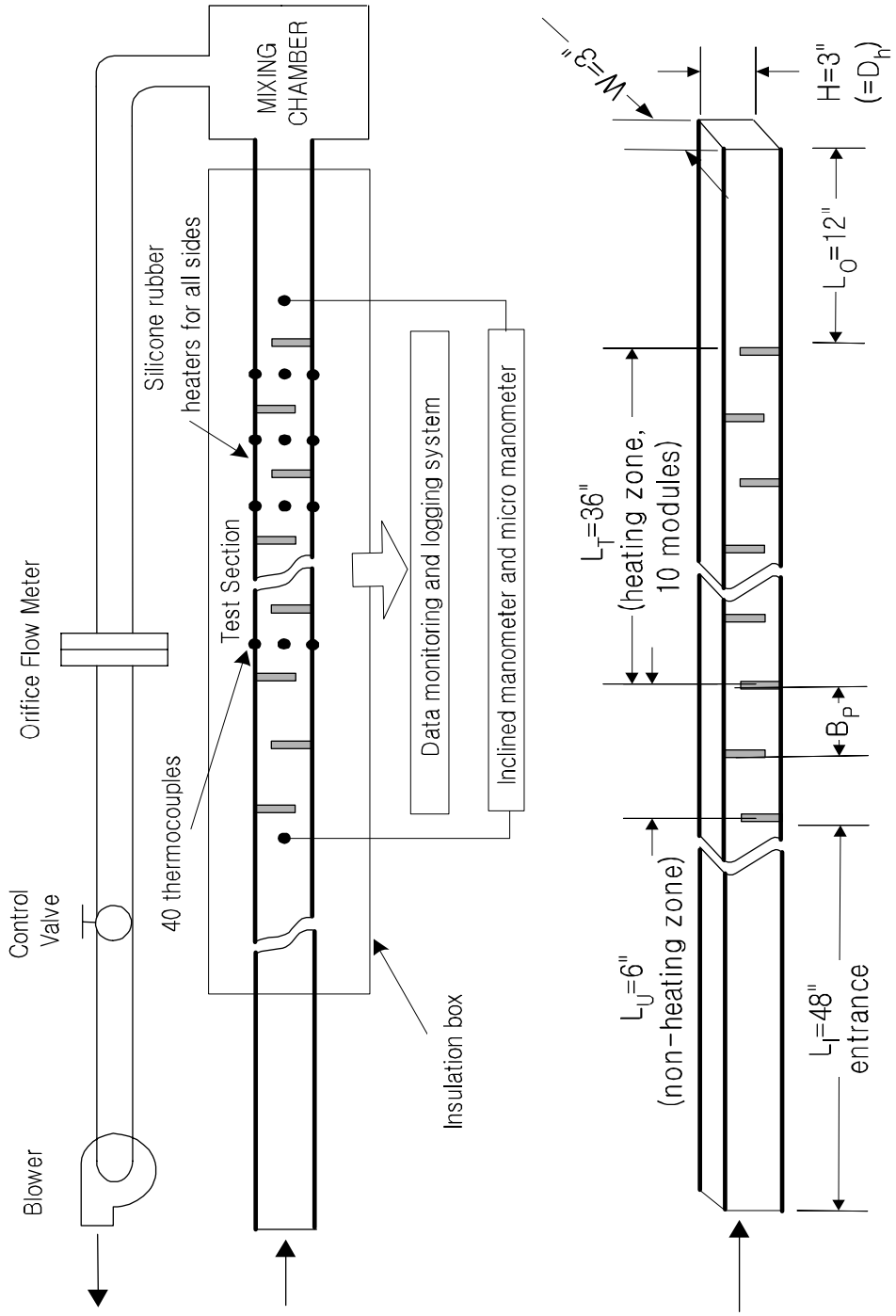

Fig. 3.2. Schematic diagram of the experimental set-up.

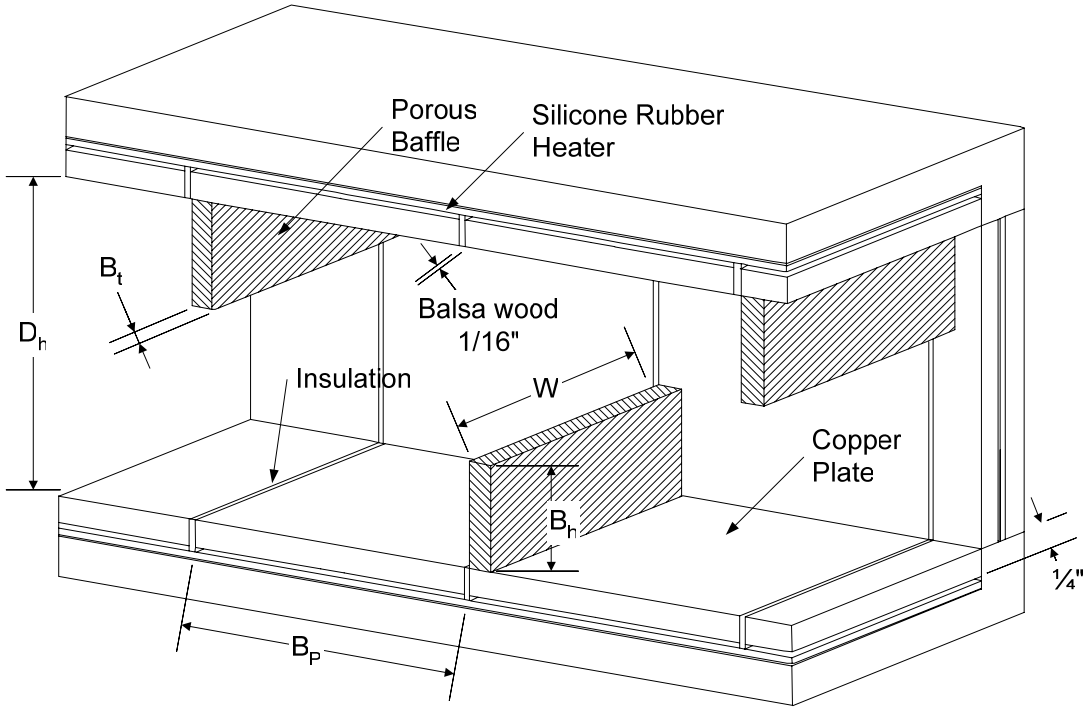

Fig. 3.3. Schematic of the test section.

The test section was built with 40 (3" × 3") copper plates (Fig. 3.4). T-type (Copper-Constantine) thermocouples with Teflon insulation were carefully inserted in drilled holes underneath the surface of each plate to measure the average temperature of each plate. Silver paint was used to ensure proper contact between the thermocouples and the copper plates. These contacts were electronically checked using an Ohm meter. In the stream-wise direction, each plate was separated by balsa wood to ensure insulation from each other. The back-side of each plate was attached to a silicone rubber heater with a thin layer of highly conductive silicone. The square channel was well insulated on the outside using four-inch (4") thick fiberglass insulation, and placing the test section

and insulation in a wooden box. Silicone rubber heaters on each side were connected in parallel and powered through a transformer; the temperature of the test section was controlled by a Watlow Auto-Tuning Controller.

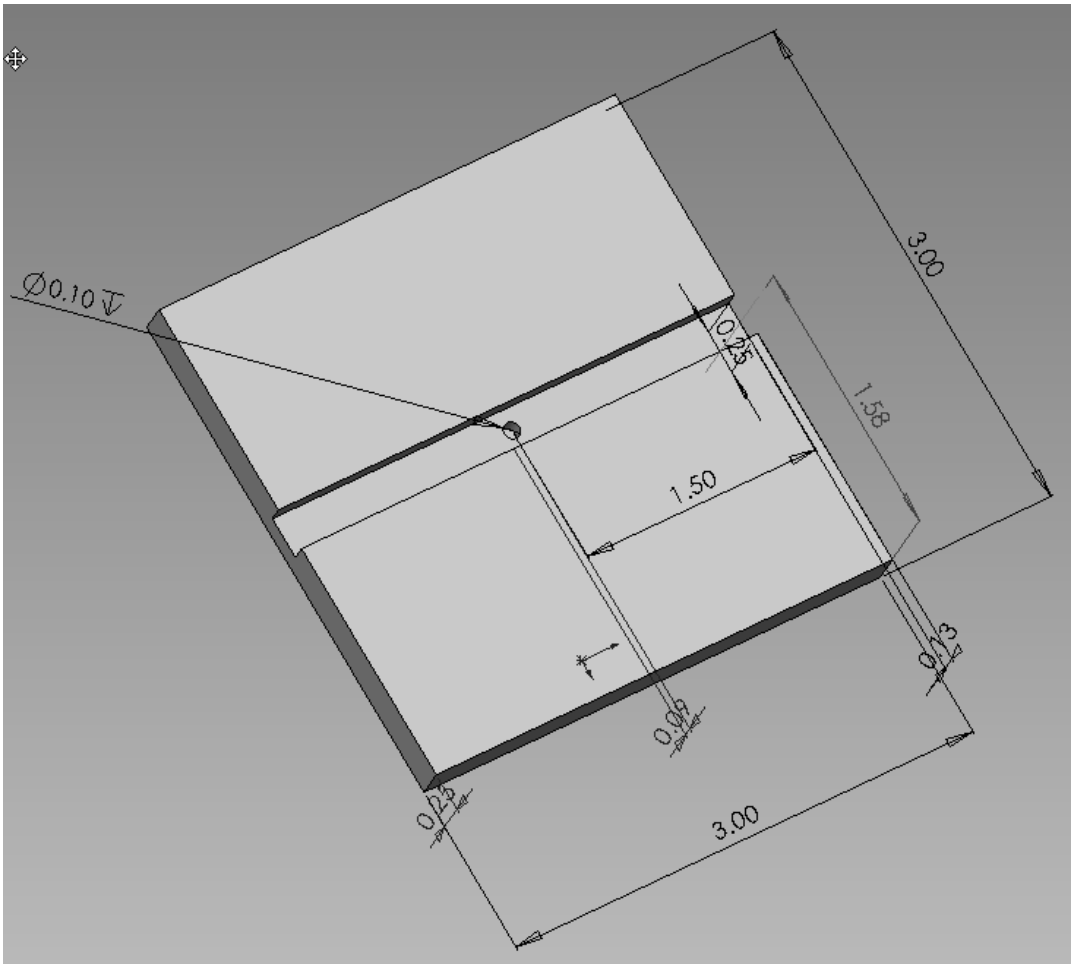

Fig. 3.4. Copper plate dimensions.

Fig. 3.5. Attached copper plates.

Fig. 3.5 shows the photograph of the assembled copper plates. The completed experimental setup can be seen in Fig. 3.6.

3.4 Instruments and Calibration

The Copper-Constantine thermocouples were calibrated against the Fischer thermal bath with a variation of 0.1°F or less over the range of operating temperatures in this study. The range of Reynolds numbers examined in this study were Re = 20,000-50,000. The flow Reynolds numbers were calculated by measuring the flow rate. The

flow rates were measured by an orifice meter using the 1.5" orifice plate made by Daniel Measurement and Control, Inc. The U-type water manometer and inclined oil manometer were used to measure pressure drop across the orifice plate. The pressure taps were located at a distance of 1.5" on either side of the test section.

Fig. 3.6. Photographs of the experimental setup.

The pressure drop in a straight channel (without baffles) was measured with a micro-manometer for higher accuracy and an inclined manometer was used for the baffled channel. Total power applied to the test section was calculated using the voltage and current measured using a multi-meter, which had a factory precision of 2.5% and 2%, respectively. Various temperatures were monitored using a computer-controlled data acquisition system. The maximum temperature was limited and controlled by a Watlow auto controller until the system reached steady state for more than 10 minutes with less than 0.5°F variations in temperatures.

3.5 Data Reduction

3.5.1 Data Reduction of Mass Flow

The Reynolds number based on the hydraulic diameter was evaluated as,

$$\mathrm{Re} = \frac{\rho U D_h}{\mu} = \frac{4\dot{m}}{\pi \mu D_h} \qquad (3.1)$$

where, U and $\dot{m}$ are the average velocity and mass flow rate of air in the test section. The discharge coefficient (C_d) of the orifice meter can be evaluated using the orifice meter formula,

$$C_D = F(\beta) + 91.71\beta^{2.5}\,\mathrm{Re}_{D_p}^{-3/4} + \left\{\frac{0.09\beta^4}{1-\beta^4}F_1 - 0.0337F_2\beta^3\right\}$$
$$f(\beta) = 0.5959 + 0.0312\beta^{2.1} - 0.184\beta^8 \qquad (3.2)$$
$$F_1 = 0.4333,\quad F_2 = 0.47$$

It is known that the accuracy of this formula is ±0.6% for $0.2<\beta<0.75$ and for $10^4<\mathrm{Re}_{D_p}<10^7$. Thus the Mass flow rate can be evaluated using equation (3.3),

$$\dot{m} = (\pi/4)d^2 C_d \left(\frac{2\Delta P}{\rho(1-\beta^4)}\right)^{0.5}$$
$$= (\pi/4)(1.5\times 0.0254)^2 C_d \left(\frac{2\cdot(P_1+101300)\Delta P}{287\cdot(T_{out}+273.15)(1-0.6^4)}\right)^{0.5} \qquad (3.3)$$

The corresponding Reynolds number can be evaluated using equation (3.4),

$$Re_{D_p} = \frac{\dot{m}}{A}\frac{D_p}{\mu} = \frac{4\dot{m}}{\pi D_p \mu} \quad \left\{\dot{m} = A\rho V,\ \mathrm{Re}_{D_p} = \rho V\frac{d}{\mu}\right\} \qquad (3.4)$$

For given P_1 *and* ΔP, equation (3.3) and equation (3.4) can be solved iteratively to obtain the appropriate value. Since the Reynolds number here is based on the hydraulic diameter of the circular pipe, the corrected Reynolds number can be evaluated using equation (3.5),

$$Re_h = \frac{\dot{m}D_h}{A\mu} = \left(\frac{4A}{P}\right)\frac{1}{A}\frac{\dot{m}}{\mu} = \frac{4\dot{m}}{P\mu} \qquad (3.5)$$

3.5.2 Data Reduction of Friction Factor

The friction factor in a periodically fully developed baffled channel flow can be determined by measuring the pressure drop across the flow channel and the average air velocity. The average friction factor can then be calculated from

$$f = \frac{(\Delta P / L) D_h}{\rho U^2 / 2} \qquad (3.6)$$

where, L denotes the distance between pressure taps.

3.5.3 Heat Loss Compensation

Before the calculation of the heat transfer related properties of the test section, if one important factor has to be mentioned it could be the heat loss compensation. By taking the heat loss compensation into consideration, the error in heat transfer measurements due to wall conduction can be taken into account.

Since the insulation for the experimental setup is not perfect while the insulated test section has been under the operating conditions of the experiment, especially temperature, it tends to lose the heat through the wall. The amount of the heat lost from the test section by conduction can be estimated under the following assumption. The conduction loss through the wall for one module is linearly dependant on the temperature of the surface of the module. Throughout the entire experiment the operating temperature should not exceed the temperature condition of the heat loss compensation.

The linear dependency can be expressed as equation (3.7),

$$q''_{loss,i}[W/m^2] = a_i(T_{wall,i} - T_{in}[°C]) + b_i \qquad (3.7)$$

where, a_i and b_i is the arbitrary coefficients which will be determined by compensation experiment.

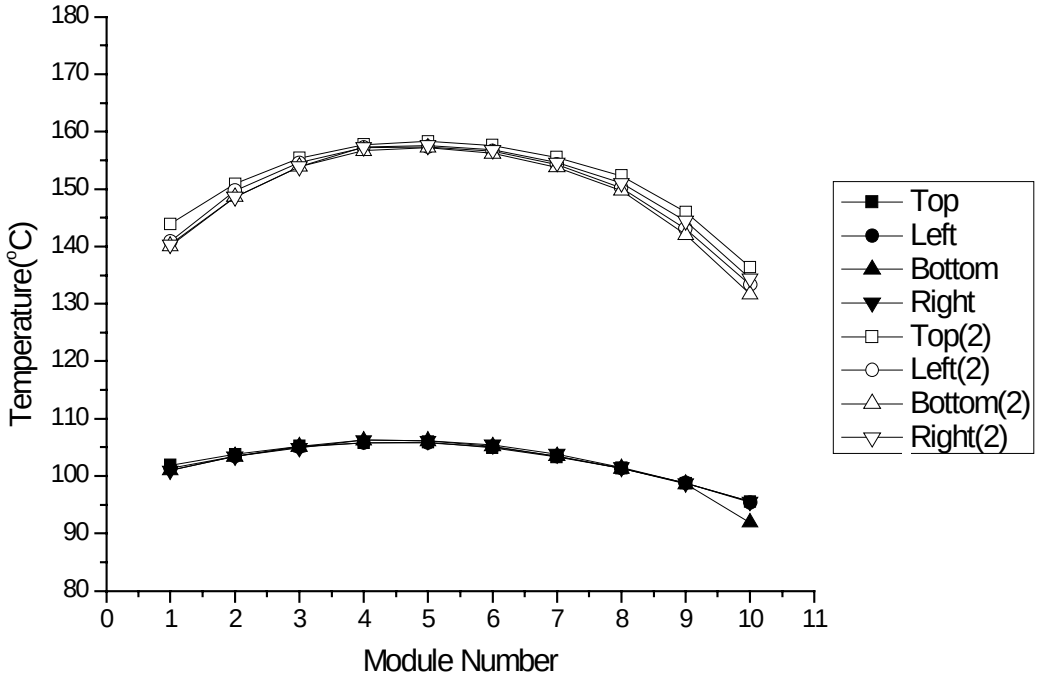

Fig. 3.7. Temperature distribution for heat loss test (Re=0).

Since the problem is how much heat is lost through the conduction under a certain operating condition it can be indirectly calculated by putting a small amount of power into the setup while both the inlet and outlet are closed (so that there is no convective loss). The power will increase the temperature of the test section. If the test section is perfectly insulated then the temperature of the test section will increase monotonically. If the test section shows steady state condition of temperature, then we can assume that under the certain temperature conditions the wall is losing a specific amount of heat. While the relationship cannot be linear, for the sake of ease in processing, the linear variation is assumed.

Fig. 3.7 shows the result of the temperature distribution experiment. The upper group shows the higher temperature due to high power input and the lower group of curves shows the lower temperature. The temperature of the module is varying depending on its location. Lower temperatures for the inlet and outlet region gives the idea of more heat loss in these areas. Fig. 3.8 shows the example of how the heat loss would be determined while the experiments were conducted.

The coefficients a_i and b_i can be determined using the data such as Fig. 3.7. The example set of the coefficients determined using equation (3.7) is shown in Table 3.2. Each of them represents the coefficient for the independent plates.

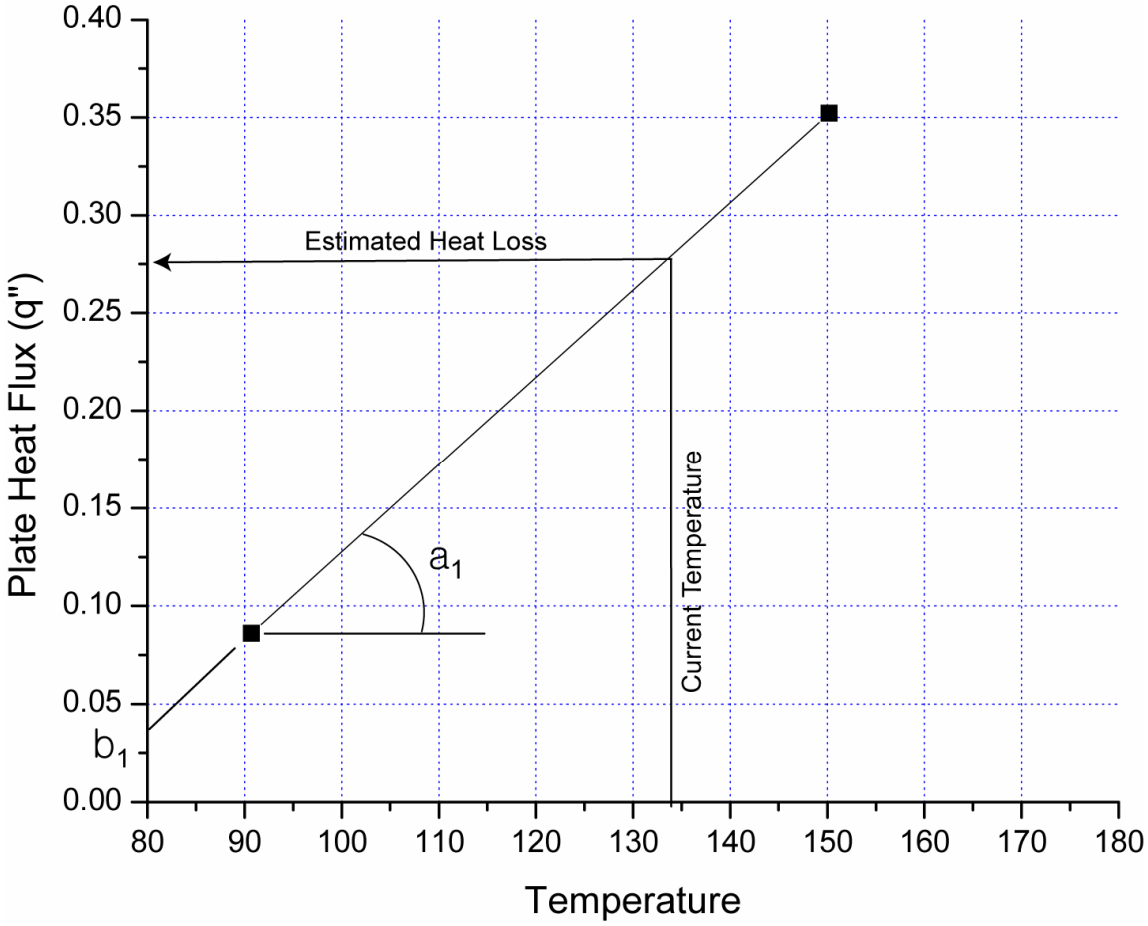

Fig. 3.8. Determination of heat loss for a plate using the linear assumption.

Table 3.2
Coefficients for the heat loss compensation for each module

a	#1	#2	#3	#4	#5	#6	#7	#8	#9	#10
Top(1)	1.13E-02	1.00E-02	9.37E-03	9.06E-03	8.97E-03	8.92E-03	9.01E-03	9.24E-03	9.96E-03	1.16E-02
Left(2)	1.20E-02	1.02E-02	9.49E-03	9.15E-03	9.13E-03	9.11E-03	9.26E-03	9.63E-03	1.07E-02	1.25E-02
Bottom(3)	1.21E-02	1.04E-02	9.65E-03	9.32E-03	9.20E-03	9.22E-03	9.35E-03	9.73E-03	1.09E-02	1.19E-02
Right(4)	1.20E-02	1.04E-02	9.61E-03	9.20E-03	9.13E-03	9.15E-03	9.26E-03	9.51E-03	1.03E-02	1.22E-02
Average	4.73E-02	4.10E-02	3.81E-02	3.67E-02	3.64E-02	3.64E-02	3.69E-02	3.81E-02	4.18E-02	4.81E-02
b										
Top(1)	-9.13E-02	-8.19E-02	-7.84E-02	-7.58E-02	-7.47E-02	-6.88E-02	-6.23E-02	-5.65E-02	-5.29E-02	-5.62E-02
Left(2)	-9.85E-02	-8.26E-02	-7.94E-02	-7.74E-02	-7.71E-02	-7.27E-02	-6.76E-02	-6.21E-02	-6.34E-02	-6.62E-02
Bottom(3)	-9.90E-02	-8.69E-02	-8.27E-02	-8.25E-02	-8.00E-02	-7.57E-02	-6.92E-02	-6.37E-02	-6.54E-02	-3.55E-02
Right(4)	-9.80E-02	-8.69E-02	-8.10E-02	-8.05E-02	-7.86E-02	-7.54E-02	-6.92E-02	-6.13E-02	-5.80E-02	-6.28E-02
Average	-3.86E-01	-3.38E-01	-3.21E-01	-3.16E-01	-3.10E-01	-2.92E-01	-2.68E-01	-2.43E-01	-2.39E-01	-2.20E-01

3.5.4 Data Reduction of Heat Transfer

The average heat transfer coefficient for the i_{th} copper segment (i = 1 to 40) is

$$h_i = \frac{Q_i}{A_s(\bar{T}_w - \bar{T}_b)} = \frac{Q_p - Q_{loss,i}}{A_s(\bar{T}_w - \bar{T}_b)} \qquad (3.8)$$

where A_s is the area of the inner surface of the plate segment. $\bar{T}_w$ is the average wall temperature. $\bar{T}_b$ is the bulk temperature calculated from an energy balance, $\bar{T}_b = \bar{T}_{in} + Q_i / (\dot{m} \times C_p)$, and Q_i is the actual amount of heat applied to the i_{th} module. Q_i is estimated by subtracting the heat loss ($Q_{loss,i}$) from the electrical input. Thus the average Nusselt number for each plate is calculated as

$$\overline{Nu}_p = \frac{h_i D_h}{K_f} \qquad (3.9)$$

Each module is made of four plates i.e. top, bottom, left, and right. Then the average module Nusselt number ($\overline{Nu_m}$) can be calculated as the weighted average of the Nusselt numbers ($\overline{Nu_p}$) for each plate. The weighting factors are the areas of each plate.

3.6 Uncertainty Analysis

A detailed uncertainty analysis was conducted. The variables measured were temperature, pressure drop, and heat applied to each module. The uncertainty associated with each variable is the square root sum of the squares of precision and bias errors. The bias error was found to be negligibly small compared to the precision errors, accordingly the bias errors associated with each variable was neglected.

The measurement of the airflow rate using the orifice plate involved the measurement of pressure drop and discharge coefficient. For the current configuration of the β = 0.6 (ratio of the orifice diameter to the pipe diameter) and Reynolds number range of 20,000 to 50,000, the maximum error for the discharge coefficient is reported as 0.6% [49, 50]. Considering the maximum uncertainty of pressure, the uncertainty of mass flow from the orifice meter is estimated to be less than 1.3%.

The precision error associated with heat applied to each module stems from the voltage and current measurements. Precision errors associated with voltage and current measurements were provided by the instrument manufacturer and were 2% and 2.5%, respectively.

According to McClintock [50] and the ANSI Guide to the Expression of Uncertainty in Measurement [51], Uncertainty of a function which has dependent variables of the form such as equation (3.10) can be expressed as equation (3.11).

$$y = f(x_1, x_2, x_3, \cdots, x_N) \tag{3.10}$$

$$u_c^2(y) = \sum_{i=1}^{N} \left(\frac{\partial f}{\partial x_i} \right)^2 u^2(x_i) \tag{3.11}$$

where, $u_c(y)$ denotes combined standard uncertainty and $u(y)$ denotes standard uncertainty. The average heat transfer coefficient for the module can be expressed as equation (3.12) (The dependent variables are listed in the order of their importance)

$$\overline{h_m} = f(\dot{m}, T_{wall}, T_{in}, Q_{total}, q_{m,loss}, C_p) \tag{3.12}$$

Using equation (3.11), the uncertainty of the module heat transfer can be expressed as follows,

$$\begin{aligned}
\left(\frac{u(\overline{h_m})}{\overline{h_m}}\right)^2 &= \left(\frac{1}{\overline{h_m}}\right)^2 \left(\frac{\partial f}{\partial x_i} u(x_i)\right)^2 \\
&= \left(\frac{1}{\overline{h_m}}\right)^2 \left[\begin{array}{l} \left(\frac{\partial y}{\partial \dot{m}} u(m)\right)^2 + \left(\frac{\partial y}{\partial q} u(q)\right)^2 + \left(\frac{\partial y}{\partial T_{in}} u(T_{in})\right)^2 \\ + \left(\frac{\partial y}{\partial T_{wall}} u(T_{wall})\right)^2 \end{array}\right] \\
&= \left(\frac{1}{A_m}\right)^2 \left\{\begin{array}{l} \left(\frac{{C_q}^2 C_{mi}}{{C_T}^2 \dot{m}}\right)^2 \left(\frac{u(\dot{m})}{\overline{h_m}}\right)^2 + \left(\frac{1}{C_T} - \frac{C_q C_{mi}}{{C_T}^2}\right)^2 \left(\frac{u(q)}{\overline{h_m}}\right)^2 \\ + \left(-\frac{C_q}{{C_T}^2}\right)^2 \left(\frac{u(T_{in})}{\overline{h_m}}\right)^2 + \left(\frac{C_q}{{C_T}^2}\right)^2 \left(\frac{u(T_{wall})}{\overline{h_m}}\right)^2 \end{array}\right\}
\end{aligned} \tag{3.13}$$

For detailed procedures, variable definitions, and sample calculations of the uncertainty analysis refer to appendix A.

The propagation equation of Kline and McClintock [50] and the ANSI Guide to the Expression of Uncertainty in Measurement [51] were referred to in order to calculate uncertainties associated with the friction factor (f), the module Nusselt number ($\overline{Nu_m}$), and the associated intermediate variables. The maximum uncertainty associated with the module Nusselt number measurement was 5.8% and the uncertainty associated friction factor was 4.3%.

3.7 Independent Parameters

All experiments were conducted with air; accordingly, the Prandtl number was fixed at 0.7 and adjustments were made to account for a variation of properties with the temperature. Consideration was given to a single channel aspect ratio (H/W = 1). While the porosity (ε) of the aluminum foam had a constant value of 0.92 and consideration was given to three different pore densities: 10 PPI, 20 PPI, and 40 PPI. PPI stands for pores per linear inch.

The Reynolds number was varied from 20,000 to 50,000. Experiments were conducted with two different baffle thickness values B_t / D_h = 1/3 and 1/12. Measurements were made with porous and solid baffles. In order to benchmark and validate the data, measurements were made for the case of a straight channel without baffles ($B_h / D_h = 0$). Consideration was given to a fixed value of baffle pitch (B_p = 3"). The scope of experimental study included two different baffle heights, B_h / D_h = 1/3 and 2/3. The ranges of independent parameters, explored in this study, are summarized in Table 3.3.

Table 3.3
Test parameters

Porosity(ε)	*Re*	Baffle Thickness (B_t / D_h)	Baffle Height (B_h / D_h)	Pore Density
0.92	20,000	1/3	1/3	10PPI
	30,000			10PPI
	40,000	1/12	2/3	40PPI
	50,000			Solid

CHAPTER IV

EXPERIMENTAL RESULTS AND DISCUSSION

4.1 Validation of Test Rig

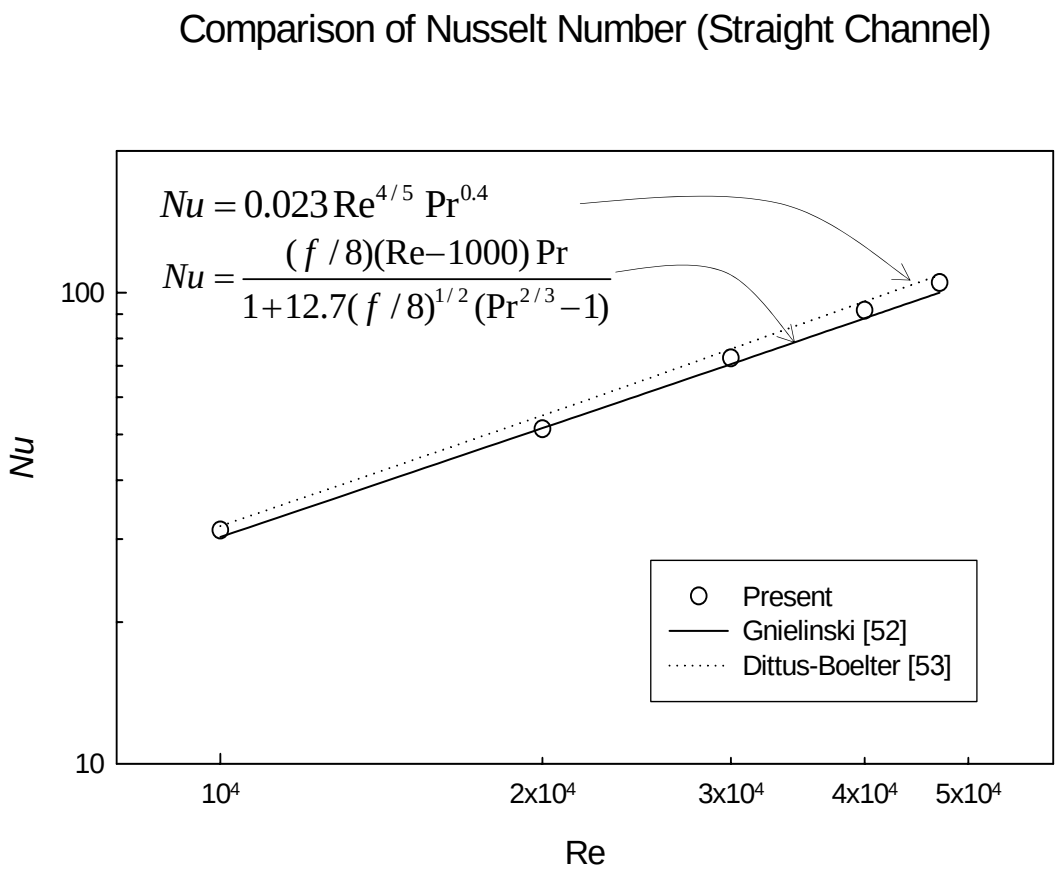

Fig. 4.1. The validation of heat transfer experiments (comparison of the Nusselt number).

The current experimental procedure was validated by making heat transfer measurements for flow through a straight channel without baffles ($B_h / D_h = 0$, Fig. 3.2) The variation of the average Nusselt number with the Reynolds number for fully developed flows in straight channels are shown in Fig. 4.1. In this figure the current experimental data is compared with the correlations available in literature. The average Nusselt number for fully developed flow in a straight channel was compared with results obtained from correlations of Gnielinski [52] and Dittus-Boelter [53]. The maximum difference for the average Nusselt number obtained in the present work and the correlations in the literature [52, 53] is 5.9%.

4.2 Heat Transfer Enhancement Ratio

Fig. 4.2 shows the module Nusselt number ($\overline{Nu}_{m,i}$) for the pore density of 20 PPI, and baffle height ratio of B_h / D_h = 1/3. In the previous work of Berner et al. [3], it was found that the flow periodically fully develops downstream of the fourth (4th) module for a thin solid baffle. Considering the baffle thickness and pore density is different from the solid baffle, it is expected that the entry length for the flow through a porous baffle channel is longer than for the flow through a solid baffle channel.

It is evident from Fig. 4.2 that the variation pattern of the average module Nusselt number repeats itself downstream of the seventh (7th) module (including baffles in unheated sections). Thus, it is clearly establishing the existence of periodically fully developed heat transfer in such porous baffled channel flows. As expected the average

module Nusselt number decreases in the downstream direction and increases with an increase in the Reynolds number.

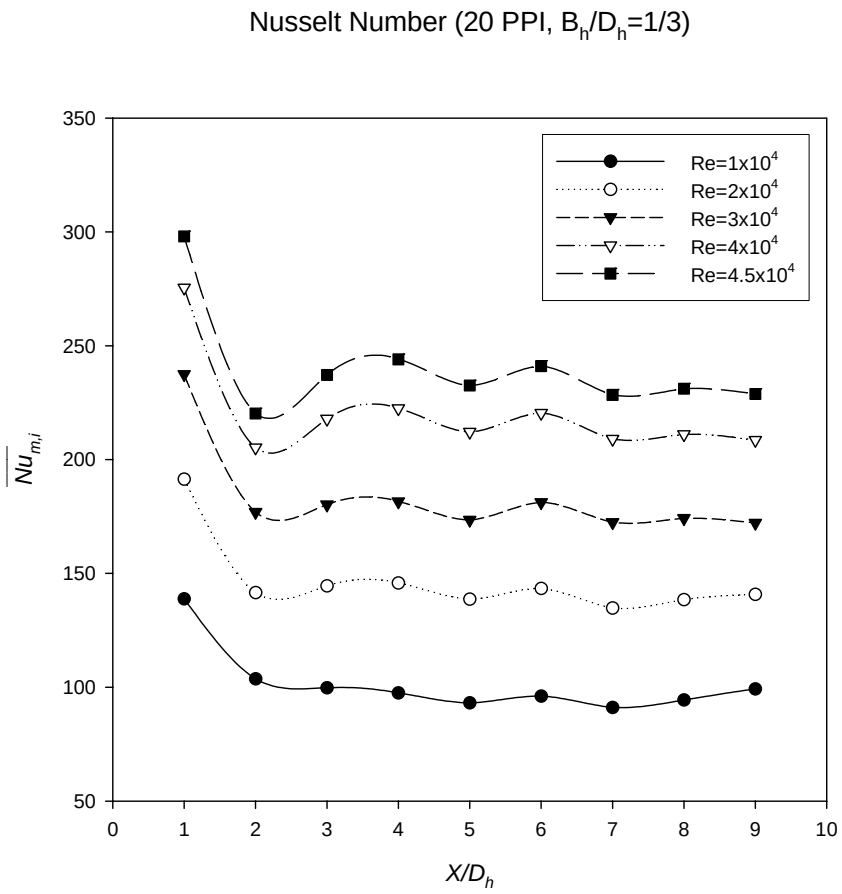

Fig. 4.2. Average module Nusselt number for 20 PPI, B_h / D_h = 1/3.

The effectiveness of using porous baffles was evaluated by studying the ratio of the average module Nusselt number ($\overline{Nu_{m,pdf}}$) for periodically fully developed flow and the average Nusselt number ($\overline{Nu_s}$) for fully developed flow in a straight channel (B_h / D_h = 0). Henceforth, this ratio will be referred as the heat transfer enhancement ratio ($\overline{Nu^+} = \overline{Nu_{m,pdf}} / \overline{Nu_s}$).

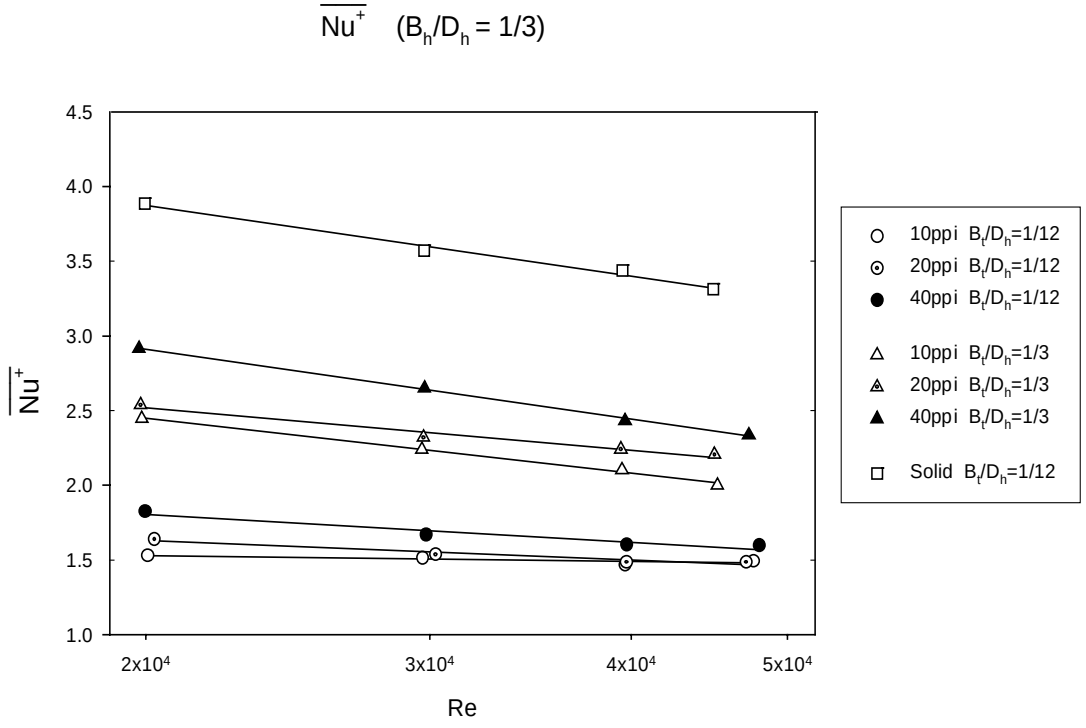

Fig. 4.3. Heat transfer enhancement ratio for B_h / D_h =1/3.

The variations of the heat transfer enhancement ratio ($\overline{Nu^+}$) and friction factor (f and f^+) with the Reynolds number for various cases are shown in Fig. 4.3 and 4.4, respectively for a fixed value of B_h / D_h = 1/3. For the case of B_h / D_h = 1/3 and for the entire range of independent parameters examined in this study, the heat transfer enhancement ratio ($\overline{Nu^+}$) is greater than unity (Fig. 4.3), signifying that the use of porous baffles over plain straight channels is advantageous. In some cases the heat transfer enhancement ratio is as high as 320%. As expected the solid baffles perform better than the porous baffles from a heat transfer point of view with an enhancement ratio as high as 400%.

The heat transfer enhancement ratio decreases with an increase in the Reynolds number. This is attributed to the fact that at higher Re values the turbulent effects play a much more dominant role than the baffle effects, such as impingement and fin effects. For a fixed pore density, the heat transfer enhancement ratio increases with an increase in baffle thickness. It is evident that the ratio $\overline{Nu^+}$ for a thicker baffle (B_t / D_h = 1/3) is consistently higher than for thinner baffles (B_t / D_h = 1/12). This behavior is expected as the thicker baffle provides a greater convection and diffusion heat transfer area.

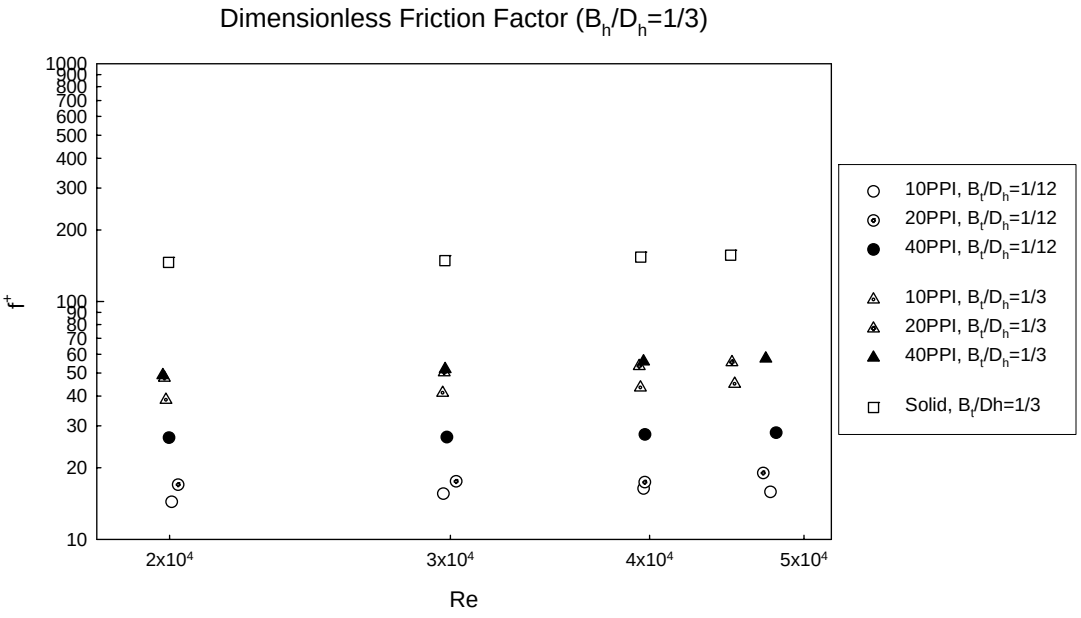

(a)

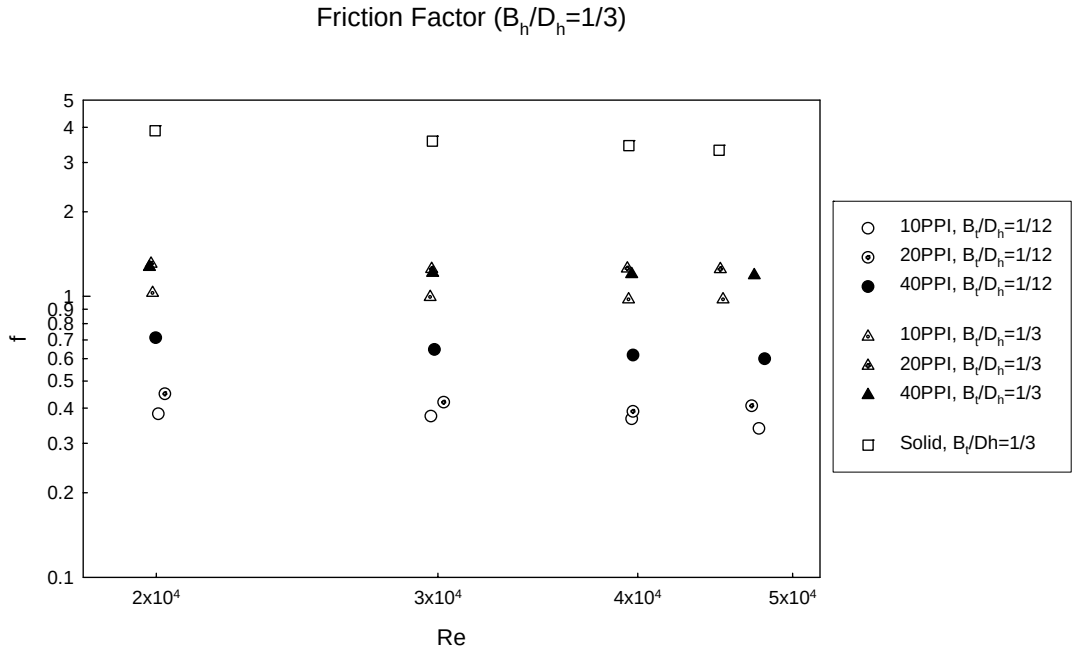

(b)

Fig. 4.4. Friction factor for B_h / D_h =1/3.

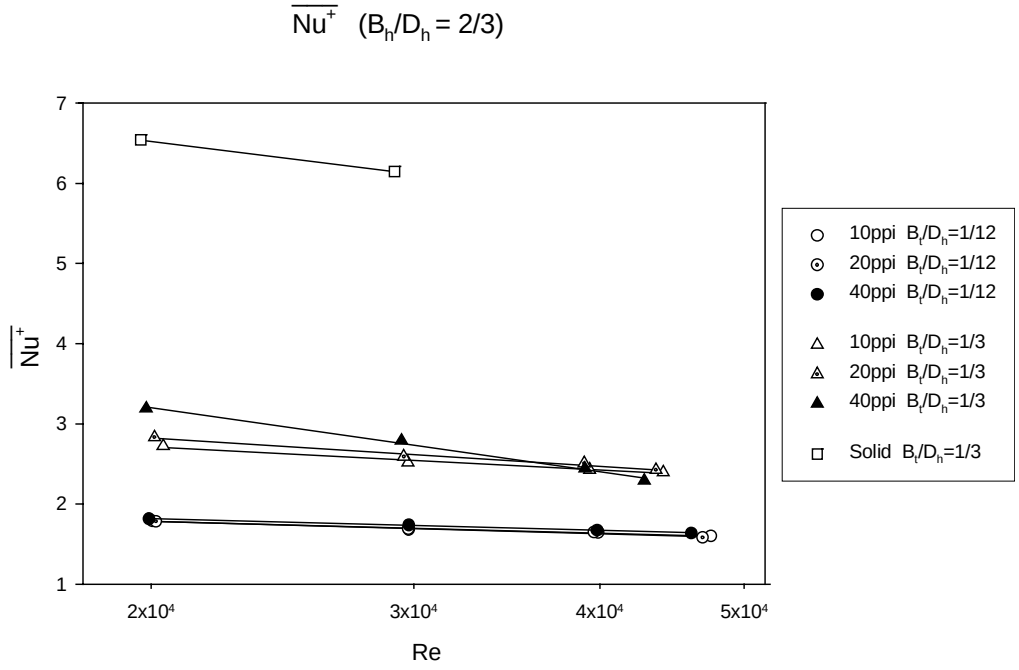

Fig. 4.5. Heat transfer enhancement ratio for B_h / D_h = 2/3.

Kuo and Tien's [9] results showed that the heat transfer enhancement is greater at higher flow rates and larger permeabilities (K). According to the material properties table, Table 3.1, provided by Kim et al. [12] and the present results show (Fig. 4.3 and 4.5) that the heat transfer enhancement is inversely proportional to the permeability for both high (present) and low flow rates [12]. This behavior is consistent with the fact that for a fixed baffle thickness the heat transfer enhancement ratio ($\overline{Nu^+}$) increases with an

increase in pore density. Accordingly, the baffles with the pore density of 40 PPI perform the best.

It is also interesting to see that the variations in $\overline{Nu^+}$ with pore density for thick baffles (B_t / D_h = 1/3) is greater compared to those for thinner baffles (B_t / D_h = 1/12). But from Fig. 4.5, it is evident that for taller (B_h / D_h = 2/3) and thicker (B_t / D_h = 1/3) baffles, as the flow rates increase the effect of pore density on $\overline{Nu^+}$ diminishes. This behavior can be explained using Darcy's equation [15]: $Q = K \times A \times \Delta P / L$. For a fixed flow rate, if the pressure drop across the baffle is large then the effect of permeability is small. On the other hand, when the flow rate is small and the pressure drop across the baffle is small, the effect of permeability is large.

The friction factor decreases slightly with an increase in Re (Fig. 4.4b). As expected the solid baffles have the highest friction factor. In general, the friction factor increases with an increase in pore density for a fixed Re. Accordingly, the thicker baffles (B_t / D_h = 1/3) with a pore density of 40 PPI have the highest friction factor. This behavior is attributed to the fact that the contact surface area between the fluid and the solid increases with an increase in pore density, thus increasing the amount of hydraulic resistance. The variation of the friction factor owing to the different pore densities is more distinct for thinner baffles (B_t / D_h = 1/12) as shown in Fig. 4.4b and 4.6b.

The dimensionless friction factors in Fig. 4.4a and 4.6a are shown for the comparison with the friction factor of a straight channel. It can be seen that the friction factor for the solid baffles are three to four times higher than porous baffles.

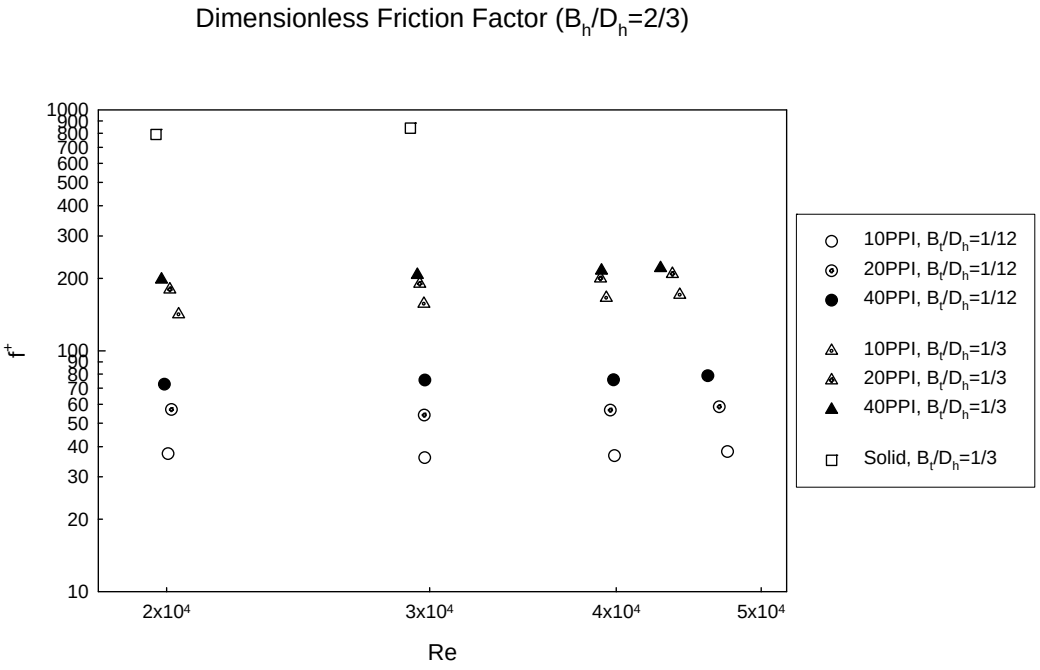

(a)

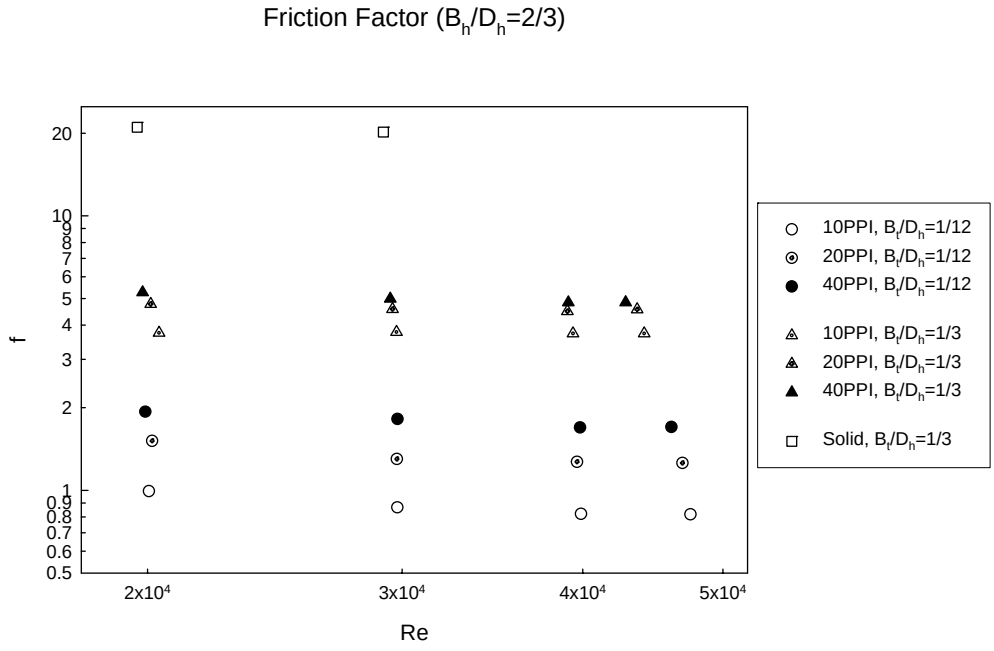

(b)

Fig. 4.6. Friction factor for B_h / D_h = 2/3.

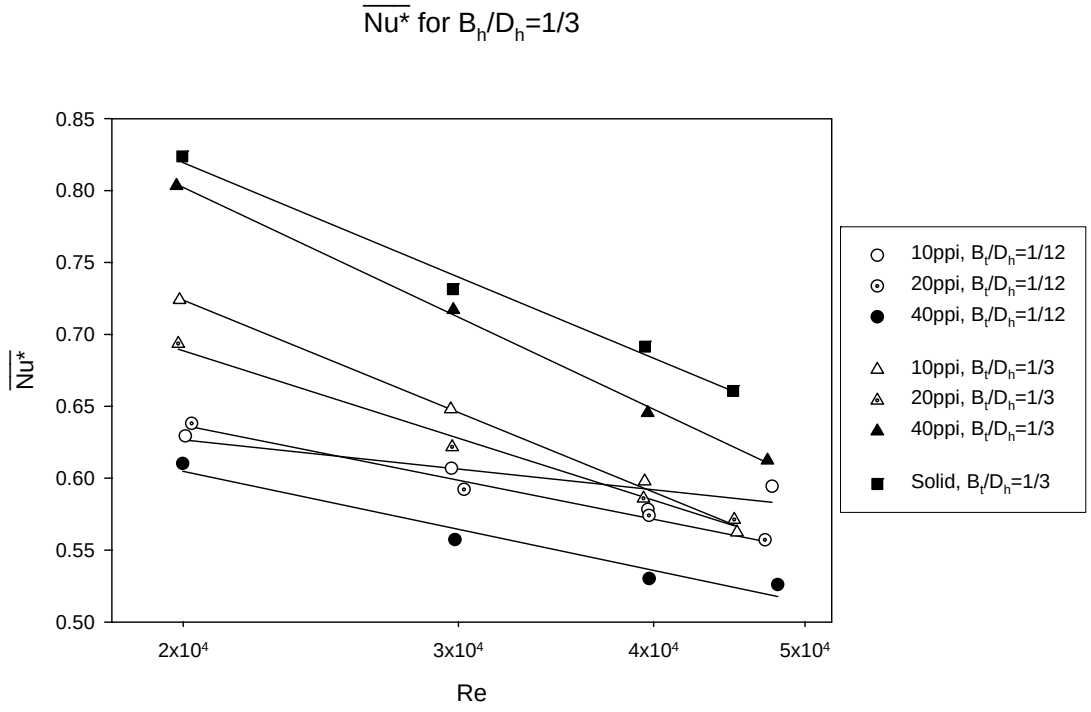

Fig. 4.7. Heat transfer performance for B_h / D_h = 1/3.

4.3 Heat Transfer Performance Ratio

The effectiveness of using porous baffles can also be studied by evaluating the heat transfer performance ratio. The heat transfer performance ratio is defined as the ratio of heat transfer enhancement to the unit increase in pumping power ($\overline{Nu^*} = \overline{Nu^+}/(f_{m,pdf} / f_s)^{1/3}$). In this ratio the friction factors are raised to the one-third power as the pumping power is proportional to the one-third power of the friction factor. For applications wherein the pumping power is of concern, the ratio $\overline{Nu^*}$ should be greater than unity (1).

It is evident from Fig. 4.7 and 4.8 that none of the data points satisfy the above condition. But there are several applications where pumping power is not scarce, as in the case of automobile or offshore drilling applications. In these cases space may be at a premium thus making the use of lightweight porous baffles very attractive.

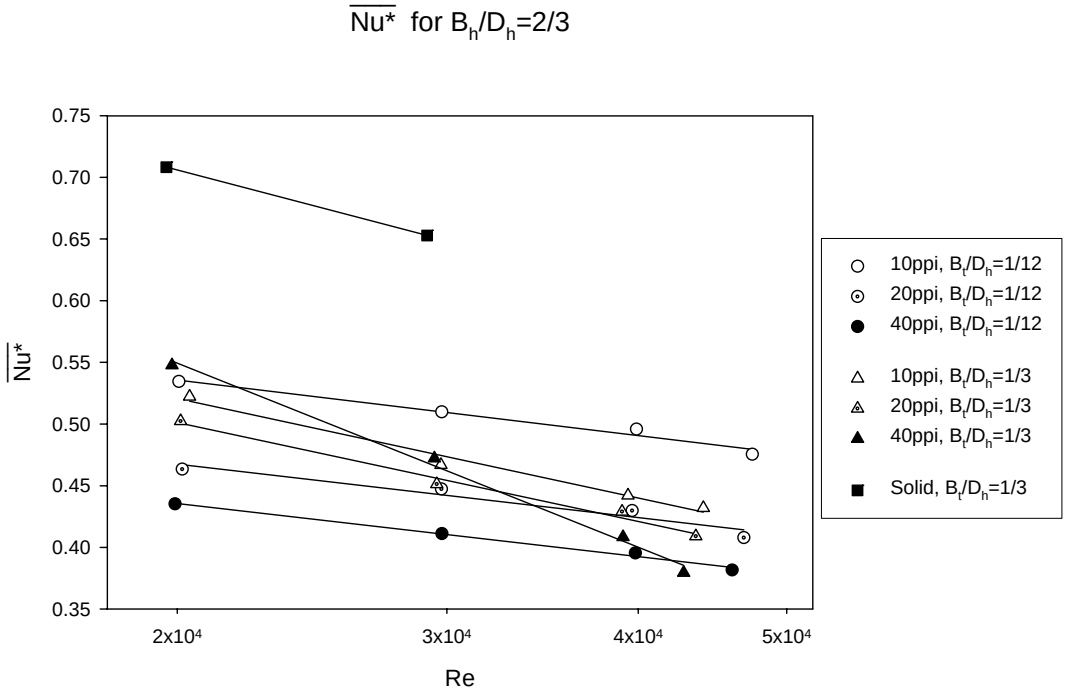

Fig. 4.8. Heat transfer performance for B_h / D_h = 2/3.

As expected the heat transfer performance ratio ($\overline{Nu^*}$) decreases with an increase in Re. This behavior is attributed to the fact that at higher Reynolds numbers turbulent effects prevail over enhancement due to porous baffles. As in the previous case (Fig. 4.3

and 4.5) the heat transfer performance ratios ($\overline{Nu^*}$) for the thicker baffle (B_t / D_h = 1/3) are higher. This is because of the fact that a greater heat transfer area is associated with thicker baffles.

Based on the experimental data, correlations for heat transfer enhancement ratio ($\overline{Nu^+}$) and heat transfer performance ratio ($\overline{Nu^*}$) were developed in terms of Reynolds number using the method of least squares. The correlations were of the form $\overline{Nu} = c_0 + c_1 \times \mathrm{Re} \times 10^{-6}$. Values for c_0 and c_1 for various cases are given in Table 4.1.

Table 4.1
Correlation coefficients for Nusselt numbers

Pore Density			10 PPI	20 PPI	40 PPI	10 PPI	20 PPI	40 PPI	Solid
Baffle Thickness (B_t / D_h)			1/12	1/12	1/12	1/3	1/3	1/3	1/3
B_h / D_h =1/3	$\overline{Nu^+}$	c_0	1.56	1.78	1.94	2.77	2.75	3.30	4.28
		c_1	-1.81	-6.95	-7.80	-17.13	-12.62	-20.93	-21.73
B_h / D_h =1/3	$\overline{Nu^*}$	c_0	0.65	0.70	0.66	0.84	0.93	0.93	0.93
		c_1	-1.48	-3.08	-2.92	-6.19	-3.24	-6.89	-6.17
B_h / D_h =2/3	$\overline{Nu^+}$	c_0	1.90	1.98	1.95	2.96	3.13	3.94	7.36
		c_1	-6.39	-8.78	-6.83	-13.17	-16.25	-38.55	-41.77
B_h / D_h =2/3	$\overline{Nu^*}$	c_0	0.57	0.51	0.47	0.59	0.57	0.69	0.82
		c_1	-2.06	-2.16	-1.99	-3.63	-3.73	-7.21	-5.87

4.4 Summary of Experimental Results

Experiments were conducted to study heat transfer enhancement in a rectangular channel using a porous baffle made of aluminum foam. Baffles were mounted on the bottom and top walls in a staggered fashion. Experiments were conducted in the Reynolds number range of 20,000-50,000. The maximum uncertainties associated with the average module Nusselt number and friction factor were 5.8% and 4.3%, respectively.

The experimental procedure was validated by comparing the data for the straight channel without baffles ($B_h / D_h = 0$) with those in literature [52, 53]. Experiments showed that the flow and heat transfer reach a periodically fully developed state downstream of the seventh module. For the range of independent parameters examined in this study the following conclusive statements can be made.

The heat transfer enhancement ratio ($\overline{Nu^+}$) decreases with an increase in the Reynolds number and increases with an increase in pore density. The heat transfer enhancement ratio reaches a maximum value of 320% for the range of parameters studied in this investigation. The heat transfer enhancement ratio was found to be higher for taller ($B_h / D_h = 2/3$) and thicker ($B_t / D_h = 1/3$) baffles.

The ratio of heat transfer enhancement per unit increase in pumping power was less than one. The friction factor slightly decreased with an increase in Reynolds number, and increased with baffle thickness and pore density. Based on the experimental data,

correlations for the heat transfer enhancement ratio ($\overline{Nu^{+}}$) and the heat transfer performance ratio ($\overline{Nu^{*}}$) were developed in terms of the Reynolds number.

CHAPTER V

NUMERICAL INVESTIGATION

5.1 Introduction

It seems that there was not significant progress in the numerical simulation of flow through channels partially filled with porous media due to the scarcity of the data and the lack of theoretical development. In the late 1980s, there were many studies reported for packed bed cases but not many for flow through channels with partially filled porous materials.

While there are fewer studies to resolve microscopic phenomenon, there was an effort to take advantage of volume averaged methods to obtain the macroscopic governing equations for porous media [16, 18, 20].

In this study, due to the lack of experimental data in the literature, effort has been made to the adaptability of currently available models. A commercial code, FLUENT, was used to investigate this problem, and GAMBIT was used to generate the grid.

5.2 Definition of Problem

5.2.1 Periodicity

As noted by Patankar et al. [54], the flow becomes periodically fully-developed in repetitive geometries. Since the geometry of a serpentine type channel (Fig. 3.2) is periodic the flow will become periodic far from the entrance region.

It is advised to use the periodic condition instead of inlet and outlet boundary condition with a large number of repetitive modules. By using the periodic condition, the computation time and cost can be saved for the case of self-repeating modules. A detailed description of periodic flow can be found in Partankar's paper and the FLUENT manual [54, 55].

5.2.2 Geometry

Using periodic characteristics of the given problem in Fig. 3.2, the periodic module shown in Fig. 3.3 can be used as the computational domain. Fig. 5.1 shows a schematic design for the computational domain that is used in this study. The computational domain is drawn from the simplified form of the experimental test section. The scale and labeling has been followed as noted in Fig. 3.3.

5.3 The Solver; FLUENT

5.3.1 Benefits and Limitations of Using a Commercial Code

Due to the complexity of the problem and limited amount of resources, a 3-dimensional investigation using numerical simulations was carried out by a commercial code. Among the available codes such as STAR-CD, FLUENT, TASCFLOW, and so forth, in the author's opinion, FLUENT showed more options to study these types of problems.

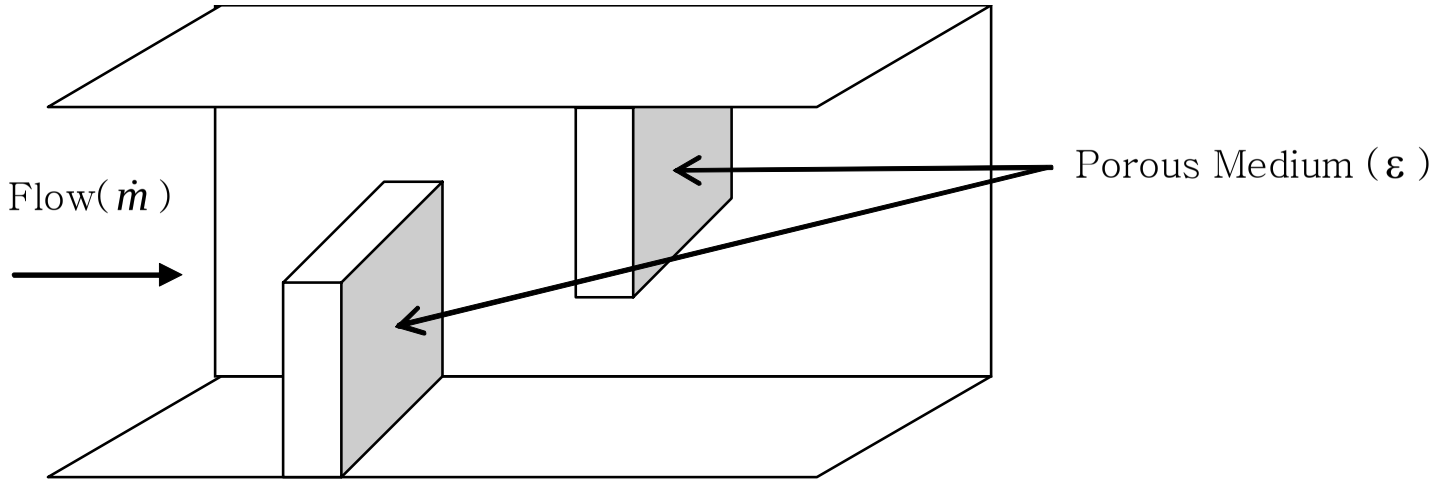

Fig. 5.1. Computational domain.

FLUENT allows the users to modify limited amounts of software using user definable files (UDF). FLUENT has stable and fast solver engines and supports user friendly input and output routines. Thus, it provides a shorter turnaround time. Meanwhile, the core part of the software is hidden from the user; thus, it is not easy to modify as required. Sometimes it is not possible to modify or obtain required data from the solver.

5.3.2 Momentum Equation

The governing equation (2.37) has to be used for full scale simulation of porous media, the limitation of FLUENT does not allow users to modify except for source terms and properties. Assuming a steady state condition and negligible gravity effects, the first term and the gravity force term in equation (2.37) will vanish. Thus, the comparable governing equation of FLUENT can be written as,

$$\underbrace{\rho_f \langle \boldsymbol{u} \rangle \cdot \nabla \langle \boldsymbol{u} \rangle}_{\text{convective inertia term}} = -\nabla \langle p \rangle^f + \underbrace{\mu \nabla^2 \langle \boldsymbol{u} \rangle}_{\text{Brinkman term}} + \underbrace{\frac{\mu}{K} \langle \boldsymbol{u} \rangle}_{\text{Darcy term}} + \underbrace{\frac{C \rho_f}{K^{1/2}} |\langle \boldsymbol{u} \rangle| \langle \boldsymbol{u} \rangle}_{\text{Forchheimer Term}} \qquad (5.1)$$

Considering the fact that the porosity used in the current study is very high ($\varepsilon = 0.92$), the effects of porosity toward the convective term and the Brinkman term in equation (2.37) are neglected in this study.

5.3.3 Turbulence Model

Many turbulence models are available through FLUENT [55]. Instead of using the standard $k-\varepsilon$ model by Launder and Spalding [56], the RNG $k-\varepsilon$ model was

selected. It is clear that the LES model or low-Reynolds model such as Reynolds Stress Model (RSM) would be more preferable to resolve the near wall phenomenon. However, in the mean time, currently available governing equations to describe the flow through the porous media have been developed under the laminar to transition range and the assumption that the large size eddies, which are larger than the size of pore scale would be suppressed due to the presence of the solid matrix.

Considering all of aspects of the limitations of the currently available theory, the RNG $k-\varepsilon$ model was selected. RNG $k-\varepsilon$ has the following benefits compared to the standard $k-\varepsilon$ model [55]: Differential viscosity model; Swirl modification is available; Viscous heating; and Inclusion of buoyancy effects on the turbulence dissipation term.

Due to the rapid change of velocity near the porous zone, this model is a suitable choice for the current study. The coefficients for the RNG $k-\varepsilon$ are $C_{\mu}=0.0845$, $C_{1,\varepsilon}=1.42, C_{2,\varepsilon}=1.68$. Detailed information regarding RNG $k-\varepsilon$ can be found in the literature [55].

The selection of the wall treatment methods is as important as the selection of turbulence model. The non-equilibrium turbulence model has been selected for this study. For the same reason as the selection of turbulence model, the enhanced wall function model is preferable but in a pilot testing with this model, it was found that the code often diverges and consumed too much time to converge. Due to this difficulty, the non-equilibrium model [55, 57] was used in this study. The non-equilibrium model [55,

57] is sensitized to the pressure gradient in the near wall region. For such reason, it is expected that it can handle the abrupt change of pressure near the porous wall zones.

5.3.4 Energy Equation

The comparable energy equation used in FLUENT with this study can be written as,

$$\rho_f C_{pf} \langle \boldsymbol{u} \rangle \cdot \nabla \langle T \rangle^f = \nabla \cdot \left(K_{eff} \nabla \langle T \rangle^f \right) + S_f \qquad (5.2)$$

where,

$$K_{eff} = \varepsilon (K_f + K_{t,f}) + (1-\varepsilon) K_s \qquad (5.3)$$

$K_{t,f}$ is theoretical conductivity increased by turbulence.

$$K_{t,f} = \frac{\mu_t C_p}{Pr_t} \qquad (5.4)$$

where, Pr_t is the turbulent Prandtl number. Assuming that there is no heat generation, S_f vanishes. Currently K_{eff} is not directly accessible by the users to modify.

5.4 Programming Using User Defined Functions (UDFs)

5.4.1 User Defined Functions

A system of UDFs is a set of macro functions which allows the users to access the limited sets of internal data. UDF can be coded using C language and is able to be compiled or interpreted with an internal or external compiler.

The function definition format of UDF is determined by a set of define macros which are classified and named by the nature of the internal calling procedures, data type, and the locations of calling. To interrupt the procedures of the solution process, the following macro sets were used,

DEFINE_INIT (called before main loop is activated)
DEFINE_ADJUST (called one time while main loop is executed)
DEFINE_EXECUTE_AT_END (called after solution is converged)
DEFINE_ON_DEMAND (can be called while not calculating anytime)

To set the specific values of variables (i.e. Velocity, Temperature, Porosity, etc.) the following model specific macros can be used,

DEFINE_PROFILE (used for setting profile of variables)
DEFINE_PROPERTY(used for setting property variables)
DEFINE_DIFFUSIVITY (used for setting user definable diffusivity)
DEFINE_SOURCE (used for setting source terms)
DEFINE_HEAT_FLUX (used for setting heat flux)

Accessing internal data is limited to the most general types such as velocity, temperature, and porosity, but not to all of the variables. Users can access the cell data for input and output purposes, but the internal face data cannot be changed by users, except for the outer fac,e such as wall boundaries.

5.4.2 Flowchart for Two-Phase Solution

Fig. 5.2 is the flowchart for the calculation solution procedures for the two-equation model. Round rectangular boxes denote the user modifiable routines, and the rectangular boxes denote code supplied routines.

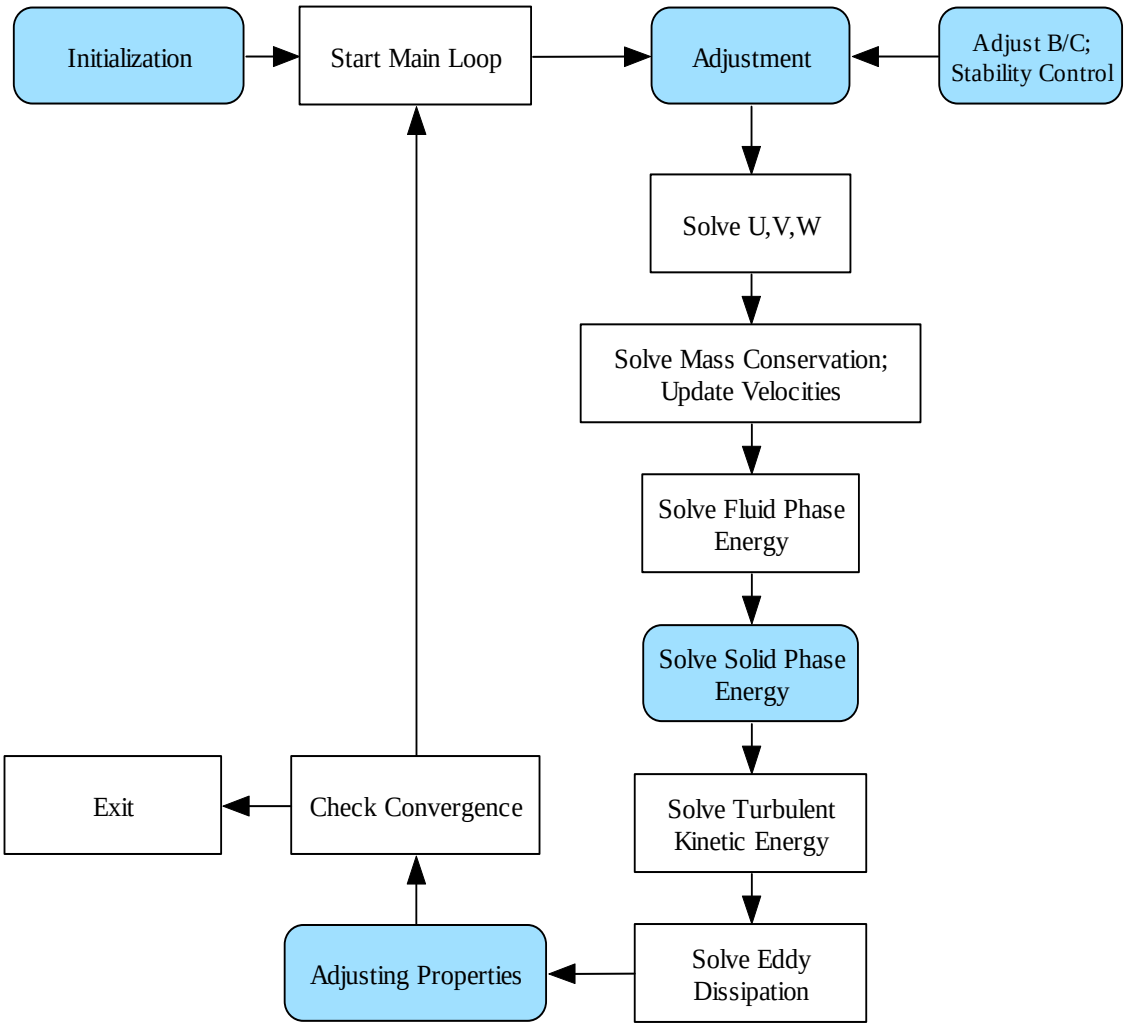

Fig. 5.2. Flowchart for the two-equation model calculation.

5.5 Convergence Criteria and Numerical Scheme

For convergence criteria, the relative errors of residual of each variable are set to be less than 10^{-6}. And the first order upwind method was used to represent the solution for the one-dimensional convection-diffusion problem. Relaxation factor and convergence criteria are shown in the Table 5.1.

Table 5.1
Convergence criteria and numerical scheme

Variables	Convergence Criteria	Relaxation Factor
u	$R^u \le 1.0\times10^{-6}$	0.7
v	$R^v \le 1.0\times10^{-6}$	0.7
w	$R^w \le 1.0\times10^{-6}$	0.7
p	$R^p \le 1.0\times10^{-6}$	0.3
T_f	$R^{T_f} \le 1.0\times10^{-6}$	0.1~0.3
k	$R^k \le 1.0\times10^{-6}$	0.8
ε	$R^\varepsilon \le 1.0\times10^{-6}$	0.8
T_s	$R^{T_s} \le 1.0\times10^{-6}$	0.05~0.1

where, $R^\phi = \dfrac{\sum_{cells\ P}\left|\sum_{nb} a_{nb}\phi_{nb} + b - a_p\phi_p\right|}{\sum_{cells\ P}\left|a_P\phi_P\right|}$ and ϕ is arbitrary variable.

5.6 Mesh Generation

5.6.1 Dimensionless Distance

The wall function approach in the turbulence model is based on log-law or universal law of the flow. Thus, the evaluation of the wall function needs to be within appropriate range. The standard $k-\varepsilon$ model [56] is known to be valid within the first grid node located from the wall such that,

$$y^* > 30 \sim 60 \tag{5.5}$$

where y* is the non-dimensional distance defined as,

$$y^* = \frac{\rho C_\mu^{1/4} k_i^{1/2} y_i}{\mu} \tag{5.6}$$

where k_i is turbulence kinetic energy at point i, and y_i is the distance from point i to the wall.

Another form of the dimensionless distance is,

$$y^+ = \frac{\rho u_\tau y_i}{\mu} \tag{5.7}$$

where $u_\tau = \sqrt{\tau_w / \rho_w}$ is frictional velocity.

These two quantities are known to be equal in equilibrium turbulent boundary layers.

The RNG $k-\varepsilon$ model is known to be valid for $y^* > 11.225$ and FLUENT is assuming that the velocity profile within the viscous sub-layer follows the log-law (equation (5.8)).

$$u^* = \frac{u_i C_\mu^{1/4} k_i^{1/2}}{\tau_w / \rho} = \frac{1}{k} \ln(Ey^*) \qquad (5.8)$$

where, u^* is the non-dimensional velocity, k is the Von Karman constant (0.42), and E is an experimental constant (9.793).

With a series of testing, y^+ was maintained within the valid range for each case. Using the boundary layer function of GAMBIT, the boundary layer height from the wall can be controlled.

5.6.2 Sample Grids

Using the journal system of GAMBIT, an automatic grid generating program is written. The input parameters for grid generation are,

$x2 = thickness of porous block

$y1 = height of porous block

$z1 = width of porous block

$blayer = length of boundary layer (y1+)

$ph = block selection for porous zone (1 or 2)

This program will generate the volumes of zones and combine multiple zones when necessary to make porous zones. It will also set the periodic and its shadow condition for the inlet and outlet regions. Users can change the porous zone by selecting different

volumes in the GAMBIT menu. Boundary layer length had to be determined heuristically after many trials. A sample mesh generated with this program is shown in Fig. 5.3.

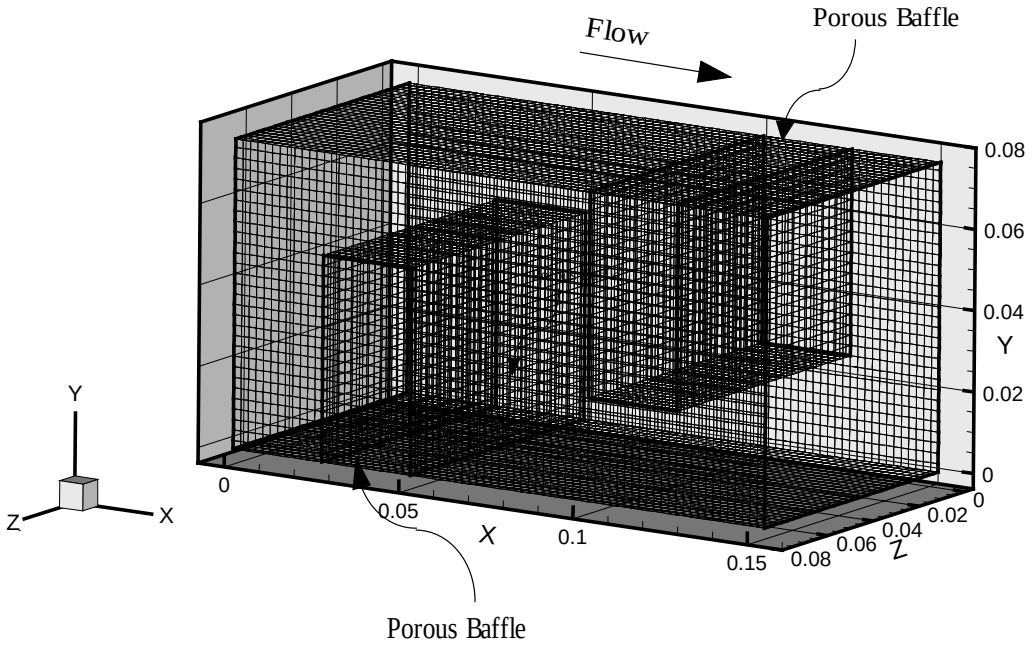

Fig. 5.3. Generated mesh

5.7 Models and Implementation

5.7.1 Heat Transfer (Conventional Model)

The theoretically developed model (equation (2.48)) is generally used when the appropriate effective conductivity of porous media is not obtained but this model does not account for the resistance between the phases (solid and fluid) or heat transfer enhancement by tortuosity of the materials. This model is verified with the experimental data for the validity of code implementation before testing other models. This model also has to be included in the category of the one-equation mode, but it is separated in this study as it is the fundamental model to be compared to others.

5.7.2 Heat Transfer (One-Equation Model)

As noted in equations (2.47)-(2.50), the effective conductivity of the moderate flow range can be modeled with the dispersion conductivity (K_d) and effective conductivity of the fluid (K_{eff}). However, these studies have been conducted in the limited parametric conditions. Most of the research and the correlation have been developed under the assumption of,

1. Lower range of flow speed ($Re = 10 \sim 10^3$)
2. Channel is fully saturated and filled with solid matrix
3. Particle based modeling of the heat transfer correlation data (thus, the porosity ranged from 0.3~0.4 for one type of particle)

Due to the shortage of information related to the characteristics of the foam material, an attempt was made with the modification of the currently available model based on the correlations using spherical beads. And its feasibility was studied.

It is interesting to note that K_{eff} in equation (2.48) is a theoretical value which is not considered with the interfacial resistance. Poulikakos [36] reported that with his experiments, the effective conductivity of air to aluminum is about 6.0 with aluminum foam of porosity 0.92.

Hsu and Cheng [26] used Van Driest type of wall function for the estimation of thermal dispersion conductivity (K_d).

$$K_d = K_f D_t Pe_d l\left(u / u_m\right) \qquad (5.9)$$

where, $Pe_d = u_m d_p / \alpha_f$, the Peclet number is based on the mean seepage velocity u_m, the particle diameter d_p, and fluid thermal diffusivity α_f. D_t is a heuristic constant and l is dimensionless dispersive distance normalized with respect to d_p.

The dispersive length is modeled by a wall function of the Van Driest type:

$$l = 1 - \exp(-y / \omega d_p) \qquad (5.10)$$

where, ω is an empirical constant and y is a distant from the wall.

Using the relationship of equation (5.11) , and substituting equation (5.11) into (5.9) , we get equation (5.12) ,

$$Pe_d = u_m d_p / \alpha_f$$
$$\alpha_f = K_f / C_p \rho_f \qquad (5.11)$$

$$K_d = D_t \rho_f C_p d_p |u| l \qquad (5.12)$$

where,

$$|u| = \sqrt{u^2 + v^2 + w^2} \qquad (5.13)$$

By comparing the numerical results using this model with experimental data, the heuristic constant ω and D_t were determined to be 1.5 and 0.375 respectively.

In this study, the porous material is not made of particles so the direct usage of equation (5.12) is not possible. One way of obtaining the effective particle diameter is using equation (2.4) and the properties of current porous medium in Table 3.1.

Equation (2.4) can be rearranged as,

$$d_{p,eff} = \sqrt{K \cdot 180 \frac{(1-\varepsilon)^2}{\varepsilon^3}} \qquad (5.14)$$

From equation (5.14), the relationship between d_p and K agreed with equation (2.51). However, due to the structural discrepancy between the two materials, there can be a difference in the effective diameter. Considering the fact that the spherical type beads normally have has a porosity of 0.37 and current material has 0.92, the term $\sqrt{180 \frac{(1-\varepsilon)^2}{\varepsilon^3}}$ has the values from 1.2 to 38 in that range, it is estimated that there could be a difference in the order of magnitude of one or two (Fig. 5.4).

The calculated value of the effective diameter is presented in Table 5.2, along with the square root of permeability. In this study, the square root of permeability is used instead of effective diameter calculated using equation (2.4).

Table 5.2
Effective diameter of aluminum foam

	10PPI	20PPI	40PPI
Permeability, K (m^2)	1.04E-07	7.60E-08	5.10E-08
Effective diameter, $d_{p,eff}$ (m)	3.922484E-04	3.353137E-04	2.746816E-04
$\sqrt{K}$, (m)	3.224903E-04	2.756810E-04	2.258318E-04

Thus, the modified equation for the thermal dispersion coefficients is,

$$K_d = D_t \rho_f C_p \sqrt{K} u l \qquad (5.15)$$

The experimental data on aluminum foam considered in this study is very limited [6]. Thus, the heuristic coefficients most be determined by comparing computational results with experimental data.

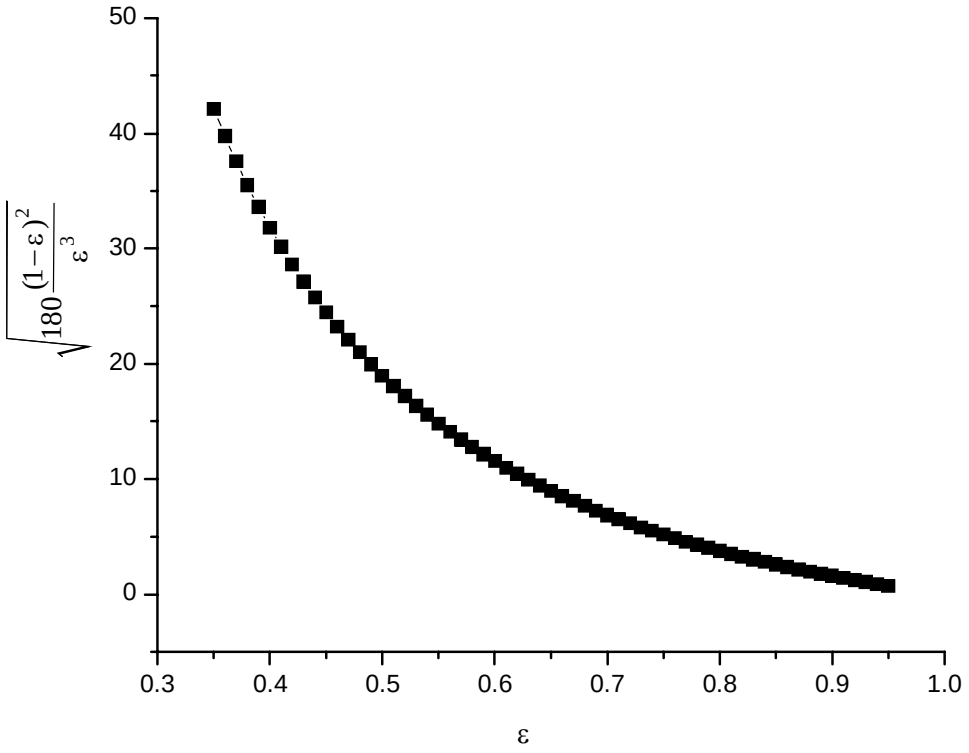

Fig. 5.4. The variation of $\sqrt{180(1-\varepsilon)^2/\varepsilon^3}$ with porosity.

5.7.3 Heat Transfer (Two-Equation Model)

To utilize Hwang and Chao's [11] model, the void diameter (d_v) has to be evaluated, as well as the interfacial area between the porous medium and the fluid (A_{int}). The comparison of the specific area by using the Carman-Kozeny equation (2.4) and the non-dimensional distance based on the permeability in Hwang and Chao's [11] model and Wakao's [46] model is presented in Table 5.3.

It can be seen from Table 5.3 that Chao's model is far from the actual value, and Wakao's model also significantly deviates from the experimental data. From Table 5.3, it can be concluded that a modified permeability based model from Chao's correlation showed the closest value for foam material. Since specific heat is related directly to the heat transfer mechanism inside the solid matrix, this issue has to be further investigated to be applied to arbitrary solid matrices.

However, specific areas were obtained by Kim's [12] experiments; thus, the actual specific areas will be used instead of the proposed ones. Void diameter d_v can be evaluated using equation (5.16),

$$d_v = \frac{4\varepsilon}{A_{\text{int}}} \qquad (5.16)$$

The local interfacial heat transfer coefficient is modified by substituting the thermal conductivity of the fluid for the effective thermal conductivity. Since there is no information available regarding this approach, the other parameters have to be

determined using a parametric study to correlate the overall effects of the experimental data taken in this study.

Table 5.3
Comparison of specific area (m^2)

	10PPI	20PPI	40PPI
Experimental Data	7.900000E+02	1.720000E+03	2.740000E+03
Hwang and Chao's model [11] $20.346(1-\varepsilon)\varepsilon^2 / d_{p,eff}$	1.321322E+04	1.545676E+04	1.886862E+04
Wakao's model [46] $6(1-\varepsilon)/d_{p,eff}$	4.603680E+03	5.385363E+03	6.574106E+03
Hwang and Chao's model [11] $20.346(1-\varepsilon)\varepsilon^2 / \sqrt{K}$	4.271968E+03	4.997328E+03	6.100418E+03
Wakao's model [46] $6(1-\varepsilon)/\sqrt{K}$	1.488417E+03	1.741143E+03	2.125476E+03
Percent Relative Error for Models			
Hwang and Chao's model [11] $20.346(1-\varepsilon)\varepsilon^2 / d_{p,eff}$	1.572559E+03	7.986488E+02	5.886358E+02
Wakao's model [46] $6(1-\varepsilon)/d_{p,eff}$	4.827443E+02	2.131025E+02	1.399309E+02
Hwang and Chao's model [11] $20.346(1-\varepsilon)\varepsilon^2 / \sqrt{K}$	4.407555E+02	1.905423E+02	1.226430E+02
Wakao's model [46] $6(1-\varepsilon)/\sqrt{K}$	8.840719E+01	1.229244E+00	-2.242789E+01

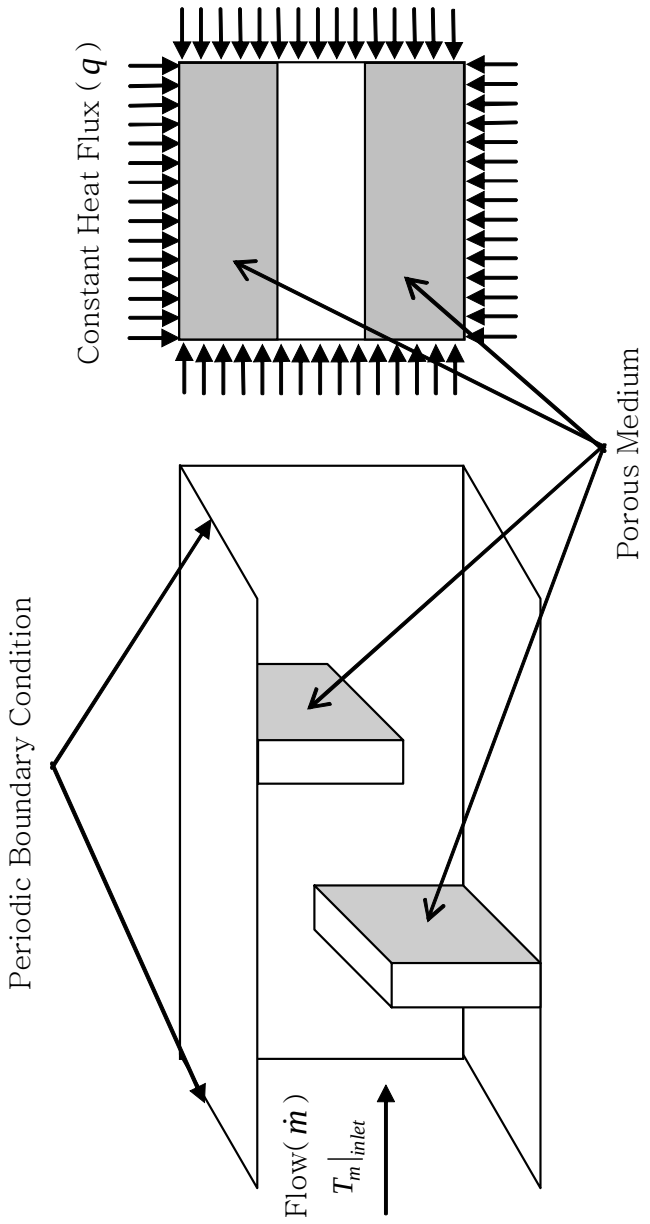

Fig. 5.5. Boundary conditions for one-equation model.

5.8 Boundary Conditions

5.8.1 Boundary Conditions for the One-Equation Model

The boundary condition applied for the one-equation model is shown in Fig. 5.5. Four walls are subjected to constant heat flux and due to the periodic condition the mass flux has been prescribed instead of velocity.

5.8.2 Boundary Conditions for the Two-Equation Model

When the heat transfer between two phases is considered due to the local non-thermal equilibrium condition a new problem arises. The amount of heat flux (q) through the fluid side and solid matrix near the wall has to be determined [58] (Fig. 5.6).

Amiri [59] assumed equal amount of heat flux for the solid and fluid phases for his numerical experiments as,

$$q = -K_s \left.\frac{\partial \langle T \rangle^s}{\partial y}\right|_{wall} = -K_f \left.\frac{\partial \langle T \rangle^f}{\partial y}\right|_{wall} \qquad (5.17)$$

but Kim [60] has shown that a different amount of heat transfer would occur through each phase as,

$$q = -K_{s,eff} \left.\frac{\partial \langle T \rangle^s}{\partial y}\right|_{wall} - K_{f,eff} \left.\frac{\partial \langle T \rangle^f}{\partial y}\right|_{wall} \qquad (5.18)$$

$$\langle T \rangle^s \Big|_{wall} = \langle T \rangle^f \Big|_{wall}$$

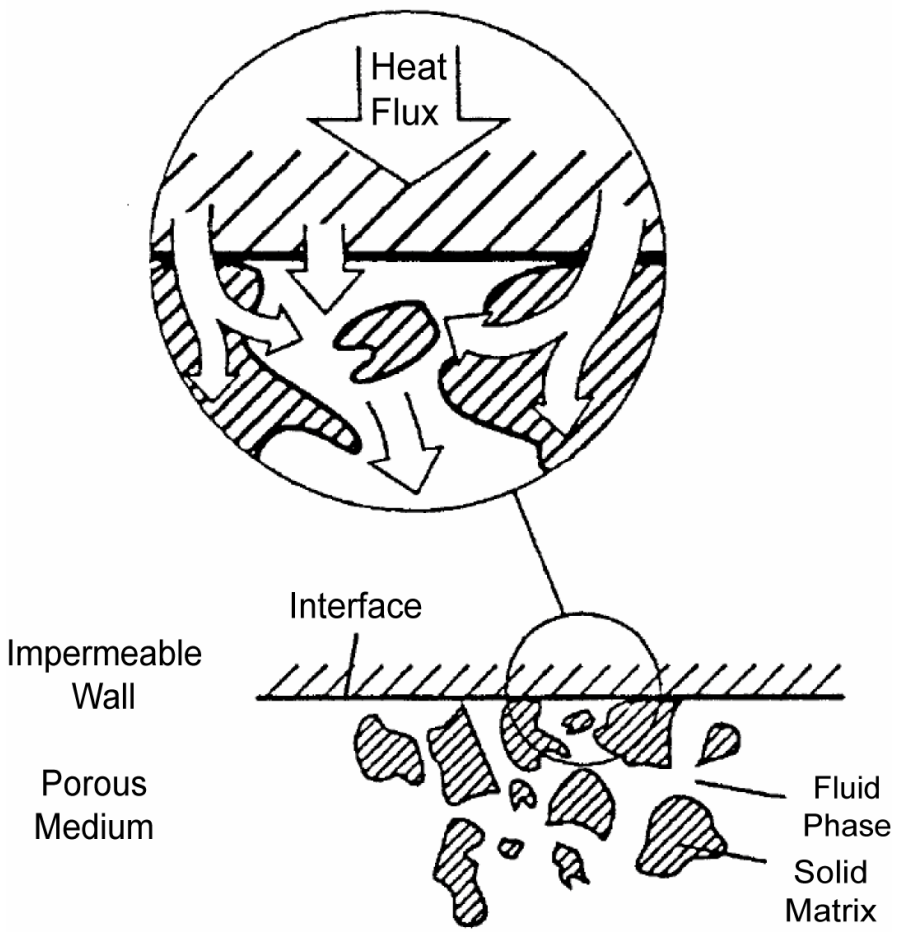

Fig. 5.6. Heat transfer at the interface between the porous medium and the impermeable wall [58].

Considering equation (2.48) the effective thermal conductivity of fluid phase can be written as,

$$K_f^* = \varepsilon K_f \tag{5.19}$$

and the effective thermal conductivity of the solid phase can be written as,

$$K_s^* = (1-\varepsilon) K_s \tag{5.20}$$

Unlike spherical beads, the porosity of metal foam is very high; thus, the contact area must be considered,

$$q = -K_f^* a_f'' \left.\frac{d\langle T\rangle^f}{dy}\right|_{wall} - K_s^* a_s'' \left.\frac{d\langle T\rangle^s}{dy}\right|_{wall} \tag{5.21}$$

where $a_s^{''}$ is ratio of area occupied by the solid contact and total area, $a_f^{''}$ is ratio of area occupied by the fluid contact and the total area. If the solid matrix is not attached to the impermeable wall, then the right hand side of the equation (5.21) will vanish; thus, the equation (5.21) is more reliable.

The contact has been made with thermal epoxy in the experiment; thus $a_f^{''}$ is assumed to be proportional to the porosity of the medium. Substituting equation (5.19) and (5.20) into equation (5.21) gives,

$$q = -\varepsilon^2 K_f \left.\frac{d\langle T\rangle^f}{dy}\right|_{wall} - (1-\varepsilon)^2 K_s \left.\frac{d\langle T\rangle^s}{dy}\right|_{wall} \tag{5.22}$$

For air as fluid, aluminum as solid matrix, and assuming the gradient of temperature near the wall is not very different for each phase [60], the ratio of heat flux between the two phases is,

$$\frac{(1-\varepsilon)^2 K_s}{\varepsilon^2 K_f} \approx 64 \qquad (5.23)$$

It can be calculated that $q_s / q \approx 0.985$ and $q_f / q \approx 0.015$. Thus, a major part of the heat transfer is occurring through the solid phase. At the bottom of the porous zone , the solid and fluid temperature are assumed to be the same as,

$$\langle T \rangle^s = \langle T \rangle^f \qquad (5.24)$$

Considering the first order discretized form of the heat flux near the wall, for the solid phase,

$$\langle T \rangle^s \Big|_w = \langle T \rangle^s \Big|_1 + q_s ds / K_s^* \qquad (5.25)$$

and, for the fluid phase,

$$\langle T \rangle^f \Big|_w = \langle T \rangle^f \Big|_1 + q_f ds / K_f^* \qquad (5.26)$$

Since the temperature is the same at the wall,

$$\left\langle T \right\rangle^s \Big|_1 + q_s ds / K_s^* = \left\langle T \right\rangle^f \Big|_1 + q_f ds / K_f^* \qquad (5.27)$$

For the fluid-porous interface boundary conditions, we can use the volume averaged method for both sides for the heat flux,

$$-K_f \left. \frac{\partial \left\langle T \right\rangle^f}{\partial \boldsymbol{n}} \right|_{f \to p} = -K_f^* \left. \frac{\partial \left\langle T \right\rangle^f}{\partial \boldsymbol{n}} \right|_{p \to f} - K_s^* \left. \frac{\partial \left\langle T \right\rangle^s}{\partial \boldsymbol{n}} \right|_{p \to f} \qquad (5.28)$$

where $f \to p$ denotes heat flux from the fluid to the porous side interface, $p \to f$ denotes heat flux from the porous side to the fluid side interface, and $\boldsymbol{n}$ is a unit normal vector to the interface. Considering continuity of the gradient of the temperature of the fluid phase and the effective thermal conductivity of the fluid,

$$-\varepsilon K_f \left. \frac{\partial \left\langle T \right\rangle^f}{\partial \boldsymbol{n}} \right|_{f \leftrightarrow p} = -\varepsilon K_s \left. \frac{\partial \left\langle T \right\rangle^s}{\partial \boldsymbol{n}} \right|_{p \leftrightarrow f} \qquad (5.29)$$

Thus, the simplified form of the boundary condition at the interface is,

$$\frac{K_f}{K_s} \left. \frac{\partial \left\langle T \right\rangle^f}{\partial \boldsymbol{n}} \right|_{f \leftrightarrow p} = \left. \frac{\partial \left\langle T \right\rangle^s}{\partial \boldsymbol{n}} \right|_{p \leftrightarrow f} \qquad (5.30)$$

Considering $K_s / K_f \approx 10,000$, the gradient of the solid matrix near the interface is very small but not to be neglected for stability. The accurate resolution of this

boundary condition seems to be very important but due to the limitation of user modification, equation (5.30) is descritised with first order approximation.

Fig. 5.7 shows the boundary conditions used for the two-equation model evaluation. Wall heat flux is applied to the wall of the test section except for the wall interface which is attached to the bottom plate of the porous block.

5.9 Nusselt Number Evaluation

5.9.1 Nusselt Number Evaluation for the One-Equation Model

The evaluation of the Nusslet number for the one-equation model is fairly straight forward. The Local Nusselt number (Nu) is defined as,

$$Nu = \frac{qD_h}{K_f (T_w - T_b)} \tag{5.31}$$

and the average module Nusselt number is defined as,

$$\overline{Nu_m} = \frac{1}{A}\int_A \frac{qD_h}{K_f (T_w - T_b)}\, dA \tag{5.32}$$

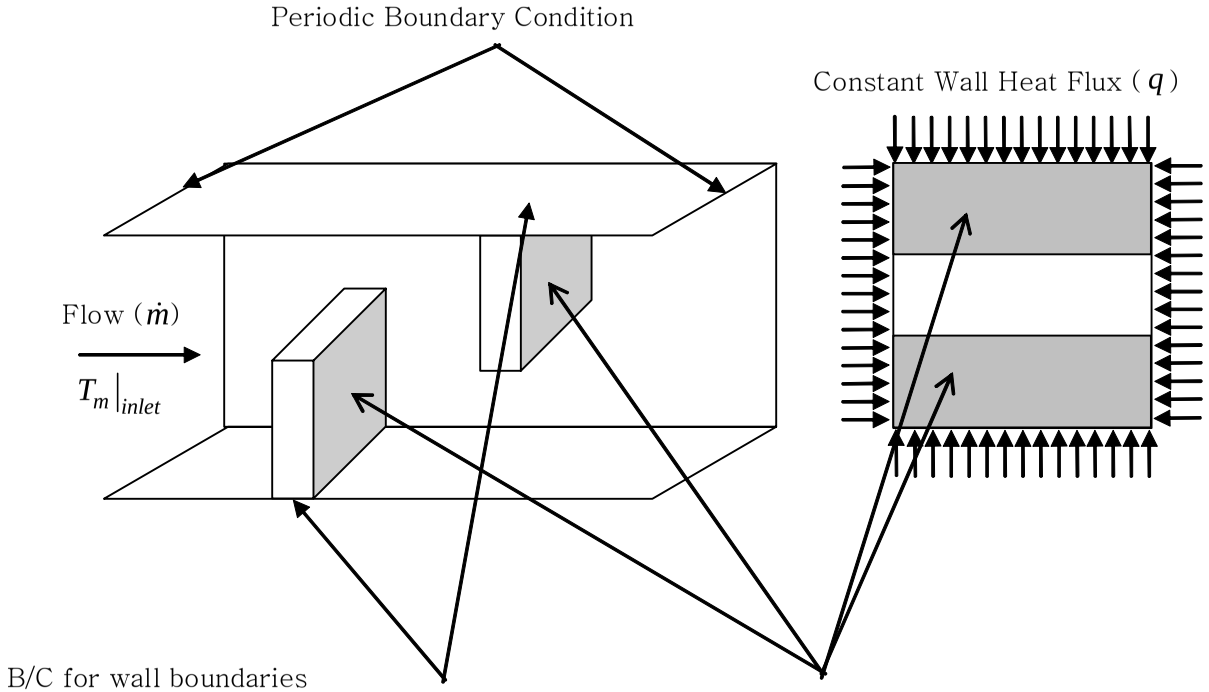

Fig. 5.7. Boundary conditions for the two-equation model.

Thus, the average module Nusselt number can be evaluated as in equation (5.33),

$$\overline{Nu_m} = \frac{1}{A}\int_A \frac{qD_h}{K_f(T_w - T_b)}\,dA = \frac{qD_h}{K_f(\overline{T_w} - T_b)} \qquad (5.33)$$

where A is total area of the module, subscript fluid denotes the surface area of the fluid only zone and porous denotes the wall zone area of the porous media.

5.9.2 Nusselt Number Evaluation for the Two-Equation Model

Since the amount of heat applied to the porous wall region is applied separately to fluid and solid region the Nusselt number for this region can be evaluated by superposition of the two representative Nusselt numbers for each phase (equation (5.34)).

$$\overline{Nu}\Big|_{porous} = \overline{Nu}\Big|_{fluid} + \overline{Nu}\Big|_{solid} = \frac{q_f D_h}{K_f(T_{w,f} - T_b)} + \frac{q_s D_h}{K_f(T_{w,s} - T_b)} \qquad (5.34)$$

Considering the boundary condition for temperature at the porous zone is $T_{w,f} = T_{w,s}$, the equation can simply be combined into,

$$\overline{Nu}\Big|_{porous} = \frac{qD_h}{K_f(T_{w,s} - T_b)} \qquad (5.35)$$

Now using equation (5.32), the module Nusselt number can also be calculated,

$$\overline{Nu_m} = \frac{1}{A}\int_A Nu\ dA = \frac{1}{A}\left(\overline{Nu}\Big|_f\ A_f + \overline{Nu}\Big|_p\ A_p\right)$$
$$= \frac{1}{A}\left(\frac{q_f D_h}{K_f(\overline{T_{w,f}} - T_b)}A_f + \frac{q_s D_h}{K_f(\overline{T_{w,s}} - T_b)}A_p\right) \qquad (5.36)$$

CHAPTER VI

RESULTS AND DISCUSSION

6.1 Grid Independence Test

It is very time consuming to test each case for grid independency. Upon a series of randomly selected test cases, it is assumed that the rest of the cases have the same order of error level with representative cases. The grid independence test for the case of $B_t / D_h = 1/12$ and $B_h / D_h = 1/3$ is shown in Fig. 6.1. A non-uniform grid is used and the grid size has been increased from 44x15x25 to 72x45x45.

The data is shown in Table 6.1. The absolute error for Nu^+ is in Fig. 6.1a and shows maximum error less than 1.5 for the entire range. The percent relative error of Nu^+ is in Fig. 6.1b and shows maximum relative error less than 2%. Thus, the grid size is chosen to be 72x30x30 in this study.

Table 6.1
Maximum percent relative error for Nu^+

Re	72x15x15	72x30x30	72x45x45
10000	0.87%	0.04%	0.43%
20000	1.12%	0.79%	0.17%
30000	1.25%	1.21%	0.56%
40000	1.25%	1.39%	0.33%
50000	1.42%	1.44%	0.49%

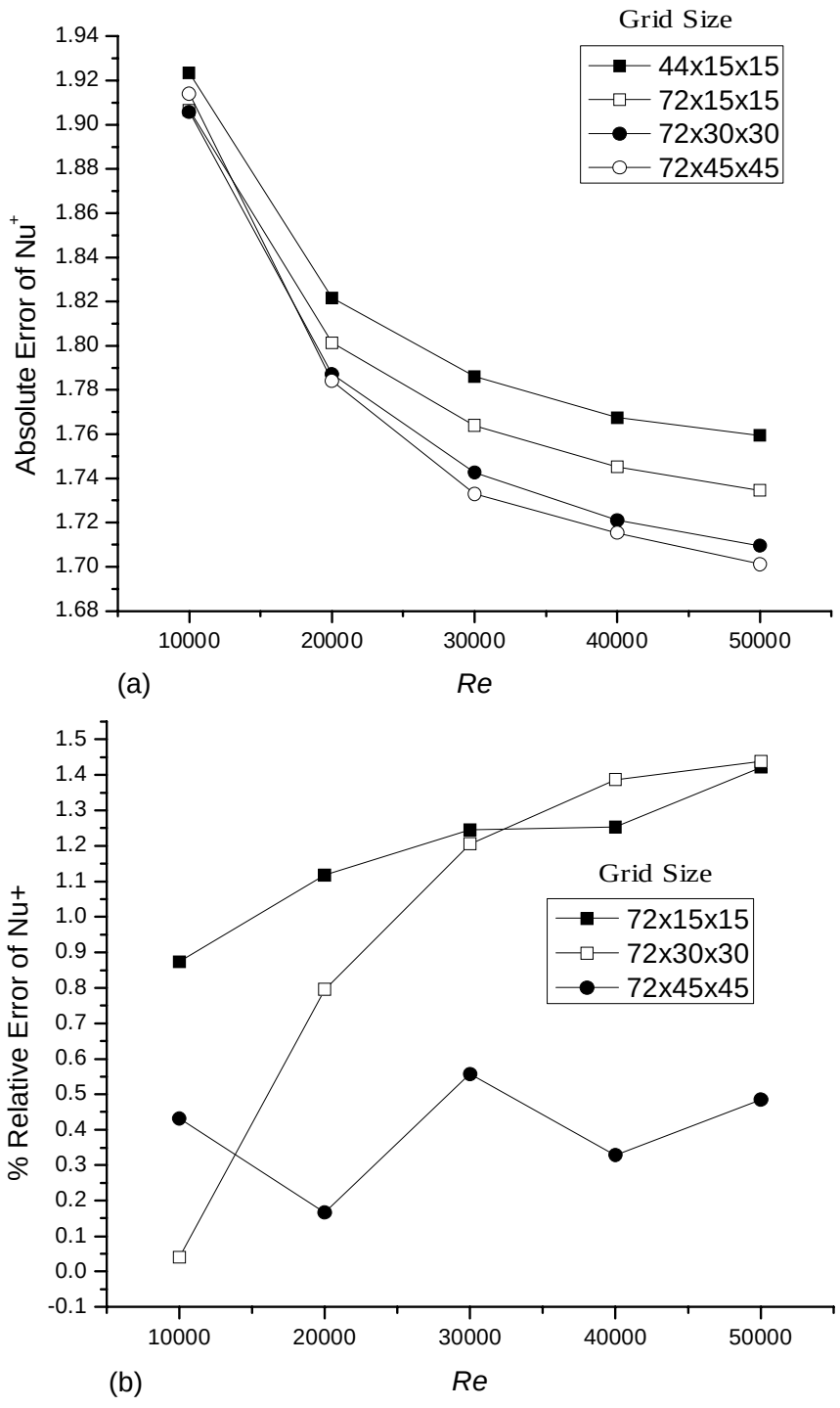

Fig. 6.1. Grid independence test for $B_t / D_h = 1/12$ and $B_h / D_h = 1/3$.

6.2 Results of the Conventional Model

6.2.1 Forchheimer Constant Dependency

The inertial coefficient in equation (2.18) is based on the assumption of sluggish flow and the beads, spheres, or particle based model for the solid matrix. The inertial coefficient can also be estimated using equation (2.16), but it is known that the correlation breaks down for the following conditions [61],

1. very high porosity,
2. particles very far from spherical shape,
3. consolidated porous medium,
4. multi-mode or very large grain or pore size distribution.

According to equation (2.16), the inertial coefficient was expected to be 0.162 for the foam material. Using the numerical simulation, the inertial parameters were evaluated to fit the experimental data.

Fig. 6.2 shows the relative error of the dimensionless friction factor for various inertial coefficients and Reynolds numbers from 20,000~40,000. It is not scaled to the friction factor to clearly see the effects of each case of different zone heights and thickness. Upon a series of computations, the range of fitting for aluminum foam is evaluated from C=0.03~0.05. Fig. 6.2a shows the case of C=0.03 and the dotted box represent the estimated percent relative error is less than $\pm 10\%$. The percent relative error ($e_{r,\%}$) is defined as,

$$e_{r,\%}(\phi) = 100\left(\frac{\phi_e - \phi_n}{\phi_e}\right) \tag{6.1}$$

where ϕ is arbitrary value such as friction factor (f) or Nusselt Number (Nu). Absolute error can be defined as,

$$e_a(\phi) = \left(\phi_e - \phi_n\right) \tag{6.2}$$

It is interesting to see that the inertial parameter is mostly dependent on the pore density (or the internal structure), except for $B_t / D_h = 1/3$ and $B_h / D_h = 1/3$ cases of denser materials.

Fig. 6.2b shows the percent relative error of the dimensionless friction factor for inertial coefficient of 0.04. Again, the cases whose percent relative error is within $\pm 10\%$ are shown in the dotted box. Fig. 6.2c shows the percent relative error of the dimensionless friction factor for the inertial coefficient of 0.05. It is also noted that the case of 20PPI, $B_t / D_h = 1/3$, and $B_h / D_h = 2/3$, is included in this range. This is partially due to the internal structure of the porous media, but it is also due to the fact that the porous medium is occupying only a partial region of the main flow.

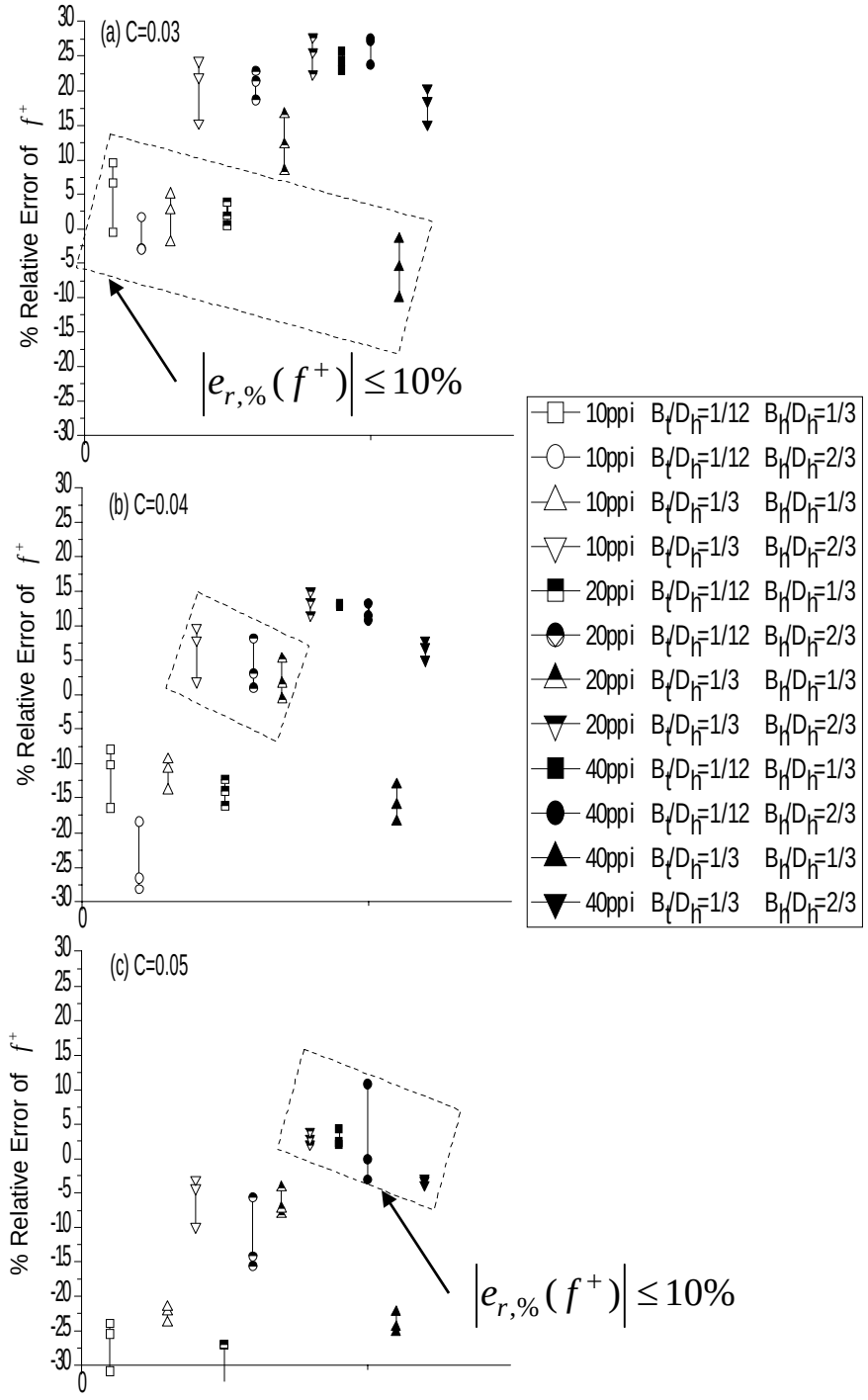

Fig. 6.2. Percent relative error for dimensionless friction factor for various inertial coefficients.

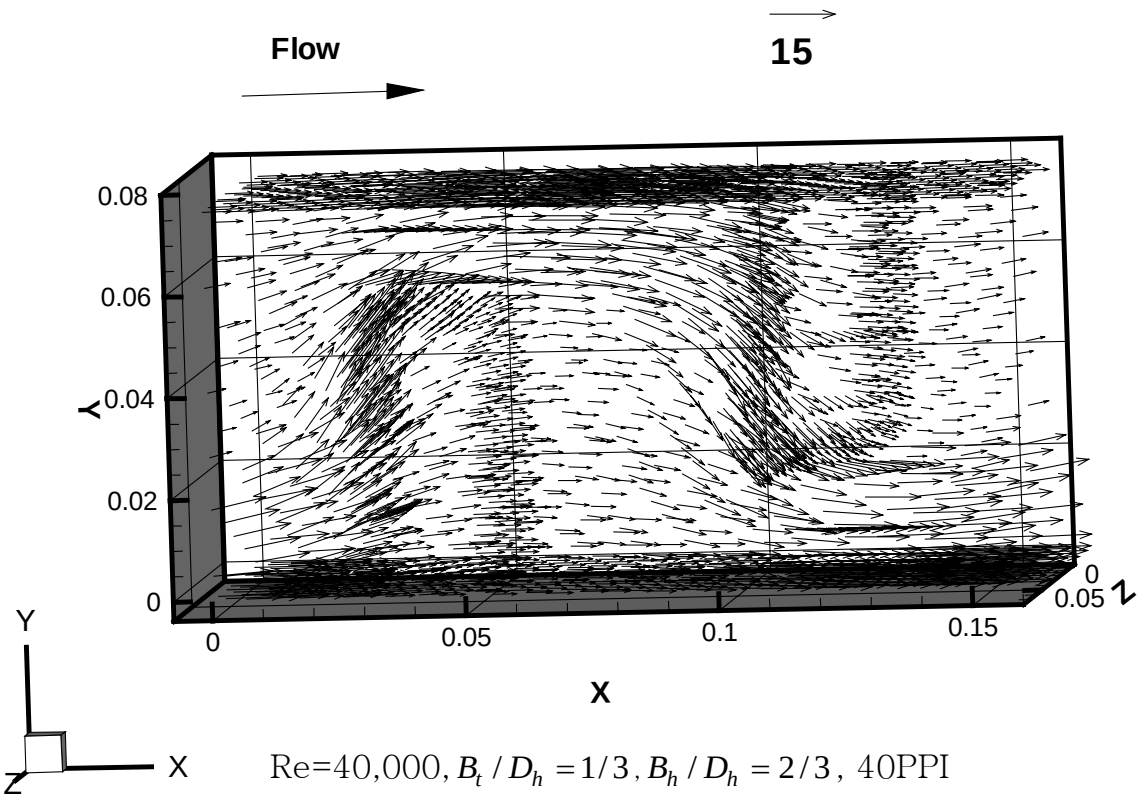

Fig. 6.3. Velocity vectors for a sample case.

When the flow is obstructed by a porous medium, there is extra pressure drop within the porous medium. Fig. 6.3 shows the velocity vectors for $B_t / D_h = 1/3$, $B_h / D_h = 2/3$, 40PPI, and Re=40,000. As clearly shown in Fig. 6.3, due to the obstruction of the main flow, the pressure drop and friction factor were increased. As the effects of transverse flow are large compared to main longitudinal flow due to this obstruction, the Brinkman-Forchheimer-Extended Darcy's law which was correlated with uni-directional flow may not describe the flow correctly.

In Fig. 6.4, the percent relative error for the dimensionless friction factor is plotted as a function of dimensionless friction factor (f^+). Again, the dotted boxes indicate the percent relative error of the friction factor within $\pm 10\%$.

6.2.2 Comparison of Heat Transfer Enhancement

Fig. 6.5 shows the absolute error for the heat transfer enhancement ratio with different sets of inertial coefficients. Each of the figures corresponds to the figures in Fig. 6.4. The variation of the heat transfer enhancement due to the inertial coefficient differences is minor. However, errors increase with the increase in the dimensionless friction factor. To verify this behavior, the percent relative error for the heat transfer enhancement ratio with f_n^+ is plotted in Fig. 6.6. Fig. 6.6 also shows the same trend of increase in error with increase in the dimensionless friction factor. The maximum percent relative error is about 30. The effective conductivity used for the conventional model is higher than the actually reported value of 6.0 due to high porosity and neglected thermal resistance between the fluid and solid interfaces.

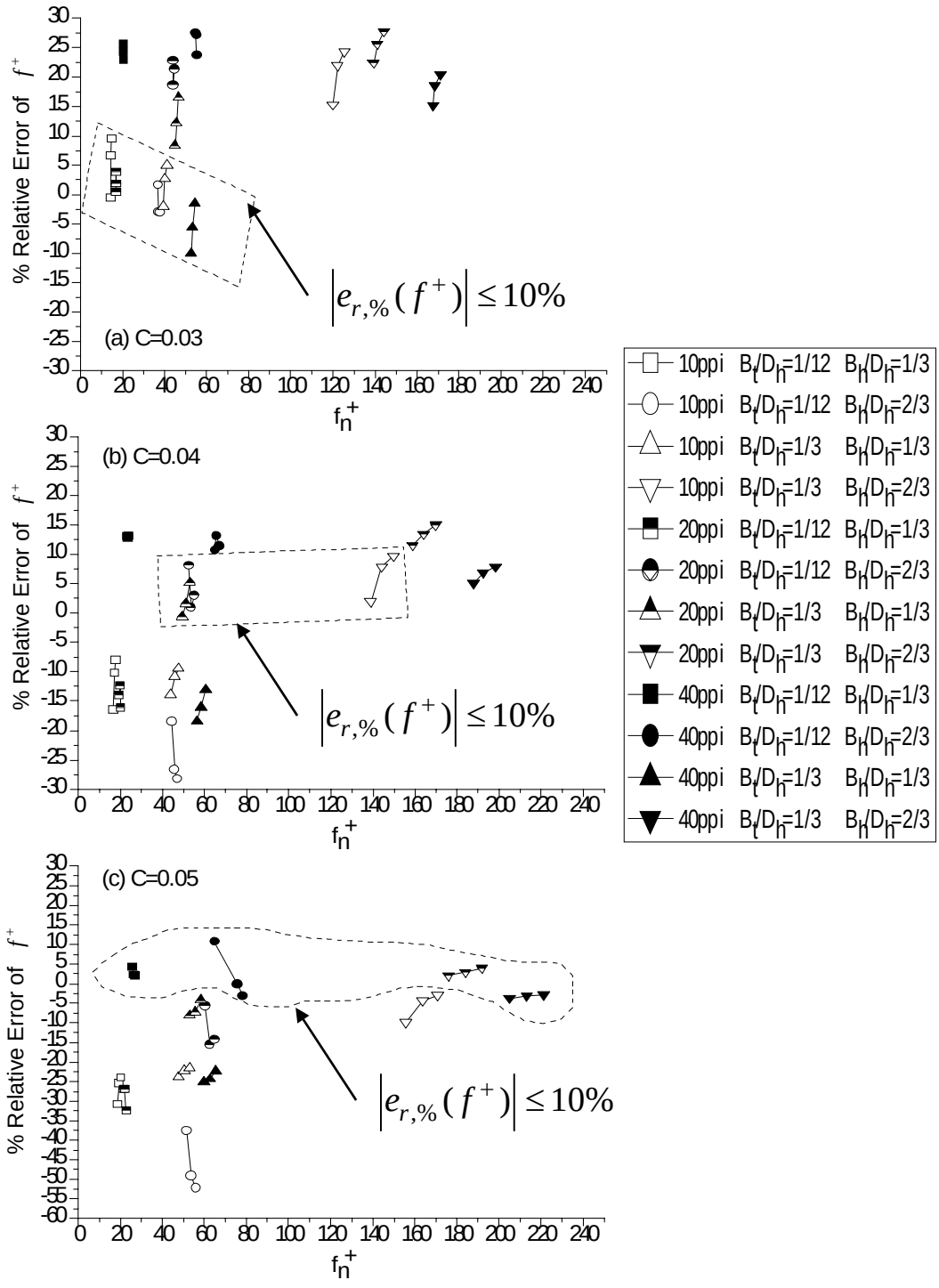

Fig. 6.4. Percent relative error for dimensionless friction factor for various inertial coefficients (plotted against dimensionless friction factor).

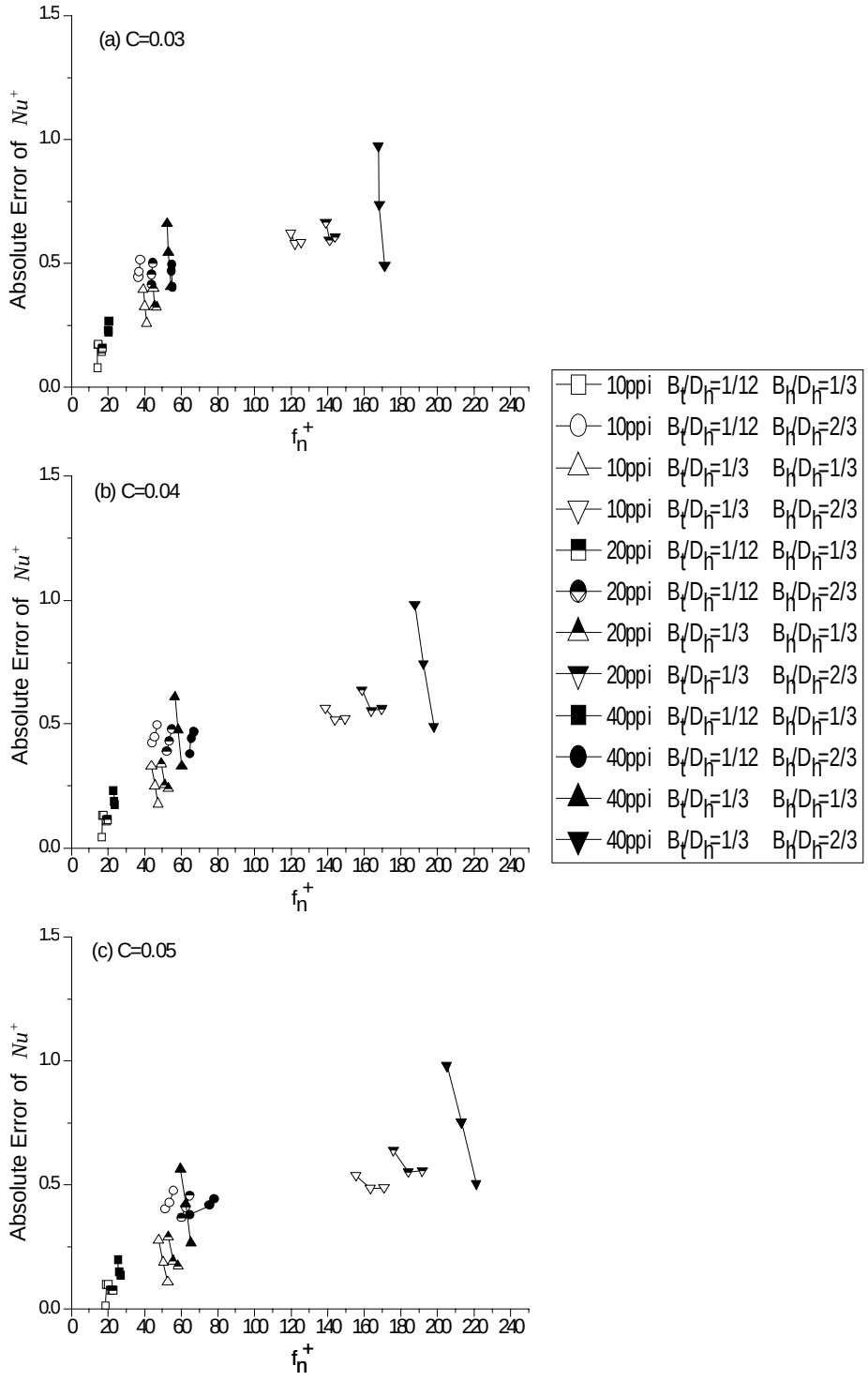

Fig. 6.5. Absolute error for the heat transfer enhancement ratio for the various inertial coefficients.

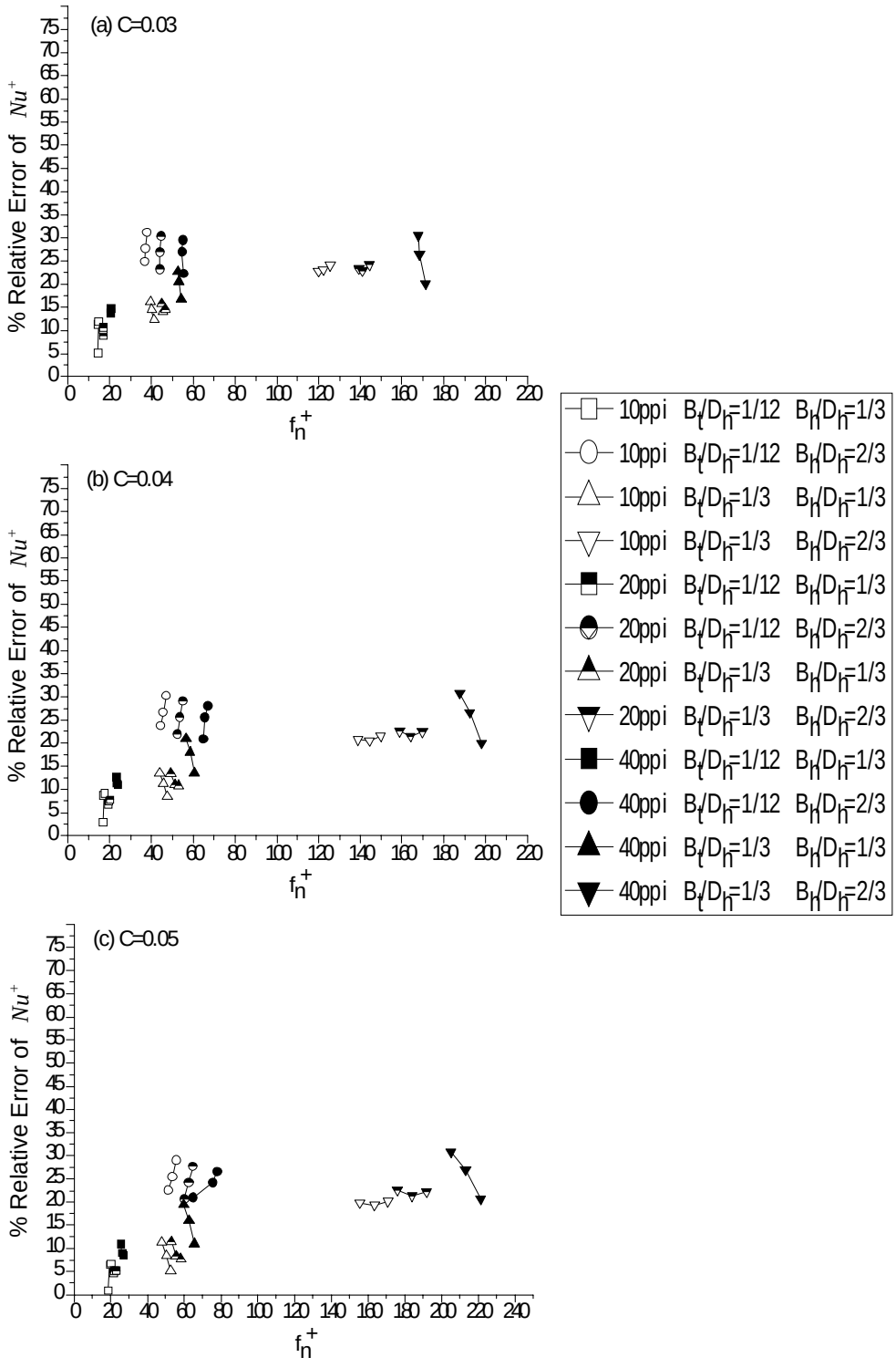

Fig. 6.6. Relative error for the heat transfer enhancement ratio for the various inertial coefficients.

6.2.3 Comparison of Heat Transfer Enhancement and Dimensionless Friction Factor for Selected Inertial Coefficients

Fig. 6.7 and 6.8 show the error in heat transfer enhancement and dimensionless friction factor for appropriate inertial coefficients. Again, while the percent relative error is less than 10 for the dimensionless friction factor, the relative error for the Nusselt number is increasing with the dimensionless friction factor, and the maximum percent relative error for Nusselt number is about 30.

6.2.4 Turbulent Conductivity

The error in the prediction of the heat transfer enhancement may be attributed to incorrect modeling of the effective thermal conductivity, neglecting the local thermal non-equilibrium, anisotropic properties of real medium, and inaccurate approximation of turbulence mechanism inside the porous medium. The turbulent production rate is proportional to the gradient of velocity. Due to the velocity reduction inside of porous medium, the production rate is decreasing. This may hold for clear fluid cases but interaction and dissipation inside of the porous medium is not taken into account directly in conjunction with the turbulence model for any of the known turbulence models.

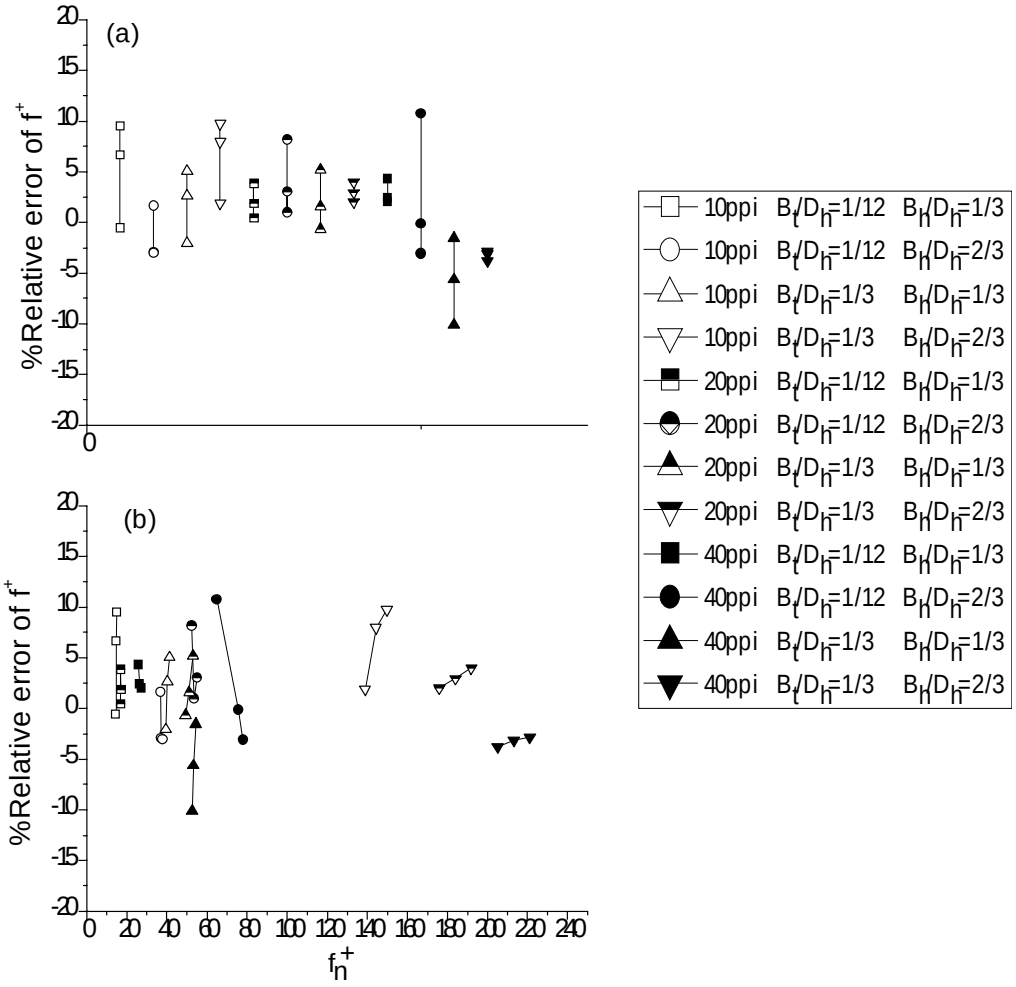

Fig. 6.7. Absolute and relative error for the dimensionless friction factor with corrected inertial coefficients.

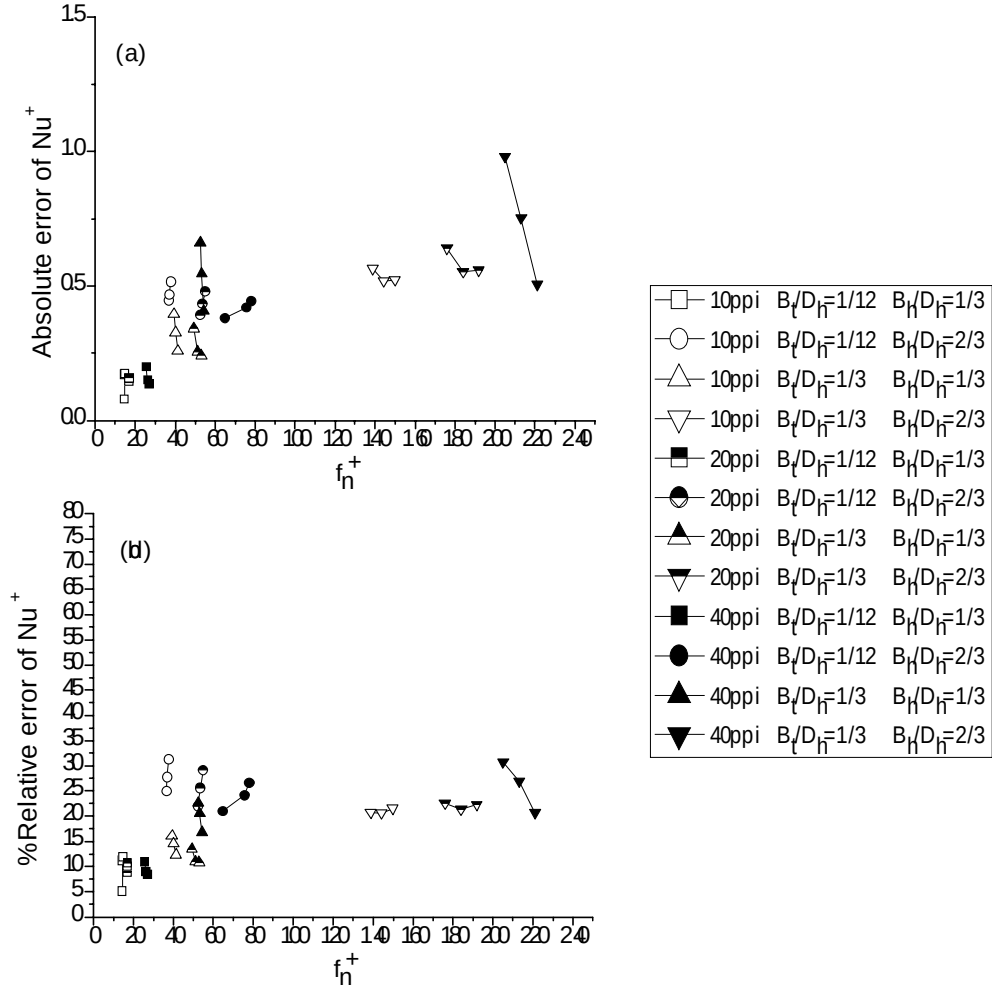

Fig. 6.8. Absolute and relative error for Nu^{+} with corrected inertial coefficients.

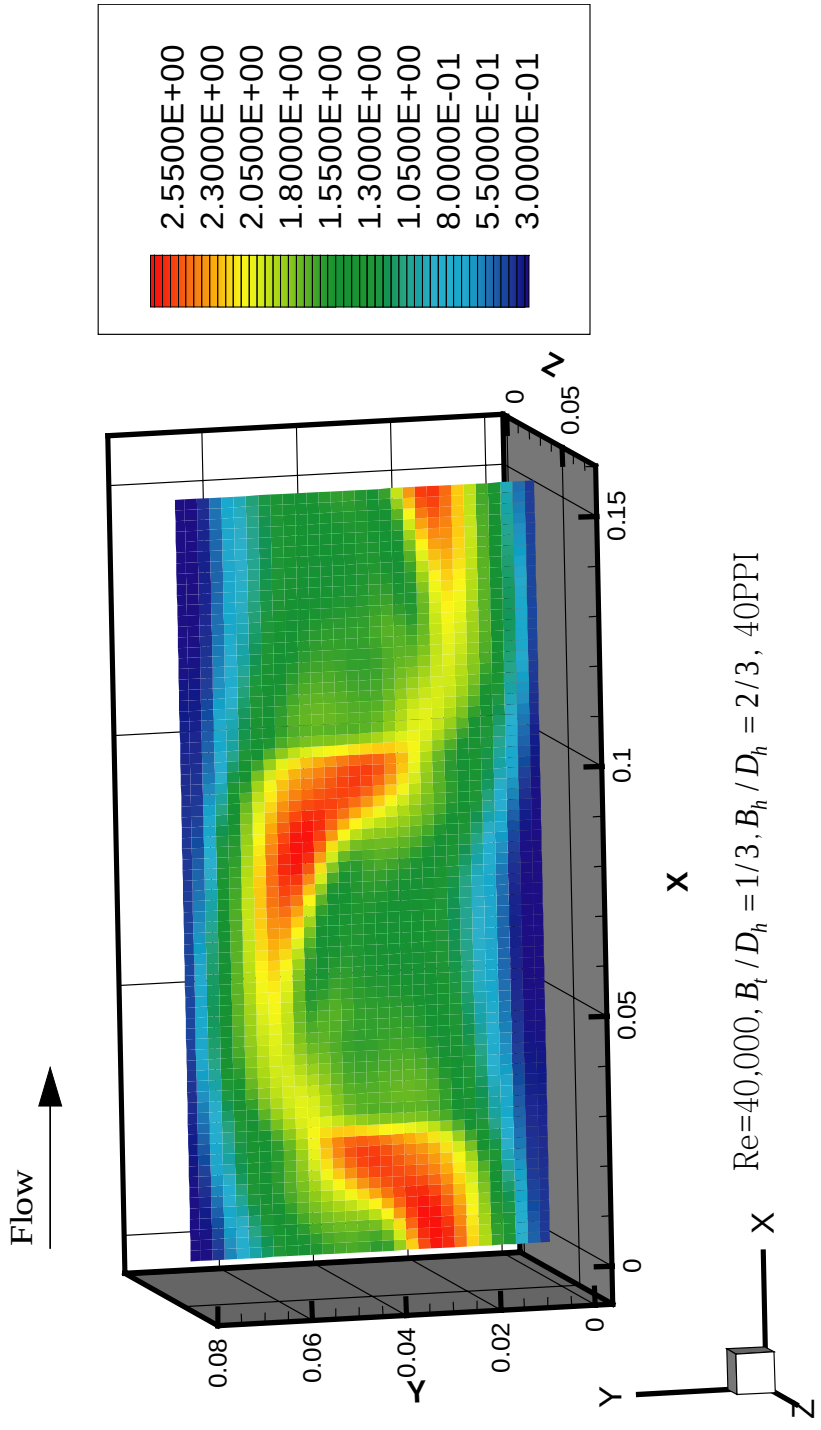

Fig. 6.9. Turbulent conductivity at the central plane for a sample case (unit: W/m-K).

Fig. 6.9 shows the turbulent conductivity for $B_t / D_h = 1/3$, $B_h / D_h = 2/3$, 40PPI, Re=40,000, and C=0.05. The turbulent conductivity ranges from 0.25 to 2.5. But the turbulent conductivity inside of porous zone is very small as $O(-2) \sim O(-1)$ near the wall. Thus, the overall contribution of turbulence conductivity is very minor compared to the effective conductivity. However, this statement is not validated because no experimental data is available to author's knowledge.

The contribution of turbulence is actually taken into account in equation (2.49) as a form of dispersion conductivity, but correlations of this dispersion conductivity were mostly performed at low Reynolds numbers, with fully saturated and filled medium, and with spherical beads. Thus, the actual contribution of this dispersion conductivity is yet to be determined.

6.2.5 Velocity Distribution

Fig. 6.10-Fig. 6.12 show the velocity distributions in the x, y, and z directions. In x-directional velocity distribution (Fig. 6.10), the velocity was greatly reduced due to the porous baffles for both the top and bottom walls. The distribution of the velocity inside of the porous baffles showed a parabolic shape due to channeling effects.

The flow is diverted to y-direction due to the porous baffles (Fig. 6.11). But the z-directional velocity is very low at the centerline due to the symmetric condition. In Fig. 6.12, the z-directional velocity near the front region of the porous baffles is relatively high due to the wall and porous baffles. The multiple of arbitrarily chosen planes in the x-direction are shown for the investigation of the local z-directional velocities.

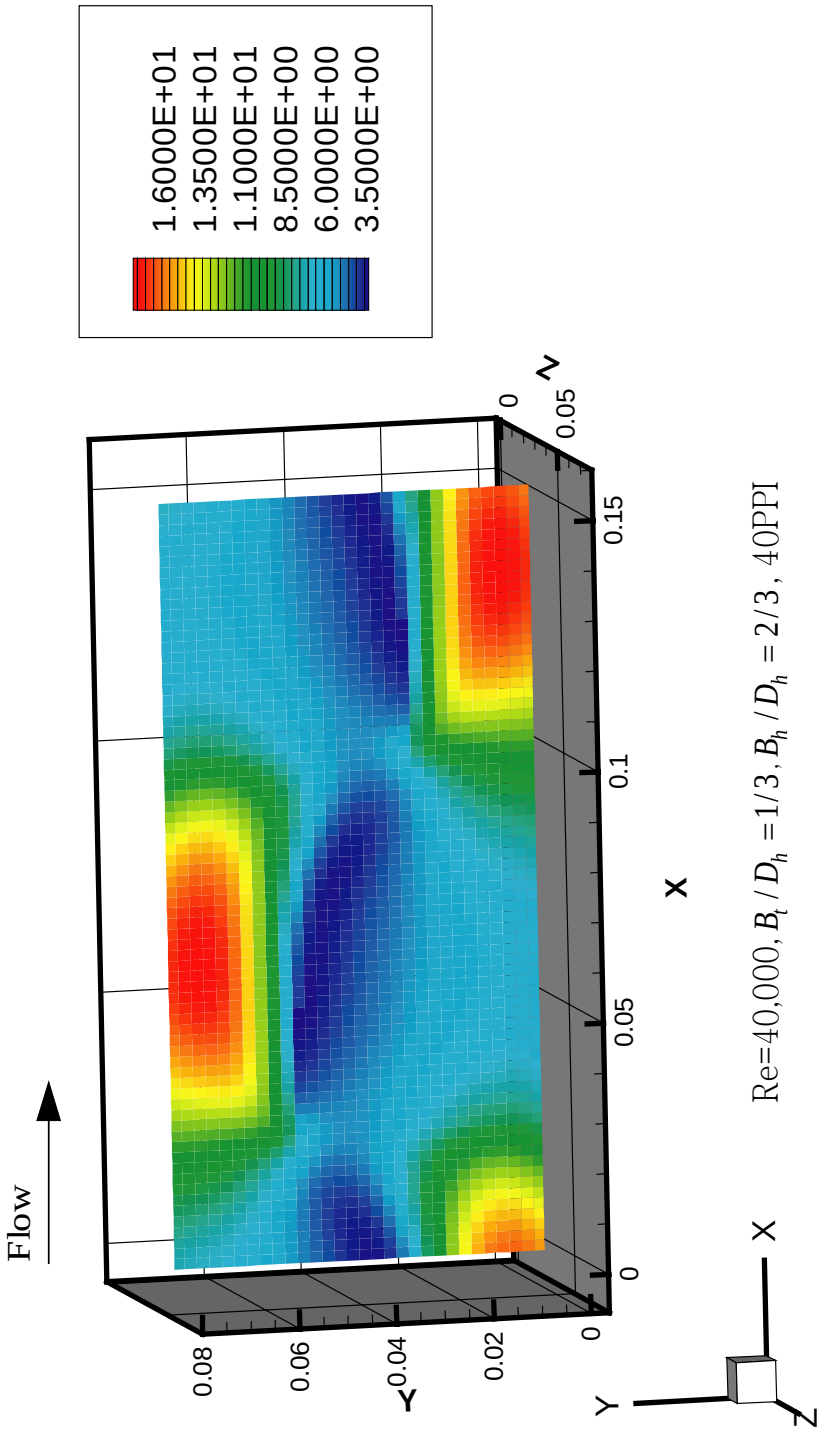

Fig. 6.10. X-directional velocity distribution at the central plane for a sample case (unit: m/s).

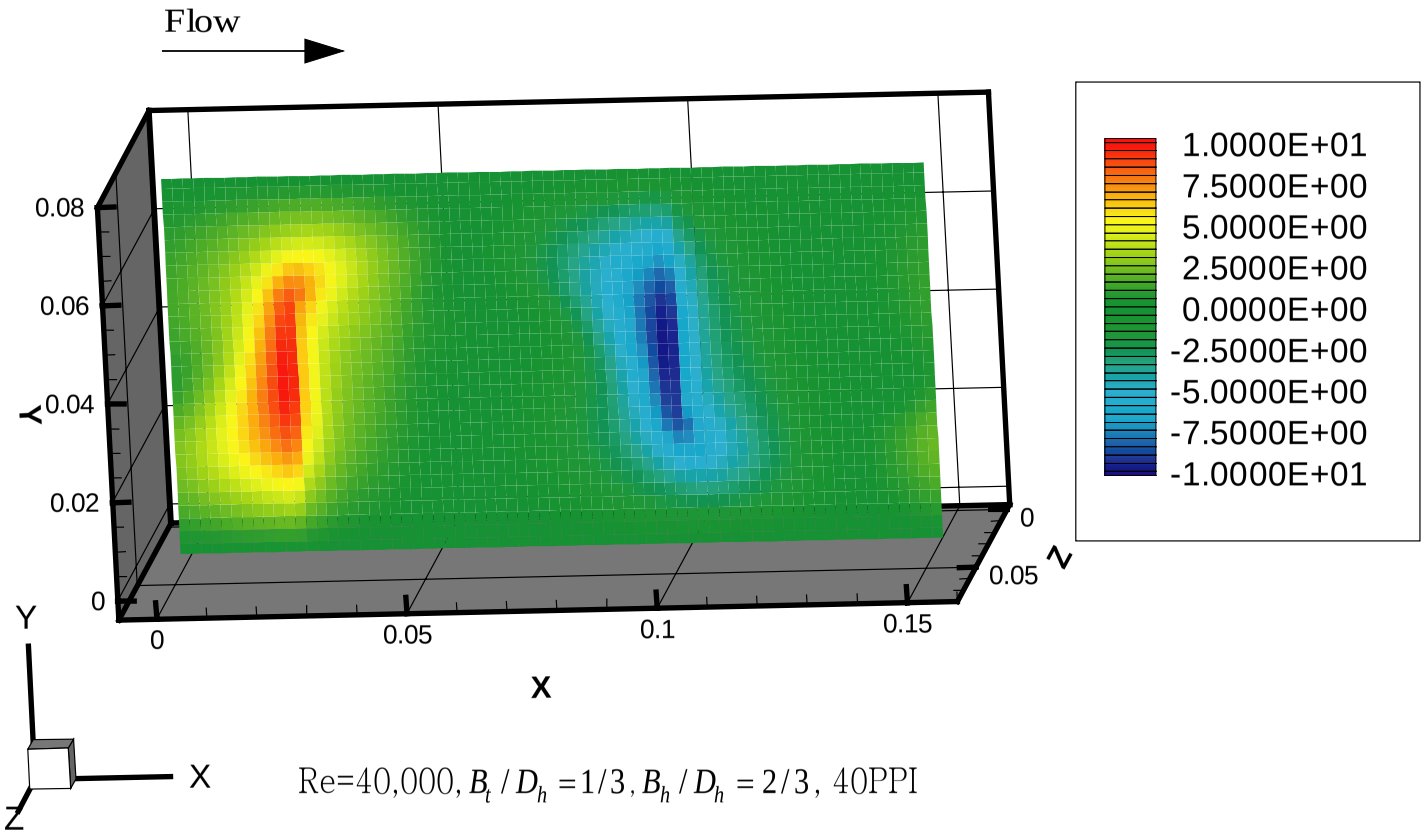

Fig. 6.11. Y-directional velocity distribution at the central plane for a sample case (unit: m/s).

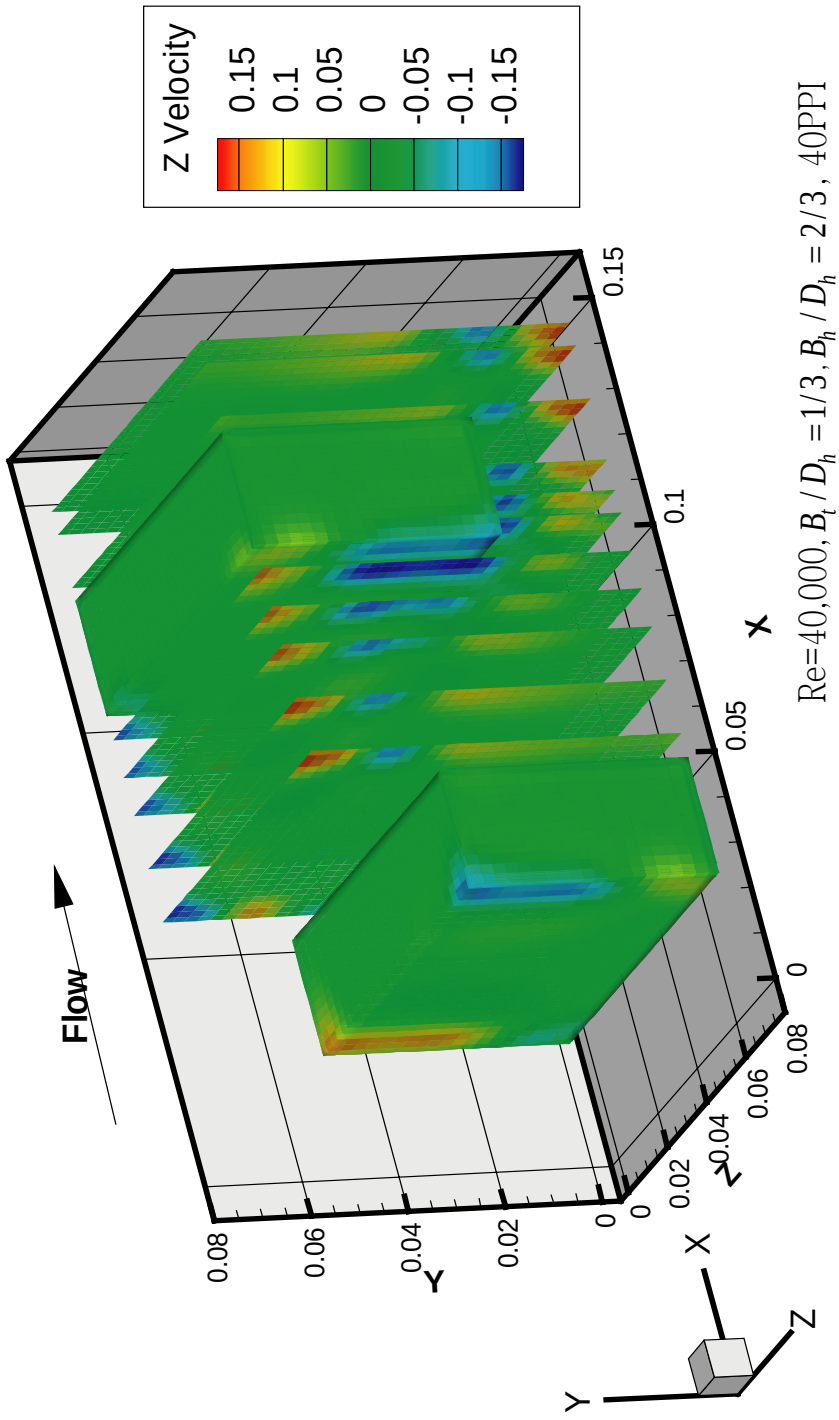

Fig. 6.12. Z-directional velocity distribution at various locations for a sample case (unit: m/s).

6.2.6 Temperature Distribution

Fig. 6.13 shows the temperature distribution for a sample case of $B_t / D_h = 1/3$, $B_h / D_h = 2/3$, 40PPI, and Re=40,000. Steep gradients of temperature near the wall show the importance of the correct information resolution near the wall region. While the flow passes through the porous media due to the high conductivity, the temperature of the flow rises slightly due to heat transfer from the porous wall. The end corners of the porous baffles in z-direction have highest temperature due to the low flow velocity in this region.

6.2.7 Turbulent Kinetic Energy and Turbulent Dissipation Rate

Fig. 6.14 and 6.15 show the turbulent kinetic energy and turbulent dissipation rate for the $B_t / D_h = 1/3$, $B_h / D_h = 2/3$, 40PPI, and Re=40,000 case. The turbulent kinetic energy reduced by 10% of the maximum turbulent kinetic energy in the lower region of the porous baffles. However, for the top portion of the baffles, the turbulent kinetic energy is comparably larger than the other portion of the baffles. Generally, due to the dramatic reduction of the flow velocity inside of the porous zone, it is accepted that the consideration of turbulence inside of porous zone is negligible. This may be true for the base zone of the porous baffle, but is not necessarily true for the entire area. Currently there is no rigorous study on this matter.

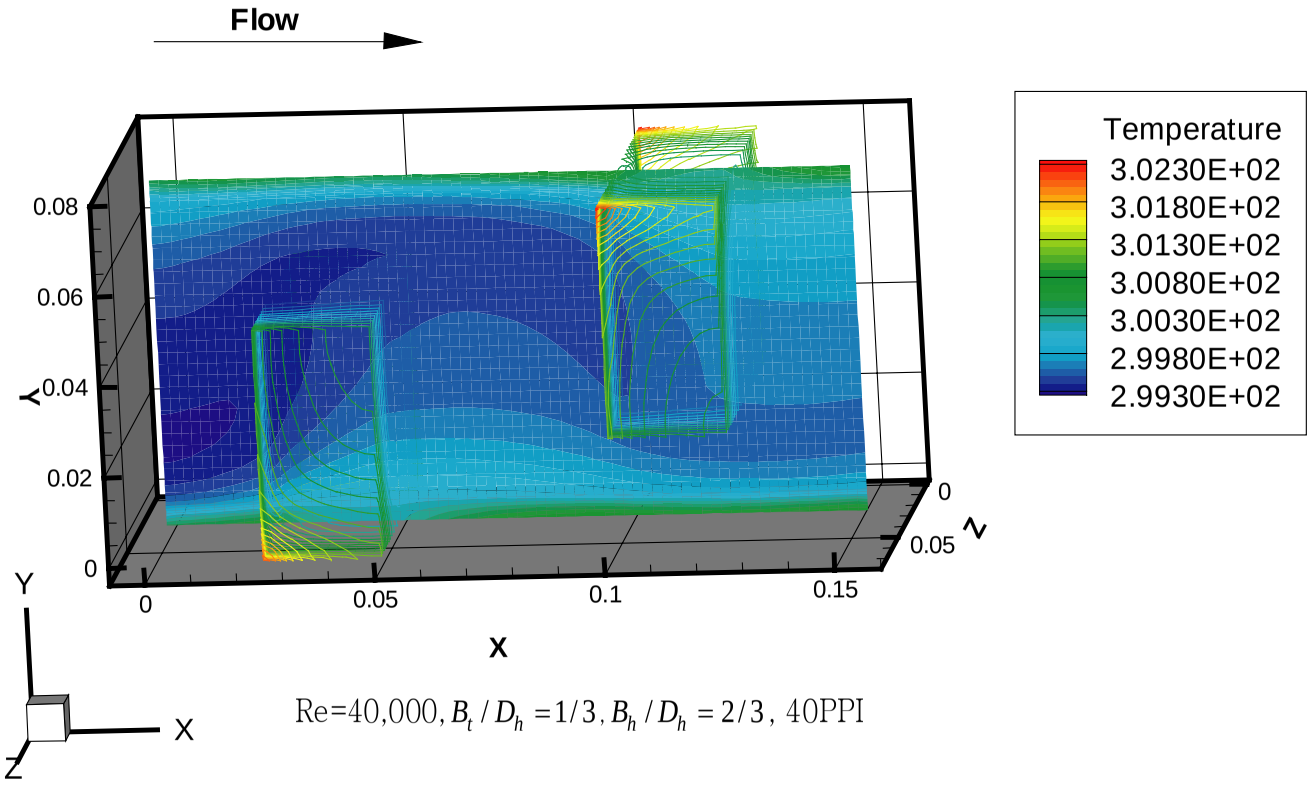

Fig. 6.13. Temperature distribution at the central plane for a sample case (unit: ℃).

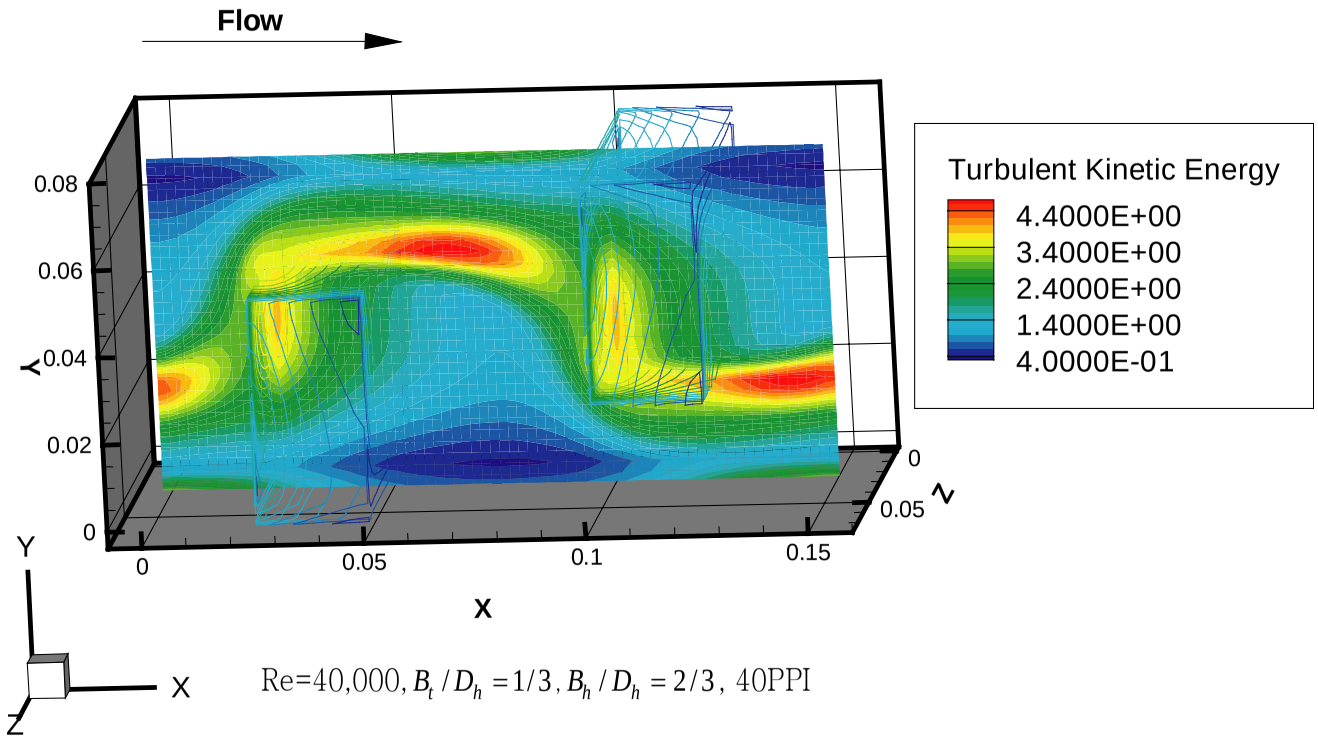

Fig. 6.14. Turbulent kinetic energy distribution at the central plane for a sample case (unit: J/Kg).

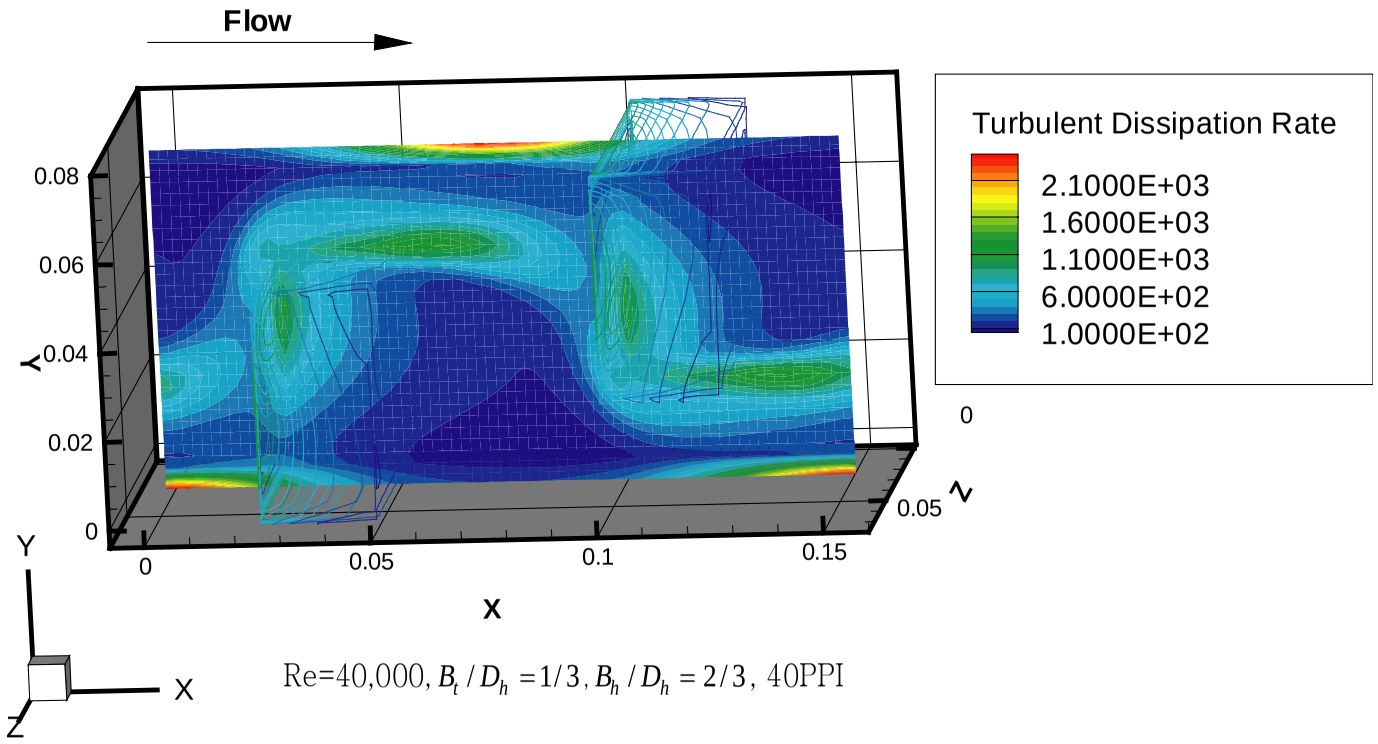

Fig. 6.15. Turbulent dissipation rate distribution at the central plane for a sample case (unit: m^2/s^3).

6.3 Results of One-Equation Model

6.3.1 Dependency of Heuristic Coefficients

Fig. 6.16 shows the variation of the heat transfer enhancement ratio (Nu^+) as a function of the heuristic coefficient (D_t). The concept of the heuristic coefficient (D_t) was originally given by Hsu and Cheng's [26] model. Hsu and Cheng's experiments were conducted under fully saturated, fully filled, sintered sphere beads, and at lower Reynolds number ($Re = 100 - 5000$). Accordingly, the higher values of D_t were chosen for this study.

It is evident from Fig. 6.16 that for $D_t \geq 100$ the corresponding one-equation model predictions cease to vary with D_t and a substantial difference between the experimental and numerical values remain ($\sim 13\%$). This is attributed to the limitation of the one-equation model.

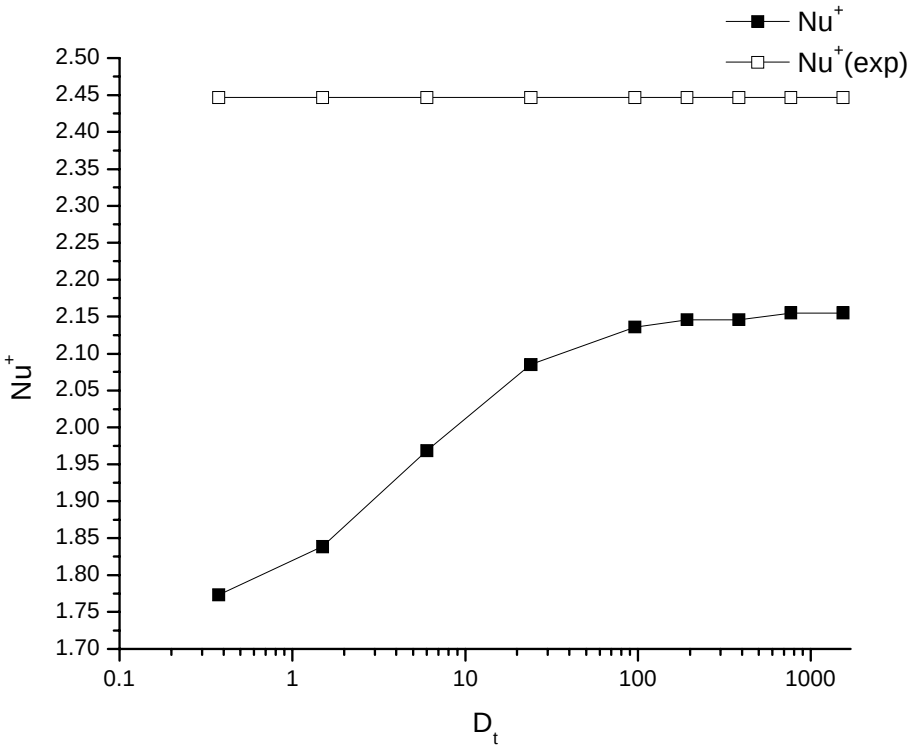

$B_t / D_h = 1/3$, $B_h / D_h = 2/3$, 40PPI, Re=40,000, and C=0.05

Fig. 6.16. Comparison of the Nusselt number variations against D_t for the one-equation model.

6.3.2 Comparison of Heat Transfer Enhancement

Fig. 6.17 and 6.18 show the comparison of the heat transfer enhancement ratio for the conventional model, one-equation model with ω =1.5, D_t =10, one-equation model with ω =1.5, D_t =100, and one-equation model with ω =0.5, D_t =100, respectively.

The first thing to notice is the reduction of error from 30 to 10% for the cases of thin and high porous baffles. Secondly, the overall reduction of error is about 5% for the cases of strong pressure drop across the baffles.

Comparing Fig. 6.17a and 6.17b does not show much difference while it is expected to be larger since D_t is about 30 times larger than the one from the original literature. This is because for the Fig. 6.17b cases, the actual values, which are lower than theoretical values, of effective thermal conductivity (K_f^*) were used, and additional effects of thermal dispersion come up to the level of the total thermal effective conductivity, which was used in the conventional model.

Fig. 6.18a shows much lower values than the ones in Fig. 6.17a, and also, the overall reduction of error by 3-4% compared to the ones in Fig. 6.17b. The effect of ω can be compared with Fig. 6.18b and the difference is minor compared to the effects of D_t.

Even though the overall errors are reduced by this approach there are still the proportional errors which cannot be explained well with the one-equation model approach.

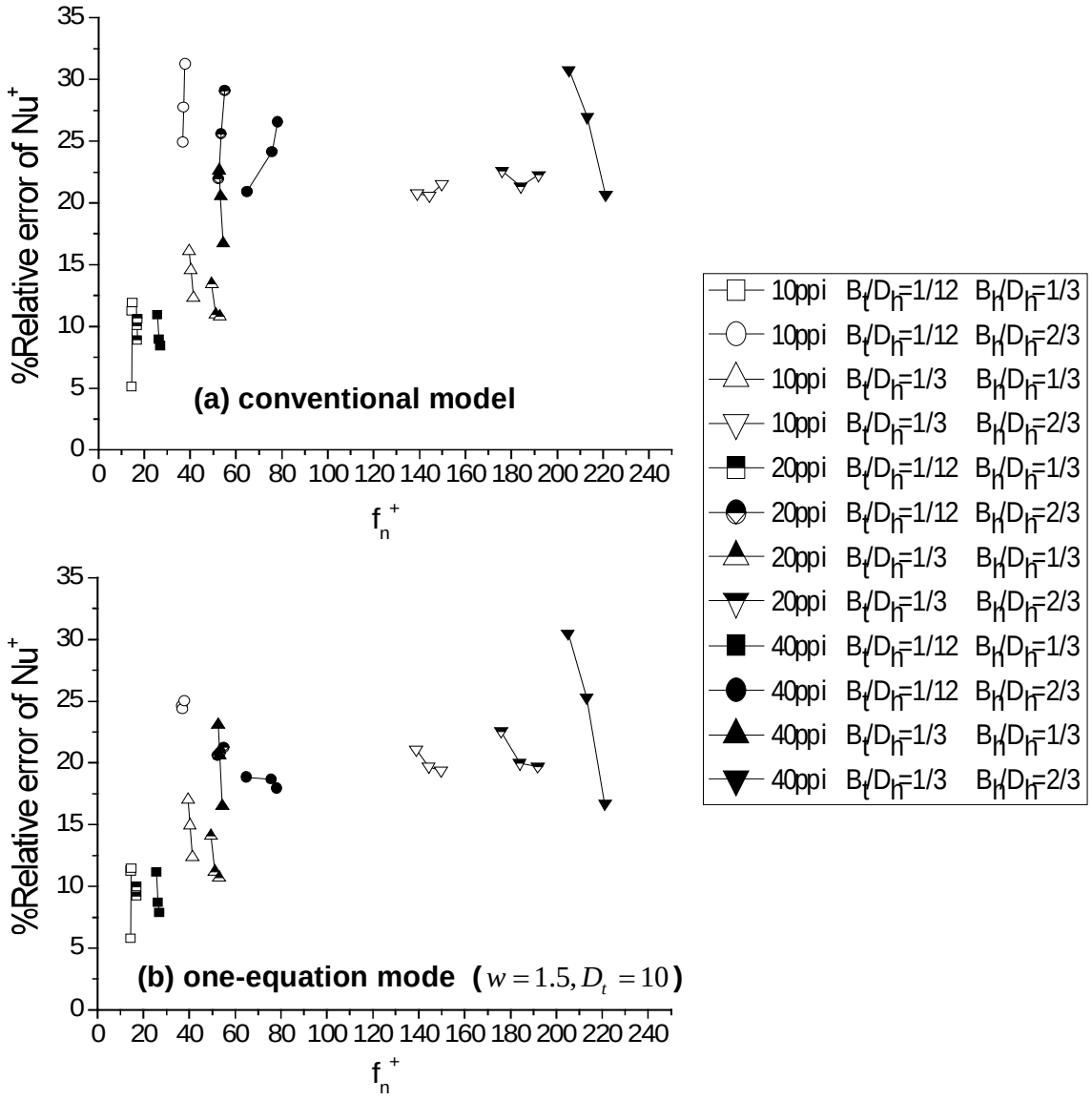

Fig. 6.17. Comparison of percent relative error for heat transfer enhancement ratio for the one-equation model (conventional and $D_t = 10$).

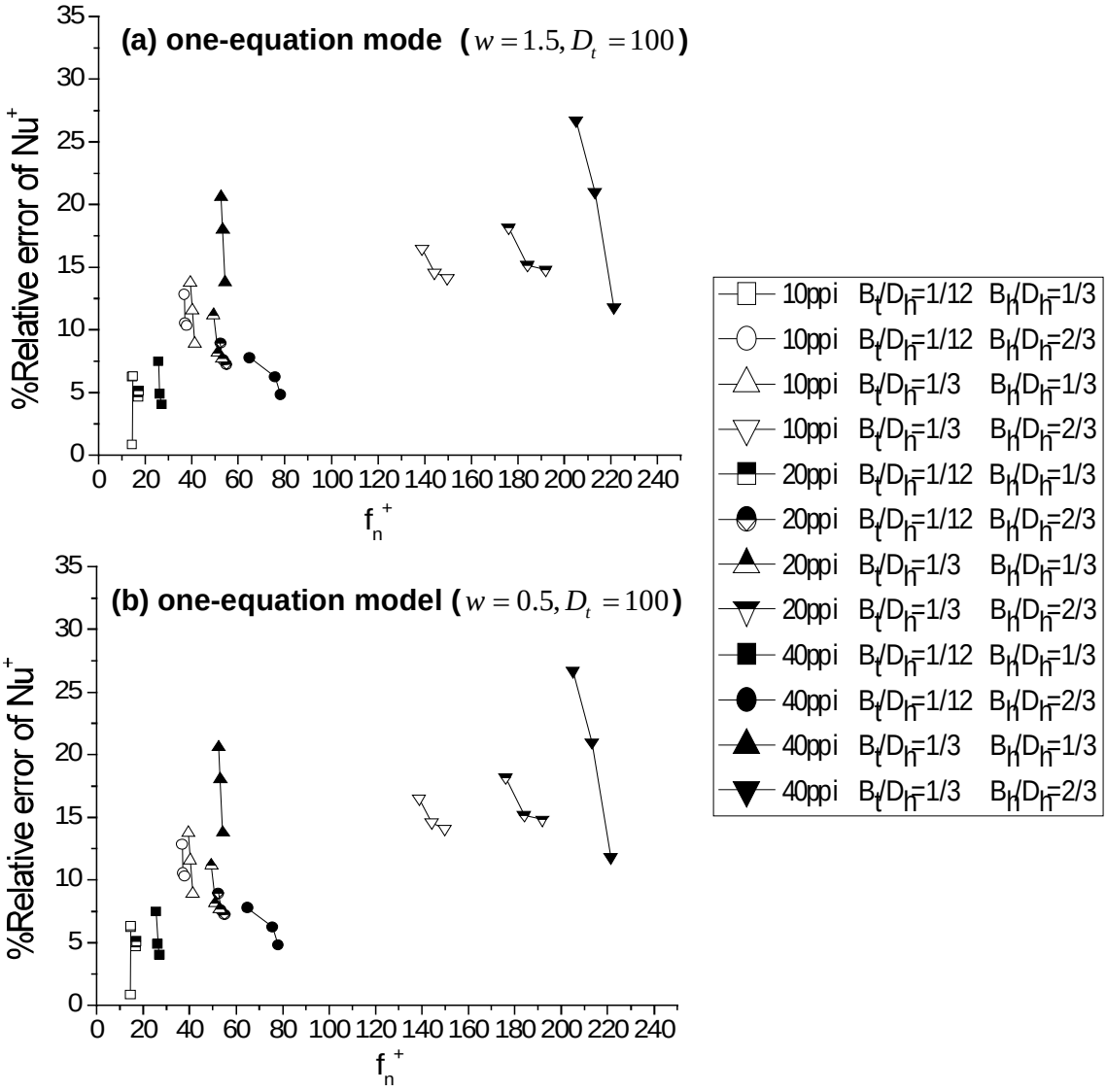

Fig. 6.18. Comparison of percent relative error for heat transfer enhancement ratio for the one-equation model ($w = 1.5$ and $w = 0.5$).

6.4 Results of Two-Equation Model

6.4.1 Comparison of All Models

Fig. 6.19 shows the variation of Nu^+ with D_t with the one-equation model and the two-equation model for the case of $B_t / D_h = 1/3$, $B_h / D_h = 2/3$, 40PPI, Re=40,000, and C=0.05. The coefficients for the two-equation model were used with its original values except for the evaluation of the interface area (equation (2.59) and (2.60)).

With a series of tests, the two-equation model showed little or no improvement over the results of the one-equation model. The maximum value of D_t showed the convergence was 50.

In the range of $D_t = 0.375 \sim 10.0$, it is shown that the dispersion conductivity (K_d) and interface heat flux (q_{sf}) share the over all effects of the heat transfer mechanism. However for values greater than $D_t = 10$, the effects of the interfacial heat flux faded, and only the dispersion conductivity played a role in this region.

In order to get a better match between numerical predictions and experimental data, two-equation model based on the local non-thermal equilibrium was adapted, but it is evident from Fig. 6.19 that the performance of the two-equation model is not much different from that of the one-equation model. The difference in performance between the one-equation and the two-equation models for $D_t \leq 10$ (Fig. 6.19) is attributed to the interfacial heat transfer between solid and fluid phases.

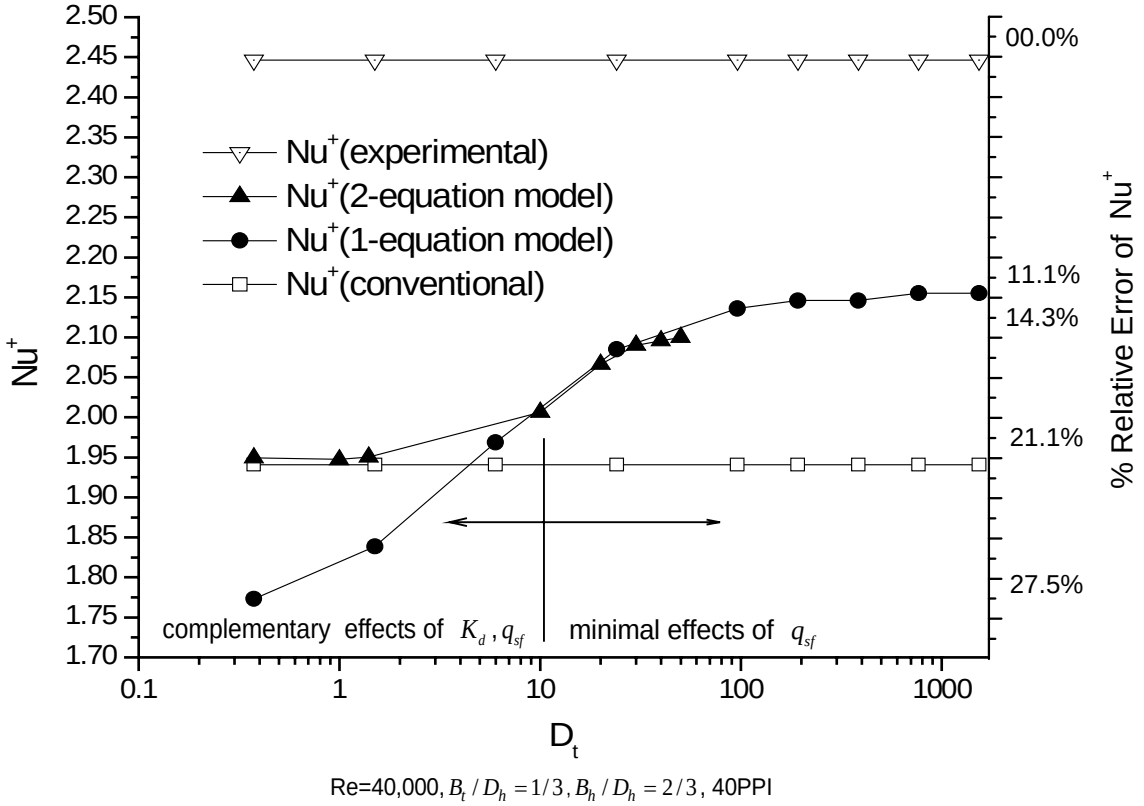

Fig. 6.19. Comparison of the Nusselt number variations with D_t for the two-equation model.

There are a few aspects to be considered to improve this discrepancy. Firstly, the classical model to describe the resistance of the porous media was based on sphere bead type geometry. Thus, another form of correlations may exist for specific foam material. The internal structure of the foam material can be very different from that of porous medium which is comprised of spherical beads.

Secondly, due to the lack of relevant studies of heat transfer mechanism near the wall region, the adopted turbulence model may not be able to describe the actual heat transfer mechanism near the wall. Along with the turbulence model, the wall function limitation prohibited the higher resolution of the grid near the wall, and the validity of wall function inside of the porous region has to be resolved. Also, the clear fluid region may be affected by this limitation.

Thirdly, due to the limitation of the commercial code, the exact form of convection and diffusion term in the momentum equation could not be used. However, due to the high porosity value, it is expected that this error is very small compared to the other sources of error.

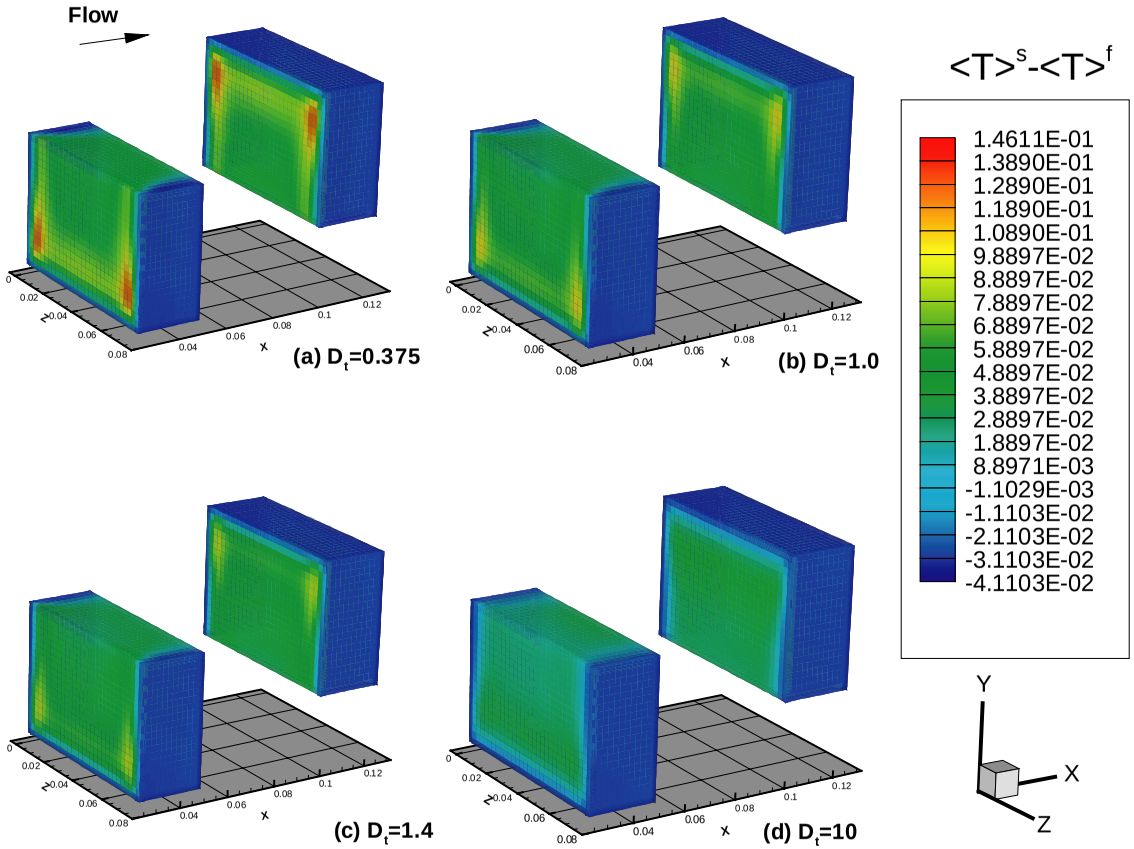

Fig. 6.20. Temperature difference between two phases for a sample case (D_t=0.375~10).

6.4.2 Temperature Difference between the Two Phases

Fig. 6.20 and 6.21 show the temperature difference ($\langle T \rangle^s - \langle T \rangle^f$) between the fluid and solid phases in the porous baffles for the sample cases of $B_t / D_h = 1/3$, $B_h / D_h = 2/3$, 40PPI, Re=40,000, and C=0.05 with the color scale fixed with $D_t = 0.375$ case to compare the overall temperature variation due to the variation of D_t.

In Fig. 6.20, the temperature difference ($\langle T \rangle^s - \langle T \rangle^f$) gradually reduced by the order of 10^{-2} for value larger than $D_t = 1.4$. This can also be confirmed by Fig. 6.21. The temperature difference ($\langle T \rangle^s - \langle T \rangle^f$) is even further reduced to the level of the gradient of the variation is almost zero.

Physically the temperature near the wall is the same for the solid and fluid phase temperatures. Thus, the temperature difference is close to zero, but due to the high conductivity of the solid phase, dispersion conductivity, and convective heat transfer of the fluid phase the solid phase, temperature is reduced abruptly out of the near wall region. However, as the conduction effects become greater, the temperature difference decreases but it is uniformly distributed throughout the entire porous baffles.

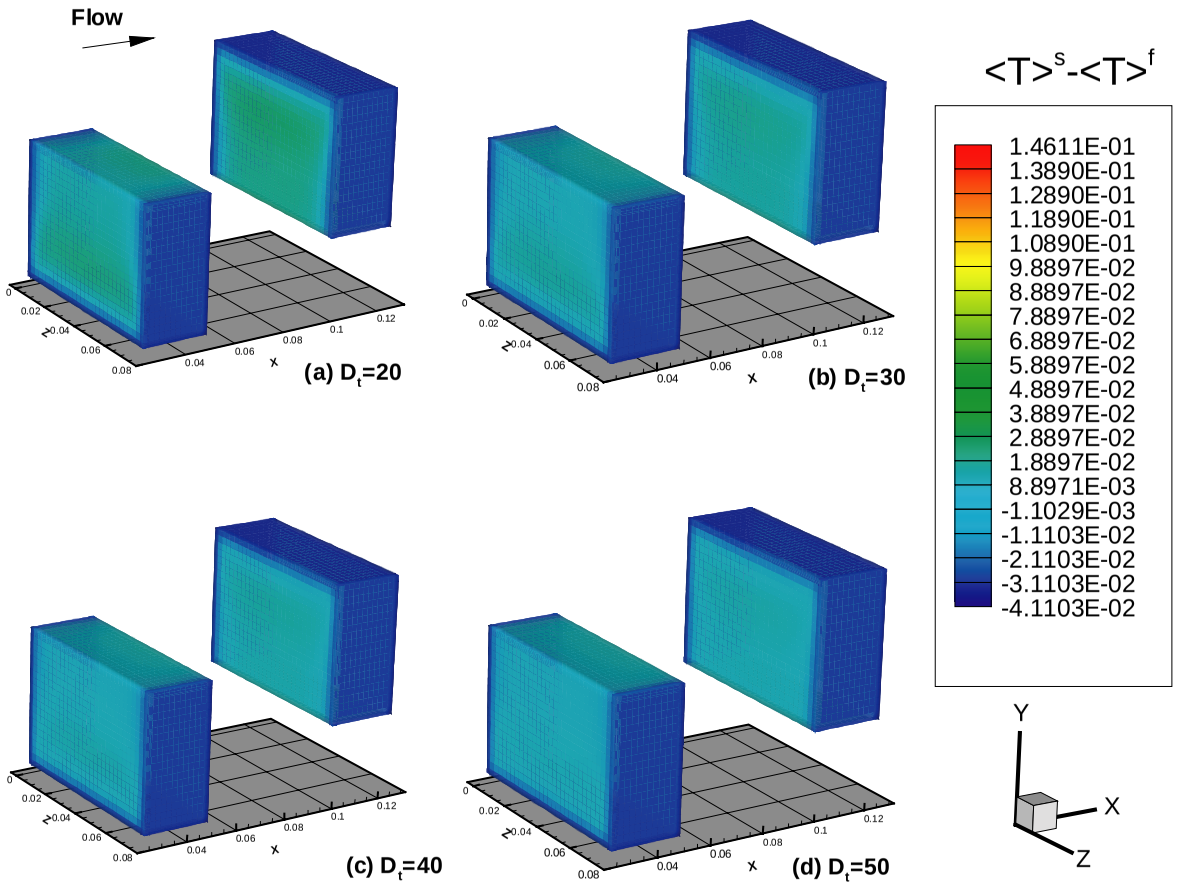

Fig. 6.21. Temperature difference between two phases for a sample case (D_t=20~50).

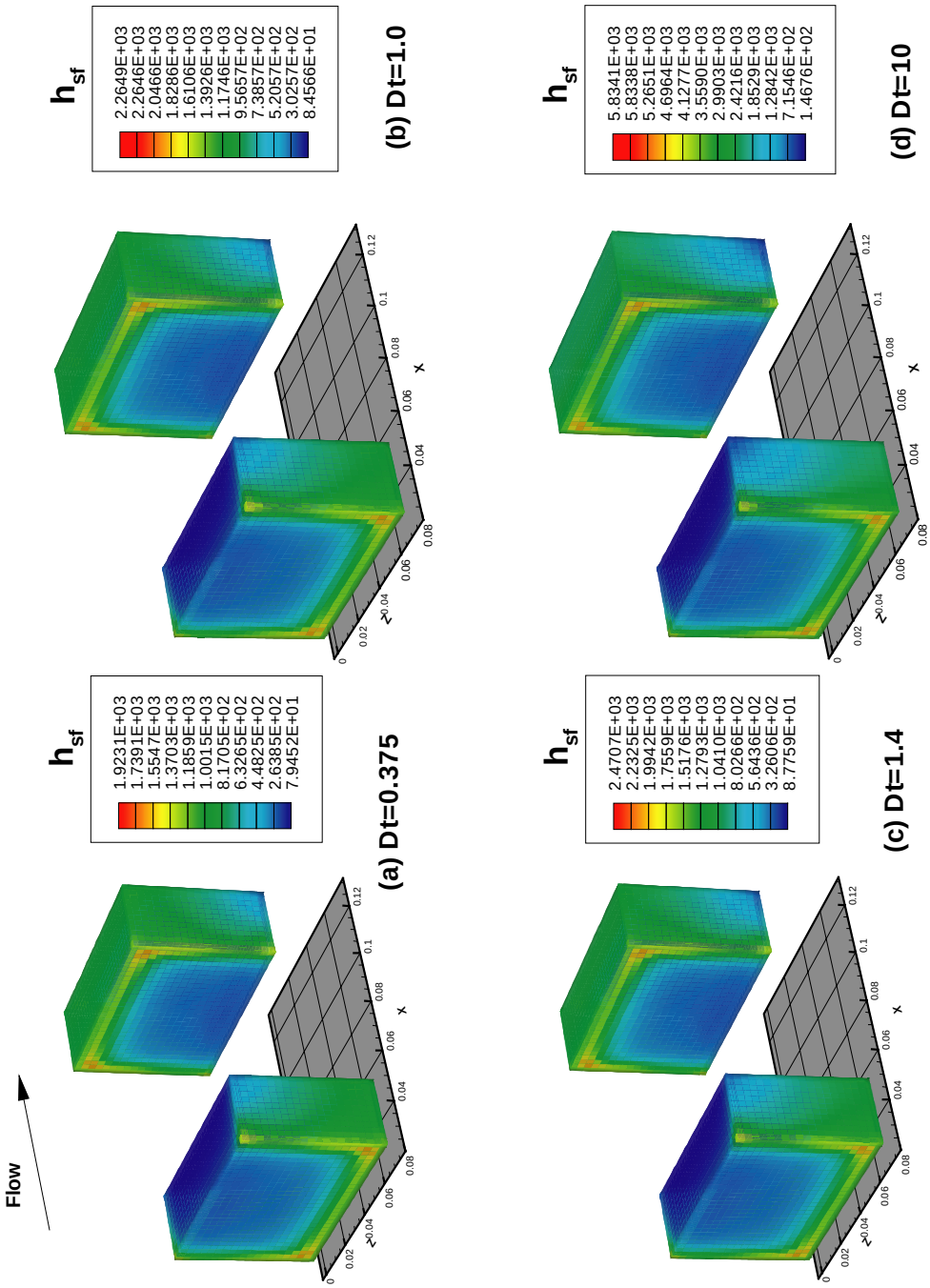

Fig. 6.22. Heat transfer coefficient variations for a sample case (D_t=0.375~10).

6.4.3 Interfacial Heat Transfer Coefficient (h_{sf})

Fig. 6.22 and 6.23 shows the interfacial heat transfer coefficients for the case of $B_t / D_h = 1/3$, $B_h / D_h = 2/3$, 40PPI, Re=40,000, and C=0.05 for various D_t. While the normalized distribution is nearly same for all values of D_t, the absolute value of heat transfer coefficient increased from 1,900~16,000 $W / m^2 °C$.

Since the heat transfer coefficients are modified to be sensitized to the local conductivity the distribution of the heat transfer coefficients are higher in the wall region. Using this method, the variable porosity method, to simulate the higher heat transfer rate near the wall zone due to the channeling effects does not have to be included. The velocity effects are reflected through the Reynolds number intrinsically.

However, the modified heat transfer coefficient does not have the term to reflect different properties which retain the internal structural variation, other than porosity, such as pore density, permeability, or Darcy number. This is also an aspect to be considered to improve the prediction capability. In this study, the two-equation model does not improve the predictions of heat transfer significantly nor stabilize the solution procedure for turbulent forced convective flow and heat transfer in porous media.

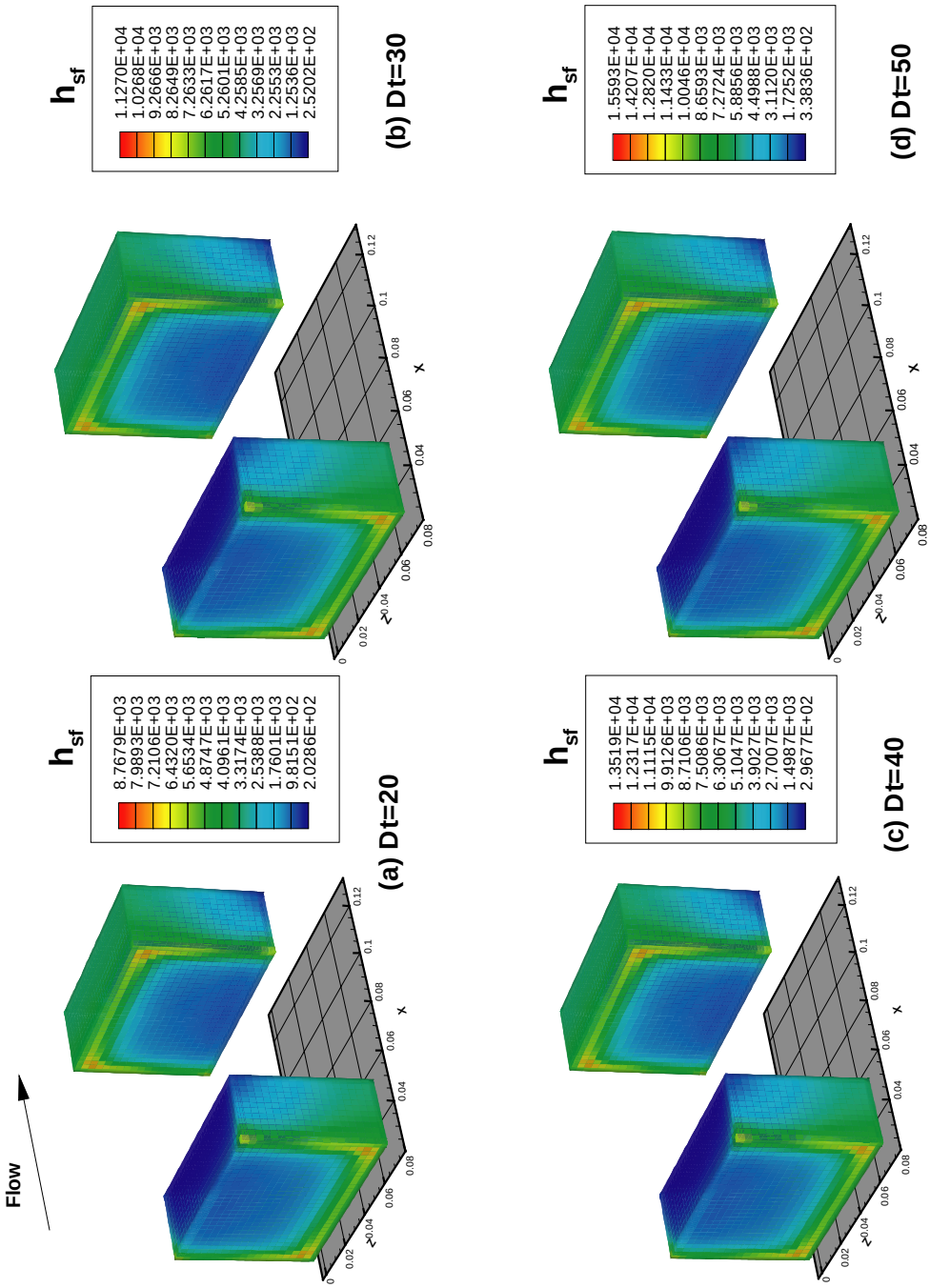

Fig. 6.23. Heat transfer coefficient variations for a sample case (D_t=20~50).

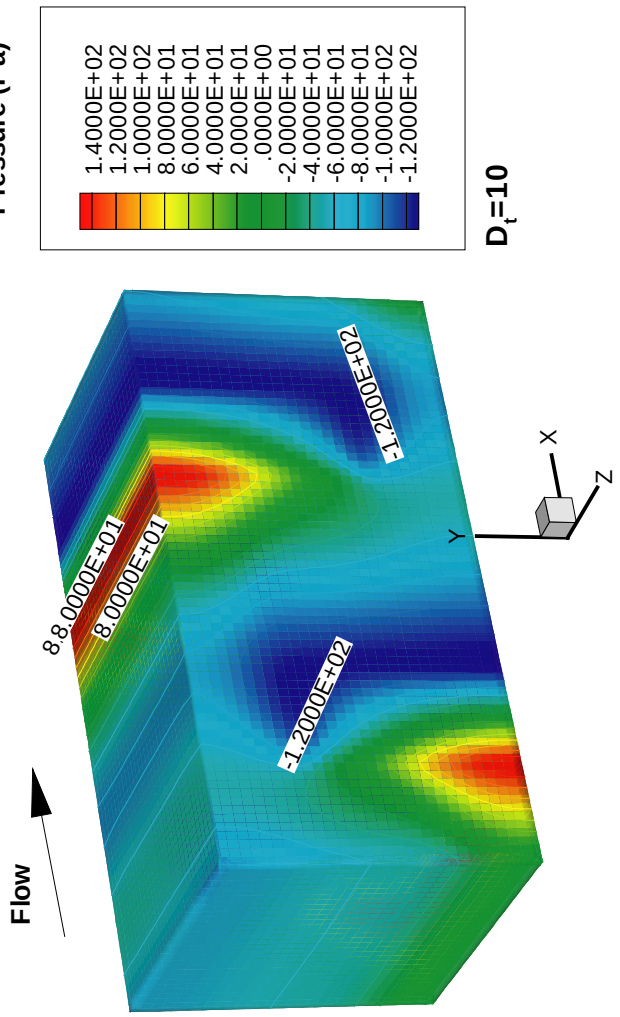

Fig. 6.24. Isobar distribution for a sample case.

6.4.4 Pressure Distribution

Fig. 6.24 shows the pressure distribution of the sample case of $B_t / D_h = 1/3$, $B_h / D_h = 2/3$, 40PPI, Re=40,000, and C=0.05 with $D_t = 10$. It is clearly seen that the lower region of the baffles are responsible for the major portion of pressure drop for this module.

6.4.5 Isotherm for Sample Case (D_t=10)

Fig. 6.25 shows the isotherms of the wall temperatures for the sample case of $B_t / D_h = 1/3$, $B_h / D_h = 2/3$, 40PPI, Re=40,000, and C=0.05 with $D_t = 10$. The top and bottom wall showed the lowest temperature due to the injection of the flow on the wall, but the left and right region around the tip of the porous baffles and the root of the baffles showed higher temperature due to the reduced speed. The root has higher temperature due to the velocity of flow becoming zero at the wall. The middle portion has higher temperature because it is in the middle of curved flow and the relatively higher speed flow, which has passed the porous media with a channeling effect.

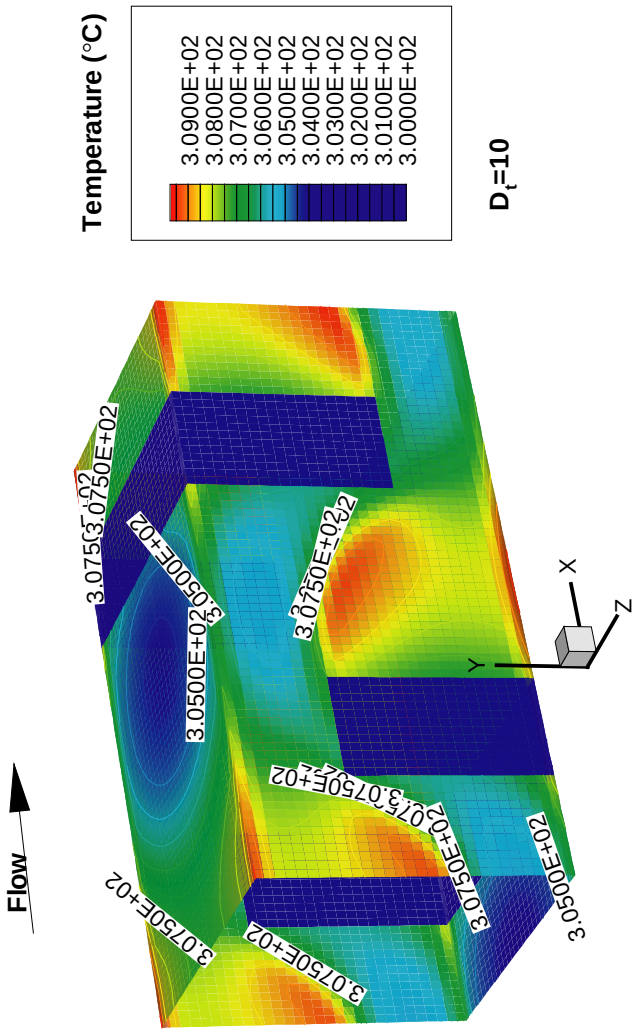

Fig. 6.25. Isotherm distribution for a sample case.

6.4.6 Local Heat Transfer Distribution

Fig. 6.26 shows the local heat transfer distribution for the case of $B_t / D_h = 1/3$, $B_h / D_h = 2/3$, 40PPI, Re=40,000, and C=0.05 with $D_t = 10$. In this study, the mean temperature was calculated using the energy balance, and it is fixed for a module at a constant velocity. For a local region, such as porous zone, the local heat transfer coefficients can be very high. To focus more on the variation of heat transfer posterior of the baffles, the local heat transfer is scaled on the wall region only.

Again, due to the injecting flow, the top portion of the module has a higher heat transfer coefficient of 70~80 $W / m^2 °C$, but the posterior region of the baffle has lowest heat transfer coefficient of 40~50 $W / m^2 °C$, due to the lower flow velocity. The central area posterior to the baffles has a relatively higher heat transfer coefficient (64~52 $W / m^2 °C$) compared to the other area (42~48 $W / m^2 °C$).

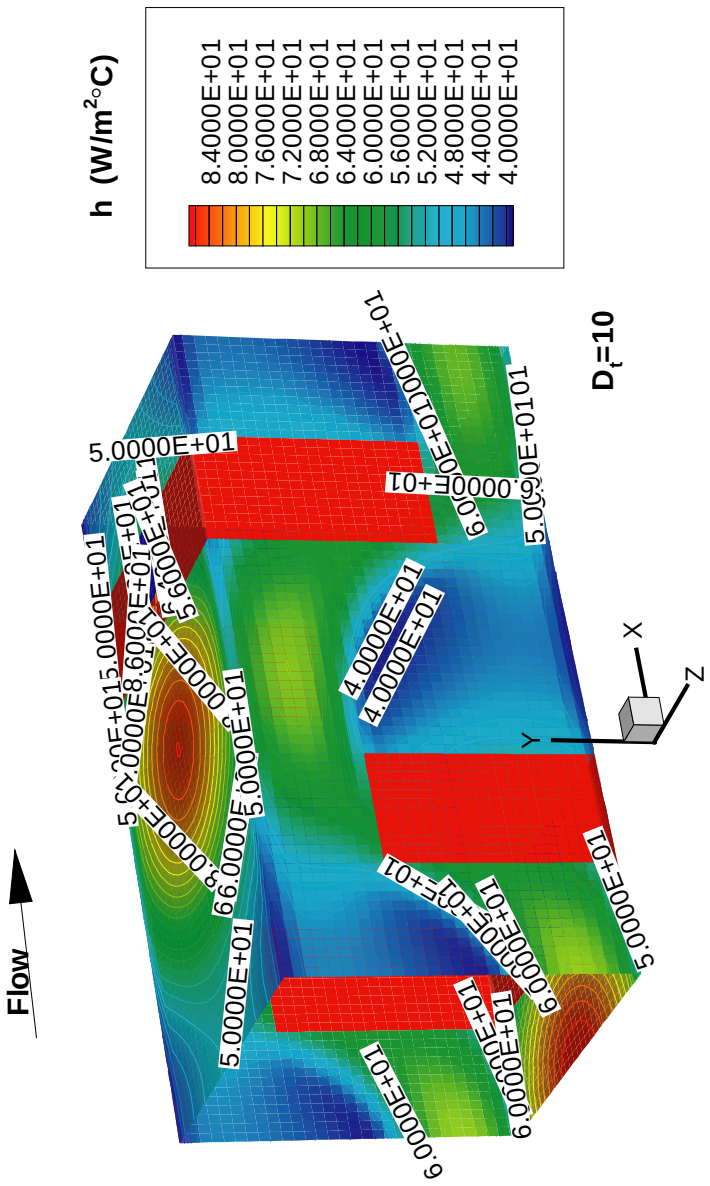

Fig. 6.26. Local heat transfer coefficients for a sample case.

CHAPTER VII

CONCLUSIONS

The module averaged heat transfer coefficients for the turbulent convective flow with porous baffles attached to the wall in a three dimensional channel were obtained through experiments. A numerical procedure was implemented in conjunction with a commercially available Navier-Stokes solver to model the turbulent flow in porous media with three types of modified energy equation models.

It was found that the heat transfer performance was increased by 300% by using porous baffles compared to that of straight channel. For a high porosity metal foam, the heat transfer enhancement was not significantly improved compared to the solid baffles under the equal pumping power condition.

The conventional model showed a maximum error of 33% in the range of Re=20,000~40,000. The one-equation model, which consisted of the effective conductivity and the dispersion conductivity, showed about 5-10% improvement over the conventional model. However, the heat transfer was not predicted well, even with the highest value of dispersion conductivity. This is due to the flow velocity range for this study was very high. The conventional model has nearly the same level of total effective conductivity compared to the one-equation model. However, the conventional model may over-predict at lower velocities due to the lack of considering the thermal resistance effects.

The two-equation model, which is based on local thermal non-equilibrium theory, was used to solve solid phase and fluid phase energy equations independently. The two-equation model showed little or no improvement over the one-equation model, but it was found that the heat transfer mechanism can be explained by complementary effects of both the dispersion conductivity and two-phase energy transfer.

The relative error for Nusselt number in turbulent convective flow was obtained within 30% of the experimental data. When the velocity of the flow was in the moderate range ($Re < 20,000$) the error decreased significantly.

For further study, rigorous turbulence modeling in conjunction with the microscopic geometric information of foam material near the wall may be required to improve the overall prediction for the turbulent flow in the porous media.

REFERENCES

[1] Choi, J. M. and Anand, N. K., Heat-Transfer in a Serpentine Channel with a Series of Right-Angle Turns, Numerical Heat Transfer Part A-Applications 23 (1993) 189-210.

[2] Choi, J. M., Anand, N. K., Lau, S. C., and Kukreja, R. T., Heat (Mass) Transfer in a Serpentine Channel with Right-Angled Turns, Journal of Heat Transfer-Transactions of the ASME 118 (1996) 211-213.

[3] Berner, C., Durst, F., and Mceligot, D. M., Flow Around Baffles, Journal of Heat Transfer-Transactions of the ASME 106 (1984) 743-749.

[4] Kim, S. H. and Anand, N. K., Turbulent Heat-Transfer Between a Series of Parallel Plates with Surface-Mounted Discrete Heat-Sources, Journal of Heat Transfer-Transactions of the ASME 116 (1994) 577-587.

[5] Hwang, J. J., Turbulent Heat Transfer and Fluid Flow in a Porous-Baffled Channel, Journal of Thermophysics and Heat Transfer 11 (1997) 429-436.

[6] Ko, K. H. and Anand, N. K., Use of Porous Baffles to Enhance Heat Transfer in a Rectangular Channel, International Journal of Heat and Mass Transfer 46 (2003) 4191-4199.

[7] Koh, J. C. Y. and Stevens, R. L., Enhancement of Cooling Effectiveness by Porous Materials in Coolant Passage, Journal of Heat Transfer-Transactions of the ASME 97 (1975) 309-311.

[8] Megerlin, F. E., Murphy, R. W., and Bergles, A. E., Augmentation of Heat-Transfer in Tubes by Use of Mesh and Brush Inserts, Journal of Heat Transfer-Transactions of the ASME 96 (1974) 145-151.

[9] Kuo, S. M. and Tien, C. L., Heat Transfer Augmentation in a Foam-Material Filled Duct With Discrete Heat Sources, Thermal Phenomena in the Fabrication and Operation of Electronic Components: I-THERM '88, Inter-Society Conference, Los Angeles, California, 1988, pp. 87-91.

[10] Rachedi, R. and Chikh, S., Enhancement of Electronic Cooling by Insertion of Foam Materials, Heat and Mass Transfer 37 (2001) 371-378.

[11] Hwang, G. J. and Chao, C. H., Heat-Transfer Measurement and Analysis for Sintered Porous Channels, Journal of Heat Transfer-Transactions of the ASME 116 (1994) 456-464.

[12] Kim, S. Y., Kang, B. H., and Kim, J. H., Forced Convection from Aluminum Foam Materials in an Asymmetrically Heated Channel, International Journal of Heat and Mass Transfer 44 (2001) 1451-1454.

[13] Hwang, J. J. and Liou, T. M., Augmented Heat-Transfer in a Rectangular Channel with Permeable Ribs Mounted on the Wall, Journal of Heat Transfer-Transactions of the ASME 116 (1994) 912-920.

[14] Liou, T. M. and Chen, S. H., Turbulent Heat and Fluid Flow in a Passage Disturbed by Detached Perforated Ribs of Different Heights, International Journal of Heat and Mass Transfer 41 (1998) 1795-1806.

[15] Bear, J., Dynamics of Fluids in Porous Media, American Elsevier Pub. Co., New York, 1972.

[16] Kaviany, M., Principles of Heat Transfer in Porous Media, Springer-Verlag, New York, 1995.

[17] Nakayama, A., PC-aided Numerical Heat Transfer and Convective Flow, CRC Press, Boca Raton, 1995.

[18] Nield, D. A. and Bejan, A., Convection in Porous Media, Springer-Verlag, New York, 1992.

[19] Wooding, R. A., Steady State Free Thermal Convection of Liquid in a Saturated Permeable Medium, Journal of Fluid Mechanics 2 (1957) 273-285.

[20] Vafai, K. and Tien, C. L., Boundary and Inertia Effects on Flow and Heat-Transfer in Porous-Media, International Journal of Heat and Mass Transfer 24 (1981) 195-203.

[21] Slattery, J. C., Flow of Viscoelastic Fluids Through Porous Media, AIChE J. 13 (1967) 1066-1071.

[22] Slattery, J. C., Multiphase Viscoelastic Flow Through Porous Media, AIChE J. 14 (1968) 50-56.

[23] Hunt, M. L. and Tien, C. L., Non-Darcian Convection in Cylindrical Packed-Beds, Journal of Heat Transfer-Transactions of the ASME 110 (1988) 378-384.

[24] Hunt, M. L. and Tien, C. L., Effects of Thermal Dispersion on Forced-Convection in Fibrous Media, International Journal of Heat and Mass Transfer 31 (1988) 301-309.

[25] Hsiao, S. W., Cheng, P., and Chen, C. K., Nonuniform Porosity and Thermal Dispersion Effects on Natural-Convection About a Heated Horizontal Cylinder in

an Enclosed Porous-Medium, International Journal of Heat and Mass Transfer 35 (1992) 3407-3418.

[26] Hsu, C. T. and Cheng, P., Thermal Dispersion in a Porous-Medium, International Journal of Heat and Mass Transfer 33 (1990) 1587-1597.

[27] Kuznetsov, A. V., Cheng, L., and Xiong, M., Effects of Thermal Dispersion and Turbulence in Forced Convection in a Composite Parallel-Plate Channel: Investigation of Constant Wall Heat Flux and Constant Wall Temperature Cases, Numerical Heat Transfer Part A-Applications 42 (2002) 365-383.

[28] Cheng, P. and Vortmeyer, D., Transverse Thermal Dispersion and Wall Channeling in a Packed-Bed with Forced Convective Flow, Chemical Engineering Science 43 (1988) 2523-2532.

[29] Dixon, A. G. and Cresswell, D. L., Theoretical Prediction of Effective Heat-Transfer Parameters in Packed-Beds, AIChE J. 25 (1979) 663-676.

[30] Achenbach, E., Heat and Flow Characteristics of Packed-Beds, Experimental Thermal and Fluid Science 10 (1995) 17-27.

[31] Kuznetsov, A. V., Analysis of Heating a Three-Dimensional Porous Bed Utilizing the Two Energy Equation Model, Heat and Mass Transfer 31 (1996) 173-177.

[32] Maxwell, J. C., A Treatise on Electricity and Magnetism, Vol. 1, Claredon Press, Oxford 1873, pp. 365.

[33] Hadley, G. R., Thermal-Conductivity of Packed Metal Powders, International Journal of Heat and Mass Transfer 29 (1986) 909-920.

[34] Chiew, Y. C. and Glandt, E. D., The Effect of Structure on the Conductivity of a Dispersion, Journal of Colloid and Interface Science 94 (1983) 90-104.

[35] Gonzo, E. E., Estimating Correlations for the Effective Thermal Conductivity of Granular Materials, Chemical Engineering Journal 90 (2002) 299-302.

[36] Boomsma, K. and Poulikakos, D., On the Effective Thermal Conductivity of a Three-Dimensionally Structured Fluid-Saturated Metal Foam, International Journal of Heat and Mass Transfer 44 (2001) 827-836.

[37] Koch, D. L. and Brady, J. L., The Effective Diffusivity of Fibrous Media, AIChE J. 32 (1986) 575-591.

[38] Angirasa, D., Forced Convective Heat Transfer in Metallic Fibrous Materials, Journal of Heat Transfer-Transactions of the ASME 124 (2002) 739-745.

[39] Fu, W. S. and Huang, H. C., Thermal Performances of Different Shape Porous Blocks Under an Impinging Jet, International Journal of Heat and Mass Transfer 40 (1997) 2261-2272.

[40] Hashimoto, K., Muroyama, K., Fujiyoshi, K., and Nagata, S., Effective Radial Thermal-Conductivity in Cocurrent Flow of a Gas and Liquid Through a Packed-Bed, International Chemical Engineering 16 (1976) 720-727.

[41] Crine, M., Heat-Transfer Phenomena in Trickle-Bed Reactors, Chemical Engineering Communications 19 (1982) 99-114.

[42] Saez, A. E., Carbonell, R. G., and Levec, J., The Hydrodynamics of Trickling Flow in Packed-Beds .1. Conduit Models, AIChE J. 32 (1986) 353-368.

[43] Vafai, K., Convective Flow and Heat-Transfer in Variable-Porosity Media, Journal of Fluid Mechanics 147 (1984) 233-259.

[44] Bachmat, Y. and Bear, J., Macroscopic Modeling of Transport Phenomena in Porous-Media .1. The Continuum Approach, Transport in Porous Media 1 (1986) 213-240.

[45] Whitaker, S., Diffusion and Dispersion in Porous Media, AIChE J. 13 (1967) 420-438.

[46] Wakao, N. and Funazkri, T., Effect of Fluid Dispersion Coefficients on Particle-To-Fluid Mass-Transfer Coefficients in Packed-Beds - Correlation of Sherwood Numbers, Chemical Engineering Science 33 (1978) 1375-1384.

[47] Amiri, A. and Vafai, K., Analysis of Dispersion Effects and Nonthermal Equilibrium, Non-Darcian, Variable Porosity Incompressible-Flow Through Porous-Media, International Journal of Heat and Mass Transfer 37 (1994) 939-954.

[48] Fourie, J. G. and Du Plessis, J. P., A Two-Equation Model for Heat Conduction in Porous Media (I: Theory), Transport in Porous Media 53 (2003) 145-161.

[49] International Organization for Standardization., Measurement of Fluid Flow by Means of Pressure Differential Devices. Part 1, Orifice Plates, Nozzles and Venturi Tubes Inserted in Circular Cross-Section Conduits, International Organization for Standardization, Geneve, Switzerland, 1991.

[50] Kline, S. J. and McClintock, F. A., Describing Uncertainties in Single-Sample Experiments, Mechanical Engineering 75 (1953) 3-8.

[51] National Conference of Standards Laboratories and American National Standards Institute, American National Standard for Expressing Uncertainty: U.S. Guide to the Expression of Uncertainty in Measurement, Reprinted -- Feb. 16, 1998. ed., National Conference of Standards Laboratories Boulder, CO: 1998, pp. 9-22.

[52] Gnielinski, V., New Equations for Heat and Mass-Transfer in Turbulent Pipe and Channel Flow, International Chemical Engineering 16 (1976) 359-368.

[53] Dittus, F. W. and Boelter, L. M. K., Heat Transfer in Automobile Radiators of the Tubular Type, Univ. of California Publications in Engineering 2 (1930) 443-461.

[54] Patankar, S. V., Liu, C. H., and Sparrow, E. M., Fully Developed Flow and Heat-Transfer in Ducts Having Streamwise-Periodic Variations of Cross-Sectional Area, Journal of Heat Transfer-Transactions of the ASME 99 (1977) 180-186.

[55] FLUENT Inc., FLUENT User Manual (Ver. 6.1), FLUENT Inc., New Hampshire, 2003.

[56] Launder, B. E. and Spalding, D. B., The Numerical Computation of Turbulent Flows, Computer Methods in Applied Mechanics and Engineering 3 (1974) 269-289.

[57] Kim, S.-E. and Choudhury, D., A Near-Wall Treatment Using Wall Functions Sensitized to Pressure Gradient, in: ASME FED Vol.217, Separated and Complex Flows, ASME, 1995.

[58] Sahraoui, M. and Kaviany, M., Slip and No-Slip Temperature Boundary-Conditions at Interface of Porous, Plain Media - Conduction, International Journal of Heat and Mass Transfer 36 (1993) 1019-1033.

[59] Amiri, A., Vafai, K., and Kuzay, T. M., Effects of Boundary-Conditions on Non-Darcian Heat-Transfer Through Porous-Media and Experimental Comparisons, Numerical Heat Transfer Part A-Applications 27 (1995) 651-664.

[60] Kim, S. J. and Kim, D., Thermal interaction at the interface between a porous medium and an impermeable wall, Journal of Heat Transfer-Transactions of the ASME 123 (2001) 527-533.

[61] Mauran, S., Rigaud, L., and Coudevylle, O., Application of the Carman-Kozeny Correlation to a High-Porosity and Anisotropic Consolidated Medium: The Compressed Expanded Natural Graphite, Transport in Porous Media 43 (2001) 355-376.

APPENDIX A

UNCERTAINTY ANALYSIS

Sample Calculation of Uncertainty ($Re = 40,000$, $40PPI$, $B_t / D_h = 1/3$, and $B_h / D_h = 2/3$ **)**

The experimental uncertainties of the test results of the current study were analyzed using the methods proposed by Kline and McClintock [50] and the ANSI Guide to the Expression of Uncertainty in Measurement [51].

The variables measured were temperature, pressure drop, and heat applied to each module. The uncertainty associated with each variable is the square root sum of the squares of precision and bias errors. The bias error was found to be negligibly small compared to the precision errors, accordingly the bias errors associated with each variable was neglected.

Uncertainty of a function which has dependent variables of the form such as equation (A.1) can be expressed as equation (A.2).

$$y = f(x_1, x_2, x_3, \cdots, x_N) \tag{A.1}$$

$$u_c^2(y) = \sum_{i=1}^{N} \left(\frac{\partial f}{\partial x_i} \right)^2 u^2(x_i) \tag{A.2}$$

where, $u_c(y)$ denotes combined standard uncertainty and $u(y)$ denotes standard uncertainty

Uncertainty of Density (ρ)

Density is a function of temperature and pressure as,

$$\rho = \frac{P}{\mathbb{R}T} \tag{A.3}$$

Using equation (A.2), the uncertainty of density can be expressed as,

$$\begin{aligned}
\left(\frac{u(\rho)}{\rho}\right)^2 &= \left(\frac{1}{\rho}\right)^2 \left(\frac{\partial f}{\partial x_i}\, u(x_i)\right)^2 \\
&= \left(\frac{1}{\rho}\right)^2 \left[\left(\frac{\partial f}{\partial p}\, u(p)\right)^2 + \left(\frac{\partial f}{\partial T}\, u(T)\right)^2\right] \\
&= \left[\left(\frac{1}{\mathbb{R}T}\,\frac{u(P)}{\frac{P}{\mathbb{R}T}}\right)^2 + \left(-\frac{P}{\mathbb{R}}\,T^{-2}\,\frac{u(T)}{\frac{P}{\mathbb{R}T}}\right)^2\right] \\
&= \left[\left(\frac{u(P)}{P}\right)^2 + \left(\frac{u(T)}{T}\right)^2\right]
\end{aligned} \tag{A.4}$$

Maximum deviation of pressure is $24.90660025\, N/m^2$ from multiple sampling and instrument calibration data. Maximum temperature deviation is estimated with $1C°$. Substituting equation (A.3) into (A.2) yields equation (A.4). Now inserting the relevant values from above yields an uncertainty of 0.32%

Uncertainty of Mass Flow Rate ($\dot{m}$)

Mass flow rate is calculated using,

$$\dot{m} = \frac{\pi}{4} d^2 C_d \left(\frac{2\Delta P}{\rho(1-\beta^4)} \right)^{0.6} \tag{A.5}$$

Considering reported maximum uncertainty of 0.6% for discharge coefficient C_d , Using equation (A.2) again, the uncertainty mass flow rate is expressed as,

$$\begin{aligned} \left(\frac{u(\dot{m})}{\dot{m}} \right)^2 &= \left[\left(\frac{u(\rho)}{\rho} \right)^2 + \frac{\partial(\Delta P)}{\partial P} \left(\frac{u(P)}{\Delta P} \right)^2 + \left(\frac{u(C_d)}{C_d} \right)^2 \right] \\ &= \left[\left(\frac{u(\rho)}{\rho} \right)^2 + 2 \left(\frac{u(P)}{\Delta P} \right)^2 + \left(\frac{u(C_d)}{C_d} \right)^2 \right] \end{aligned} \tag{A.6}$$

Inserting the relevant values from above yields an uncertainty of 1.73%

Uncertainty of Total Heat Flux (Q)

Total heat flux is calculated from direct electric current and voltage meters, which have factory calibration uncertainty of 2.5% and 2% respectively.

$$Q = IV \tag{A.7}$$

$$\left(\frac{u(Q)}{Q} \right)^2 = \left[\left(\frac{u(I)}{I} \right)^2 + \left(\frac{u(V)}{V} \right)^2 \right] \tag{A.8}$$

Thus the maximum uncertainty of total heat flux is 3.2%.

Uncertainty of Heat Transfer Coefficient (h_m)

Since the averaged heat transfer coefficient for the module can be expressed as equation (A.9) (The dependent variables are ordered its importance)

$$\bar{h}_m = f(\dot{m}, T_{wall}, T_{in}, Q_{total}, q_{m,loss}, C_p) \tag{A.9}$$

To determine the sensitive coefficients from equation (A.2), taking partial derivatives of each independent variables of equation (A.9),

$$\frac{\partial f}{\partial x_1} = \frac{\partial y}{\partial \dot{m}} = \left(\frac{1}{A_m}\right) \frac{(q_m - q_{m,loss})^2 (i-1/2)}{\left[T_{wall} - \left(T_{in} + \frac{q_m - q_{m,loss}}{\dot{m} C_p} \cdot (i-1/2)\right)\right]^2 \dot{m}^2 C_p}$$

$$\frac{\partial f}{\partial x_2} = \frac{\partial y}{\partial q} = \left(\frac{1}{A_m}\right) \left\{ \frac{1}{T_{wall} - \left(T_{in} + \frac{q_m - q_{m,loss}}{\dot{m} C_p} \cdot (i-1/2)\right)} - \frac{(q_m - q_{m,loss})(i-1/2)}{\left[T_{wall} - \left(T_{in} + \frac{q_m - q_{m,loss}}{\dot{m} C_p} \cdot (i-1/2)\right)\right]^2 \dot{m} C_p} \right\}$$

$$\frac{\partial f}{\partial x_3} = \frac{\partial y}{\partial T_{in}} = \left(\frac{1}{A_m}\right) \left\{ \frac{-\left(q_m - q_{m,loss}\right)}{\left[T_{wall} - \left(T_{in} + \frac{q_m - q_{m,loss}}{\dot{m} C_p} \cdot (i-1/2)\right)\right]^2} \right\}$$

$$\frac{\partial f}{\partial x_4} = \frac{\partial y}{\partial T_{wall}} = \left(\frac{1}{A_m}\right) \left\{ \frac{\left(q_m - q_{m,loss}\right)}{\left[T_{wall} - \left(T_{in} + \frac{q_m - q_{m,loss}}{\dot{m} C_p} \cdot (i-1/2)\right)\right]^2} \right\} \tag{A.10}$$

To simplify equation (A.10), substitute complex terms with new variables,

$$\begin{aligned}
\frac{\partial f}{\partial x_1} &= \frac{\partial y}{\partial \dot{m}} = \left(\frac{1}{A_m}\right)\frac{{C_q}^2 C_{mi}}{{C_T}^2 \dot{m}} \\
\frac{\partial f}{\partial x_2} &= \frac{\partial y}{\partial q} = \left(\frac{1}{A_m}\right)\left(\frac{1}{C_T} - \frac{C_q C_{mi}}{{C_T}^2}\right) \\
\frac{\partial f}{\partial x_3} &= \frac{\partial y}{\partial T_{in}} = \left(\frac{1}{A_m}\right)\frac{-C_q}{{C_T}^2} \\
\frac{\partial f}{\partial x_4} &= \frac{\partial y}{\partial T_{wall}} = \left(\frac{1}{A_m}\right)\frac{C_q}{{C_T}^2}
\end{aligned} \qquad \textit{(A.11)}$$

where

$$\begin{aligned}
C_q &= (q_m - q_{m,loss}) \\
C_T &= \left[T_{wall} - \left(T_{in} + \frac{q_m - q_{m,loss}}{\dot{m} C_p} \cdot (i - 1/2)\right)\right] \\
C_{mi} &= \frac{i - 1/2}{\dot{m} C_p}
\end{aligned} \qquad \textit{(A.12)}$$

Final equation form is,

$$\begin{aligned}
\left(\frac{u(\overline{h_m})}{\overline{h_m}}\right)^2 &= \left(\frac{1}{\overline{h_m}}\right)^2 \left(\frac{\partial f}{\partial x_i} u(x_i)\right)^2 \\
&= \left(\frac{1}{\overline{h_m}}\right)^2 \left[\begin{array}{l} \left(\frac{\partial f}{\partial \dot{m}} u(\dot{m})\right)^2 + \left(\frac{\partial f}{\partial q} u(q)\right)^2 + \left(\frac{\partial f}{\partial T_{in}} u(T_{in})\right)^2 \\ + \left(\frac{\partial f}{\partial T_{wall}} u(T_{wall})\right)^2 \end{array}\right] \\
&= \left(\frac{1}{A_m}\right)^2 \left\{\begin{array}{l} \left(\frac{{C_q}^2 C_{mi}}{{C_T}^2 \dot{m}}\right)^2 \left(\frac{u(\dot{m})}{\overline{h_m}}\right)^2 + \left(\frac{1}{C_T} - \frac{C_q C_{mi}}{{C_T}^2}\right)^2 \left(\frac{u(q)}{\overline{h_m}}\right)^2 \\ + \left(-\frac{C_q}{{C_T}^2}\right)^2 \left(\frac{u(T_{in})}{\overline{h_m}}\right)^2 + \left(\frac{C_q}{{C_T}^2}\right)^2 \left(\frac{u(T_{wall})}{\overline{h_m}}\right)^2 \end{array}\right\}
\end{aligned} \qquad \textit{(A.13)}$$

Again inserting relevant data to equation (A.13) yields maximum uncertainty of 5.6%.

APPENDIX B

MESH GENERATION SCRIPT

```
/ Script written by Kang-Hoon Ko
/ Department of Mechanical Engineering
/ Texas A&M University
/
/           |y
/           |
/           |-----
/           |    | y1
/           ------------ --->z
/             z1
/

/ input $x2 -> thickness of porous block
/ input $y1 -> height of porous block
/ input $z1 -> width of porous block
/ input $blayer -> length of boundary layer (y+)
/ input $ph  -> block selection for porous zone (1 or 2)
solver select "FLUENT 5/6"

$blayer = 0.08
$n_mesh_z = 10
$n_mesh_y = 10
$n_mesh_x1 =15
$n_mesh_x2 =6

/porous block height & thickness
$ph = 2.5
$pt = 1.5

/first box size
$x2=$pt
if cond ($ph .le. 1.5) then
        $y=$ph
endif
if cond ($ph .gt. 1.5) then
        $y=3-$ph
endif
```

```
$z1=1

/box1
$x1=(3-$x2)/2
$xinc=0
$xc=$x1
$xco=$xc/2+$xinc
$y1o=$y1/2
$z1o=$z1/2

volume create "base1" width $xc depth $y1 height $z1 offset $xco $y1o $z1o brick
$y2=3-$y1*2
$y2o=$y2/2+$y1
$z2=3-$z1*2
$z2o=$z2/2+$z1
volume cmove "base1" multiple 1 offset 0 (3-$y1) 0
volume cmove "base1" multiple 1 offset 0 (3-$y1) (3-$z1)
volume cmove "base1" multiple 1 offset 0       0 (3-$z1)

if cond ($y2 .gt. 0)
        volume create "up1" width $xc depth $y2 height $z1 offset $xco $y2o $z1o brick
        volume cmove "up1" multiple 1 offset 0    0 (3-$z1)
endif

if cond ($z2 .gt. 0)
        volume create "right1" width $xc depth $y1 height $z2 offset $xco $y1o $z2o
brick
        volume cmove "right1" multiple 1 offset 0 (3-$y1) 0
endif

if cond (($y2 .gt. 0).and.($z2 .gt 0))
        volume create "center1" width $xc depth $y2 height $z2 offset $xco 1.5 1.5 brick
endif

/box2
$xinc=$x1
$xc=$x2
$xco=$xc/2+$xinc
$y1o=$y1/2
$z1o=$z1/2

volume create "base2" width $xc depth $y1 height $z1 offset $xco $y1o $z1o brick
$y2=3-$y1*2
$y2o=$y2/2+$y1
```

```
$z2=3-$z1*2
$z2o=$z2/2+$z1
volume cmove "base2" multiple 1 offset 0 (3-$y1) 0
volume cmove "base2" multiple 1 offset 0 (3-$y1) (3-$z1)
volume cmove "base2" multiple 1 offset 0       0 (3-$z1)
if cond ($y2 .gt. 0)
        volume create "up2" width $xc depth $y2 height $z1 offset $xco $y2o $z1o brick
        volume cmove "up2" multiple 1 offset 0       0 (3-$z1)
endif
if cond ($z2 .gt. 0)
        volume create "right2" width $xc depth $y1 height $z2 offset $xco $y1o $z2o
brick
        volume cmove "right2" multiple 1 offset 0 (3-$y1) 0
endif
if cond (($y2 .gt. 0).and.($z2 .gt 0))
        volume create "center2" width $xc depth $y2 height $z2 offset $xco 1.5 1.5 brick
endif


/box3
$xinc=$x1+$x2
$xc=$x1
$xco=$xc/2+$xinc
$y1o=$y1/2
$z1o=$z1/2

volume create "base3" width $xc depth $y1 height $z1 offset $xco $y1o $z1o brick
$y2=3-$y1*2
$y2o=$y2/2+$y1
$z2=3-$z1*2
$z2o=$z2/2+$z1
volume cmove "base3" multiple 1 offset 0 (3-$y1) 0
volume cmove "base3" multiple 1 offset 0 (3-$y1) (3-$z1)
volume cmove "base3" multiple 1 offset 0       0 (3-$z1)
if cond ($y2 .gt. 0)
        volume create "up3" width $xc depth $y2 height $z1 offset $xco $y2o $z1o brick
        volume cmove "up3" multiple 1 offset 0       0 (3-$z1)
endif
if cond ($z2 .gt. 0)
        volume create "right3" width $xc depth $y1 height $z2 offset $xco $y1o $z2o
brick
        volume cmove "right3" multiple 1 offset 0 (3-$y1) 0
endif
if cond (($y2 .gt. 0).and.($z2 .gt 0))
```

```
        volume create "center3" width $xc depth $y2 height $z2 offset $xco 1.5 1.5 brick
endif

/box4
$xinc=$x1+$x2+$x1
$xc=$x1
$xco=$xc/2+$xinc
$y1o=$y1/2
$z1o=$z1/2

volume create "base4" width $xc depth $y1 height $z1 offset $xco $y1o $z1o brick
$y2=3-$y1*2
$y2o=$y2/2+$y1
$z2=3-$z1*2
$z2o=$z2/2+$z1
volume cmove "base4" multiple 1 offset 0 (3-$y1) 0
volume cmove "base4" multiple 1 offset 0 (3-$y1) (3-$z1)
volume cmove "base4" multiple 1 offset 0       0 (3-$z1)
if cond ($y2 .gt. 0)
        volume create "up4" width $xc depth $y2 height $z1 offset $xco $y2o $z1o brick
        volume cmove "up4" multiple 1 offset 0       0 (3-$z1)
endif
if cond ($z2 .gt. 0)
        volume create "right4" width $xc depth $y1 height $z2 offset $xco $y1o $z2o
brick
        volume cmove "right4" multiple 1 offset 0 (3-$y1) 0
endif
if cond (($y2 .gt. 0).and.($z2 .gt 0))
        volume create "center4" width $xc depth $y2 height $z2 offset $xco 1.5 1.5 brick
endif

/box5
$xinc=$x1+$x2+$x1+$x1
$xc=$x2
$xco=$xc/2+$xinc
$y1o=$y1/2
$z1o=$z1/2

volume create "base5" width $xc depth $y1 height $z1 offset $xco $y1o $z1o brick
$y2=3-$y1*2
$y2o=$y2/2+$y1
$z2=3-$z1*2
$z2o=$z2/2+$z1
volume cmove "base5" multiple 1 offset 0 (3-$y1) 0
```

```
volume cmove "base5" multiple 1 offset 0 (3-$y1) (3-$z1)
volume cmove "base5" multiple 1 offset 0       0 (3-$z1)
if cond ($y2 .gt. 0)
        volume create "up5" width $xc depth $y2 height $z1 offset $xco $y2o $z1o brick
        volume cmove "up5" multiple 1 offset 0       0 (3-$z1)
endif
if cond ($z2 .gt. 0)
        volume create "right5" width $xc depth $y1 height $z2 offset $xco $y1o $z2o
brick
        volume cmove "right5" multiple 1 offset 0 (3-$y1) 0
endif
if cond (($y2 .gt. 0).and.($z2 .gt 0))
        volume create "center5" width $xc depth $y2 height $z2 offset $xco 1.5 1.5 brick
endif

/box6
$xinc=$x1+$x2+$x1+$x1+$x2
$xc=$x1
$xco=$xc/2+$xinc
$y1o=$y1/2
$z1o=$z1/2

volume create "base6" width $xc depth $y1 height $z1 offset $xco $y1o $z1o brick
$y2=3-$y1*2
$y2o=$y2/2+$y1
$z2=3-$z1*2
$z2o=$z2/2+$z1
volume cmove "base6" multiple 1 offset 0 (3-$y1) 0
volume cmove "base6" multiple 1 offset 0 (3-$y1) (3-$z1)
volume cmove "base6" multiple 1 offset 0       0 (3-$z1)
if cond ($y2 .gt. 0)
        volume create "up6" width $xc depth $y2 height $z1 offset $xco $y2o $z1o brick
        volume cmove "up6" multiple 1 offset 0       0 (3-$z1)
endif
if cond ($z2 .gt. 0)
        volume create "right6" width $xc depth $y1 height $z2 offset $xco $y1o $z2o
brick
        volume cmove "right6" multiple 1 offset 0 (3-$y1) 0
endif
if cond (($y2 .gt. 0).and.($z2 .gt 0))
        volume create "center6" width $xc depth $y2 height $z2 offset $xco 1.5 1.5 brick
endif

/connect faces
```

```
face connect real

/link periodic mesh
face link "face.16" "face.288" edges "edge.35" "edge.565" vertices \
  "vertex.19" "vertex.378" reverse periodic
face link "face.46" "face.318" edges "edge.95" "edge.569" vertices \
  "vertex.24" "vertex.381" reverse periodic
face link "face.10" "face.282" edges "edge.23" "edge.553" vertices \
  "vertex.11" "vertex.370" reverse periodic
face link "face.34" "face.306" edges "edge.33" "edge.601" vertices \
  "vertex.20" "vertex.377" reverse periodic
face link "face.51" "face.322" edges "edge.93" "edge.605" vertices \
  "vertex.23" "vertex.382" reverse periodic
face link "face.27" "face.298" edges "edge.21" "edge.599" vertices \
  "vertex.12" "vertex.369" reverse periodic
face link "face.22" "face.294" edges "edge.47" "edge.577" vertices \
  "vertex.27" "vertex.386" reverse periodic
face link "face.39" "face.310" edges "edge.79" "edge.581" vertices \
  "vertex.32" "vertex.389" reverse periodic
face link "face.3" "face.274" edges "edge.7" "edge.551" vertices "vertex.7" \
  "vertex.368" reverse periodic

/bounday layer
undo begingroup
blayer create "bounday" first $blayer growth 1 total $blayer rows 1 transition 1 \
  trows 0
blayer attach "bounday" volume "base1" "volume.2" "up1" "base2" "base2" \
  "volume.11" "volume.11" "up2" "base3" "base3" "volume.20" "volume.20" "up3" \
  "base4" "base4" "volume.29" "volume.29" "up4" "volume.38" "volume.38" \
  "volume.39" "volume.39" "volume.44" "base6" "base6" "volume.47" "volume.47" \
  "up6" "volume.3" "volume.3" "volume.4" "volume.4" "volume.6" "volume.12" \
  "volume.12" "volume.13" "volume.13" "volume.15" "volume.21" "volume.21" \
  "volume.22" "volume.22" "volume.24" "volume.30" "volume.30" "volume.31" \
  "volume.31" "volume.33" "volume.42" "volume.40" "volume.40" "volume.48" \
  "volume.48" "volume.49" "volume.49" "volume.51" "volume.8" "volume.17" \
  "volume.26" "volume.35" "volume.53" "right1" "right2" "right3" "right4" \
  "right5" "right6" face "face.1" "face.8" "face.25" "face.55" "face.56" \
  "face.62" "face.65" "face.79" "face.109" "face.110" "face.116" "face.119" \
  "face.133" "face.163" "face.164" "face.170" "face.173" "face.187" \
  "face.224" "face.227" "face.229" "face.233" "face.263" "face.271" \
  "face.272" "face.278" "face.281" "face.295" "face.13" "face.17" "face.19" \
  "face.21" "face.31" "face.67" "face.71" "face.73" "face.75" "face.85" \
  "face.121" "face.125" "face.127" "face.129" "face.139" "face.175" \
  "face.179" "face.181" "face.183" "face.193" "face.247" "face.235" \
```

```
  "face.237" "face.283" "face.287" "face.289" "face.291" "face.301" "face.47" \
  "face.101" "face.155" "face.209" "face.317" "face.38" "face.92" "face.146" \
  "face.200" "face.254" "face.308"
undo endgroup

/mesh

undo begingroup
edge delete "edge.13" "edge.577" "edge.543" "edge.469" "edge.435" "edge.361" \
  "edge.327" "edge.253" "edge.219" "edge.145" "edge.111" "edge.43" "edge.37" \
  "edge.10" "edge.3" "edge.601" "edge.591" "edge.493" "edge.483" "edge.385" \
  "edge.375" "edge.277" "edge.267" "edge.169" "edge.159" "edge.67" "edge.61" \
  "edge.58" "edge.51" "edge.565" "edge.557" "edge.457" "edge.449" "edge.349" \
  "edge.341" "edge.241" "edge.233" "edge.133" "edge.125" "edge.31" "edge.25" \
  "edge.17" "edge.15" "edge.581" "edge.551" "edge.473" "edge.443" "edge.365" \
  "edge.335" "edge.257" "edge.227" "edge.149" "edge.119" "edge.41" "edge.39" \
  "edge.11" "edge.2" "edge.605" "edge.599" "edge.497" "edge.491" "edge.389" \
  "edge.383" "edge.281" "edge.275" "edge.173" "edge.167" "edge.65" "edge.63" \
  "edge.59" "edge.50" "edge.569" "edge.553" "edge.461" "edge.445" "edge.353" \
  "edge.337" "edge.245" "edge.229" "edge.137" "edge.121" "edge.29" "edge.27" \
  "edge.19" keepsettings onlymesh
edge mesh "edge.13" "edge.577" "edge.543" "edge.469" "edge.435" "edge.361" \
  "edge.327" "edge.253" "edge.219" "edge.145" "edge.111" "edge.43" "edge.37" \
  "edge.10" "edge.3" "edge.601" "edge.591" "edge.493" "edge.483" "edge.385" \
  "edge.375" "edge.277" "edge.267" "edge.169" "edge.159" "edge.67" "edge.61" \
  "edge.58" "edge.51" "edge.565" "edge.557" "edge.457" "edge.449" "edge.349" \
  "edge.341" "edge.241" "edge.233" "edge.133" "edge.125" "edge.31" "edge.25" \
  "edge.17" "edge.15" "edge.581" "edge.551" "edge.473" "edge.443" "edge.365" \
  "edge.335" "edge.257" "edge.227" "edge.149" "edge.119" "edge.41" "edge.39" \
  "edge.11" "edge.2" "edge.605" "edge.599" "edge.497" "edge.491" "edge.389" \
  "edge.383" "edge.281" "edge.275" "edge.173" "edge.167" "edge.65" "edge.63" \
  "edge.59" "edge.50" "edge.569" "edge.553" "edge.461" "edge.445" "edge.353" \
  "edge.337" "edge.245" "edge.229" "edge.137" "edge.121" "edge.29" "edge.27" \
  "edge.19" bellshape ratio1 0.5 intervals $n_mesh_z
undo endgroup
undo begingroup
edge delete "edge.33" "edge.564" "edge.562" "edge.548" "edge.546" "edge.456" \
  "edge.454" "edge.440" "edge.438" "edge.348" "edge.346" "edge.332" \
  "edge.330" "edge.240" "edge.238" "edge.224" "edge.222" "edge.132" \
  "edge.130" "edge.116" "edge.114" "edge.24" "edge.23" "edge.22" "edge.21" \
  "edge.8" "edge.7" "edge.6" "edge.5" "edge.636" "edge.634" "edge.620" \
  "edge.618" "edge.528" "edge.526" "edge.512" "edge.510" "edge.420" \
  "edge.418" "edge.404" "edge.402" "edge.312" "edge.310" "edge.296" \
  "edge.294" "edge.204" "edge.202" "edge.188" "edge.186" "edge.96" "edge.95" \
```

```
  "edge.94" "edge.93" "edge.80" "edge.79" "edge.78" "edge.77" "edge.588" \
  "edge.586" "edge.576" "edge.574" "edge.480" "edge.478" "edge.468" \
  "edge.466" "edge.372" "edge.370" "edge.360" "edge.358" "edge.264" \
  "edge.262" "edge.252" "edge.250" "edge.156" "edge.154" "edge.144" \
  "edge.142" "edge.48" "edge.47" "edge.46" "edge.45" "edge.36" "edge.35" \
  "edge.34" keepsettings onlymesh
edge mesh "edge.33" "edge.564" "edge.562" "edge.548" "edge.546" "edge.456" \
  "edge.454" "edge.440" "edge.438" "edge.348" "edge.346" "edge.332" \
  "edge.330" "edge.240" "edge.238" "edge.224" "edge.222" "edge.132" \
  "edge.130" "edge.116" "edge.114" "edge.24" "edge.23" "edge.22" "edge.21" \
  "edge.8" "edge.7" "edge.6" "edge.5" "edge.636" "edge.634" "edge.620" \
  "edge.618" "edge.528" "edge.526" "edge.512" "edge.510" "edge.420" \
  "edge.418" "edge.404" "edge.402" "edge.312" "edge.310" "edge.296" \
  "edge.294" "edge.204" "edge.202" "edge.188" "edge.186" "edge.96" "edge.95" \
  "edge.94" "edge.93" "edge.80" "edge.79" "edge.78" "edge.77" "edge.588" \
  "edge.586" "edge.576" "edge.574" "edge.480" "edge.478" "edge.468" \
  "edge.466" "edge.372" "edge.370" "edge.360" "edge.358" "edge.264" \
  "edge.262" "edge.252" "edge.250" "edge.156" "edge.154" "edge.144" \
  "edge.142" "edge.48" "edge.47" "edge.46" "edge.45" "edge.36" "edge.35" \
  "edge.34" bellshape ratio1 0.5 intervals $n_mesh_y
undo endgroup
/ x1,x3,x4,x6
undo begingroup
edge delete "edge.26" "edge.134" "edge.242" "edge.1" "edge.4" "edge.9" \
  "edge.12" "edge.14" "edge.16" "edge.18" "edge.20" "edge.44" "edge.28" \
  "edge.30" "edge.32" "edge.38" "edge.40" "edge.42" "edge.217" "edge.220" \
  "edge.225" "edge.228" "edge.230" "edge.232" "edge.234" "edge.236" \
  "edge.260" "edge.244" "edge.246" "edge.248" "edge.254" "edge.256" \
  "edge.258" "edge.325" "edge.328" "edge.333" "edge.336" "edge.338" \
  "edge.340" "edge.342" "edge.344" "edge.350" "edge.352" "edge.354" \
  "edge.356" "edge.362" "edge.364" "edge.366" "edge.368" "edge.541" \
  "edge.544" "edge.549" "edge.552" "edge.554" "edge.556" "edge.558" \
  "edge.560" "edge.566" "edge.568" "edge.570" "edge.572" "edge.578" \
  "edge.580" "edge.582" "edge.584" keepsettings onlymesh
edge picklink "edge.582" "edge.578" "edge.572" "edge.568" "edge.558" \
  "edge.554" "edge.549" "edge.544" "edge.366" "edge.362" "edge.356" \
  "edge.352" "edge.342" "edge.338" "edge.333" "edge.328" "edge.258" \
  "edge.254" "edge.248" "edge.244" "edge.234" "edge.230" "edge.225" \
  "edge.220" "edge.42" "edge.38" "edge.32" "edge.28" "edge.18" "edge.14" \
  "edge.9" "edge.4" "edge.584" "edge.580" "edge.570" "edge.566" "edge.560" \
  "edge.556" "edge.552" "edge.541" "edge.368" "edge.364" "edge.354" \
  "edge.350" "edge.344" "edge.340" "edge.336" "edge.325" "edge.256" \
  "edge.246" "edge.260" "edge.236" "edge.232" "edge.228" "edge.217" "edge.40" \
  "edge.30" "edge.44" "edge.20" "edge.16" "edge.12" "edge.1" "edge.242" \
```

```
  "edge.134" "edge.26"
edge mesh "edge.26" "edge.134" "edge.242" "edge.1" "edge.4" "edge.9" \
  "edge.12" "edge.14" "edge.16" "edge.18" "edge.20" "edge.44" "edge.28" \
  "edge.30" "edge.32" "edge.38" "edge.40" "edge.42" "edge.217" "edge.220" \
  "edge.225" "edge.228" "edge.230" "edge.232" "edge.234" "edge.236" \
  "edge.260" "edge.244" "edge.246" "edge.248" "edge.254" "edge.256" \
  "edge.258" "edge.325" "edge.328" "edge.333" "edge.336" "edge.338" \
  "edge.340" "edge.342" "edge.344" "edge.350" "edge.352" "edge.354" \
  "edge.356" "edge.362" "edge.364" "edge.366" "edge.368" "edge.541" \
  "edge.544" "edge.549" "edge.552" "edge.554" "edge.556" "edge.558" \
  "edge.560" "edge.566" "edge.568" "edge.570" "edge.572" "edge.578" \
  "edge.580" "edge.582" "edge.584" bellshape ratio1 0.5 intervals $n_mesh_x1
undo endgroup
/
undo begingroup
edge delete "edge.109" "edge.112" "edge.117" "edge.120" "edge.122" "edge.124" \
  "edge.126" "edge.128" "edge.134" "edge.136" "edge.138" "edge.140" \
  "edge.146" "edge.148" "edge.150" "edge.152" "edge.433" "edge.436" \
  "edge.441" "edge.444" "edge.446" "edge.448" "edge.450" "edge.452" \
  "edge.458" "edge.460" "edge.462" "edge.464" "edge.470" "edge.472" \
  "edge.474" "edge.476" keepsettings onlymesh
edge picklink "edge.474" "edge.470" "edge.464" "edge.460" "edge.450" \
  "edge.446" "edge.441" "edge.436" "edge.150" "edge.146" "edge.140" \
  "edge.136" "edge.126" "edge.122" "edge.117" "edge.112" "edge.476" \
  "edge.472" "edge.462" "edge.458" "edge.452" "edge.448" "edge.444" \
  "edge.433" "edge.152" "edge.148" "edge.138" "edge.134" "edge.128" \
  "edge.124" "edge.120" "edge.109"
edge mesh "edge.109" "edge.112" "edge.117" "edge.120" "edge.122" "edge.124" \
  "edge.126" "edge.128" "edge.134" "edge.136" "edge.138" "edge.140" \
  "edge.146" "edge.148" "edge.150" "edge.152" "edge.433" "edge.436" \
  "edge.441" "edge.444" "edge.446" "edge.448" "edge.450" "edge.452" \
  "edge.458" "edge.460" "edge.462" "edge.464" "edge.470" "edge.472" \
  "edge.474" "edge.476" bellshape ratio1 0.5 intervals $n_mesh_x2
undo endgroup

/ volume mesh
undo begingroup
volume delete "base1" "volume.2" "volume.3" "volume.4" "up1" "volume.6" \
  "right1" "volume.8" "center1" "base2" "volume.11" "volume.12" "volume.13" \
  "up2" "volume.15" "right2" "volume.17" "center2" "base3" "volume.20" \
  "volume.21" "volume.22" "up3" "volume.24" "right3" "volume.26" "center3" \
  "base4" "volume.29" "volume.30" "volume.31" "up4" "volume.33" "right4" \
  "volume.35" "center4" "base5" "volume.38" "volume.39" "volume.40" "up5" \
  "volume.42" "right5" "volume.44" "center5" "base6" "volume.47" "volume.48" \
```

```
  "volume.49" "up6" "volume.51" "right6" "volume.53" "center6" onlymesh
volume mesh "base1" "volume.2" "volume.3" "volume.4" "up1" "volume.6" \
  "right1" "volume.8" "center1" "base2" "volume.11" "volume.12" "volume.13" \
  "up2" "volume.15" "right2" "volume.17" "center2" "base3" "volume.20" \
  "volume.21" "volume.22" "up3" "volume.24" "right3" "volume.26" "center3" \
  "base4" "volume.29" "volume.30" "volume.31" "up4" "volume.33" "right4" \
  "volume.35" "center4" "base5" "volume.38" "volume.39" "volume.40" "up5" \
  "volume.42" "right5" "volume.44" "center5" "base6" "volume.47" "volume.48" \
  "volume.49" "up6" "volume.51" "right6" "volume.53" "center6" map size 1
undo endgroup

/periodic
physics create "periodic" btype "PERIODIC" face "face.3" "face.10" "face.16" \
  "face.22" "face.27" "face.34" "face.39" "face.46" "face.51" "face.274" \
  "face.282" "face.288" "face.294" "face.298" "face.306" "face.310" \
  "face.318" "face.322"

/physics
if cond ($ph .gt. 1.5) // height == 2
physics create "fluid" ctype "FLUID" volume "base1" "volume.2" "volume.3" \
  "volume.4" "up1" "volume.6" "right1" "volume.8" "center1" "base2" \
  "volume.11" "up2" "base3" "volume.20" "volume.21" "volume.22" "up3" \
  "volume.24" "right3" "volume.26" "center3" "base4" "volume.29" "volume.30" \
  "volume.31" "up4" "volume.33" "right4" "volume.35" "center4" "volume.39" \
  "volume.40" "volume.42" "base6" "volume.47" "volume.48" "volume.49" "up6" \
  "volume.51" "right6" "volume.53" "center6"
physics create "porous1" ctype "FLUID" volume "volume.12" "volume.13" \
  "volume.15" "right2" "volume.17" "center2"
physics create "porous2" ctype "FLUID" volume "base5" "volume.38" "up5" \
  "right5" "volume.44" "center5"
endif
if cond ($ph .lt. 1.5) // height == 1
physics create "fluid" ctype "FLUID" volume "base1" "volume.2" "volume.3" \
  "volume.4" "up1" "volume.6" "right1" "volume.8" "center1" "base2" \
  "volume.11" "up2" "right2" "volume.17" "center2" "base3" "volume.20" \
  "volume.21" "volume.22" "up3" "volume.24" "right3" "volume.26" "center3" \
  "base4" "volume.29" "volume.30" "volume.31" "up4" "volume.33" "right4" \
  "volume.35" "center4" "volume.39" "volume.40" "volume.42" "right5" \
  "volume.44" "center5" "base6" "volume.47" "volume.48" "volume.49" "up6" \
  "volume.51" "right6" "volume.53" "center6"
physics create "porous1" ctype "FLUID" volume "volume.12" "volume.13" \
  "volume.15"
physics create "porous2" ctype "FLUID" volume "base5" "volume.38" "up5"
endif
```

VITA

Kang-Hoon Ko was born in Daejeon, South Korea. He received his B.S. degree in February 1995 and M.S. degree in February 1998 in mechanical engineering from Inha University, Inchon, South Korea. He joined Texas A&M University, College Station, Texas to pursue his Ph.D. degree. Kang-Hoon Ko married Hyekyung Yun in 2003, and has a son, John Youngkwang.

Permanent mailing address is :

403-54 Sambu APT

Teapyung-Dong,

Joong-Gu,

Daejeon, South Korea.

e-mail address :

indyko@hotmail.com